Effect of Severe Plastic Deformation on Microstructure in Metastable β-Ti Alloys

JIANG Baozhen

September 2015

Effect of Severe Plastic Deformation on Microstructure in Metastable β-Ti Alloys

JIANG Baozhen
Doctoral Program in Materials Science and Engineering

Submitted to the Graduate School of
Pure and Applied Sciences
in Partial Fulfillment of the Requirements
for the Degree of Doctor of Philosophy in
Engineering

at the
University of Tsukuba

Table of contents

Table of contents

Chapter 1 Introduction

1.1 Titanium and titanium alloys

Titanium and its alloys are relative newcomers to the field of structural materials compared with steel and aluminum alloys. The high strength-to-density ratio and the excellent corrosion resistance in titanium and its alloys make them more and more attractive for a variety of applications [1]. The comparison of strength-to-density ratio of different alloys is shown in Fig. 1.1. The applications of Ti and its alloys include aircraft (high strength in combination with low density), aero-engines (high strength, low density and good creep resistance to about 550 °C), biomedical devices (high corrosion resistance and high strength) and components in chemical processing equipment (corrosion resistance). The relatively high cost of titanium alloys initially limits their wider use, for example in automotive applications. To minimize the inherent cost problem, successful applications must take advantage of the special features and characteristics of titanium alloys that differentiate them from competing engineering materials. This requires a more complete understanding of titanium alloys, including the interplay between cost, processing methods and performance.

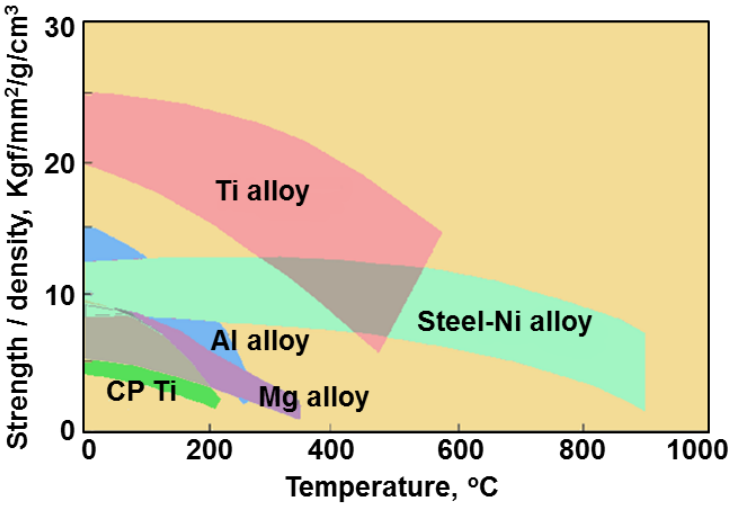

Fig. 1.1 Strength-to-density of different alloys [2].

1.1.1 Crystal structure in pure Ti

There are two types of crystal structures can be obtained in pure Ti. When the temperature is higher than 882 °C, it exhibits a body-centered cubic (BCC) crystal structure, namely β phase. When the temperature is lower than 882 °C, it exhibits a hexagonal close-packed (HCP) crystal structure, namely α phase [1]. In other

words, an allotropic phase transformation occurs at 882 ºC. The crystal structure of α phase and β phase is respectively shown in Fig. 1.2(a) and (b). The lattice parameters for pure α Ti at room temperature is a=0.295 nm and c=0.468 nm. The resulting c/a ratio is 1.587. The c/a ratio is influenced by the interstitial and substitutional elements and its value is usually smaller than the ideal c/a ratio of 1.633 for the HCP structure. There are three types of most densely packed lattice planes: the basal (0002) plane, the three prismatic $\{10\bar{1}0\}$ plane and the six pyramidal $\{10\bar{1}1\}$ plane. The close-packed direction is $<11\bar{2}0>$. The lattice parameter for pure β Ti at 900 ºC is a=0.332 nm. There are six most densely packed {110} planes, and the close packed directions are the four <111> directions.

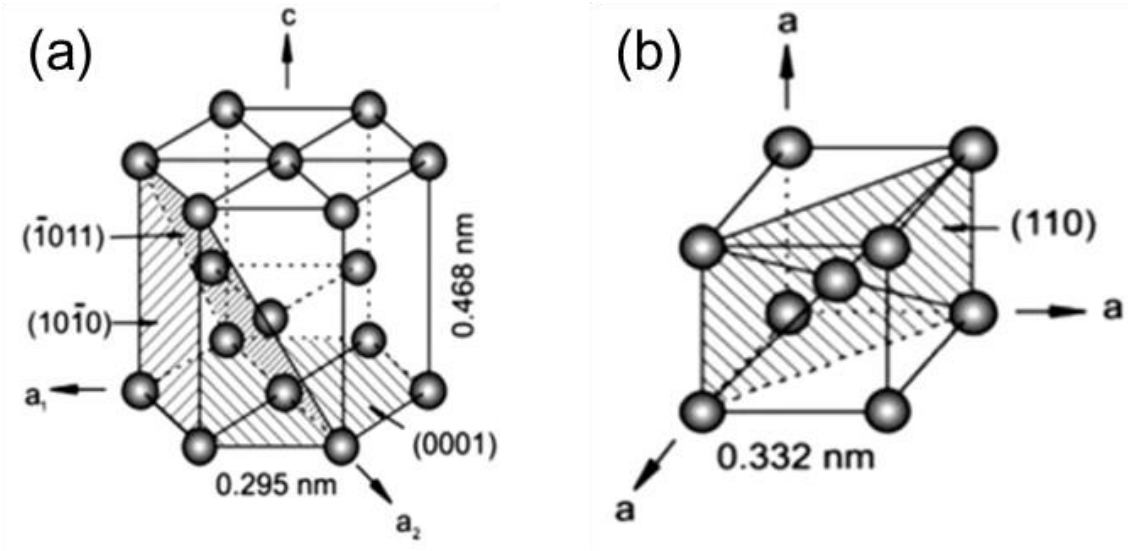

Fig. 1.2 Crystal structure of (a) HCP α phase and (b) BCC β phase [1].

1.1.2 Alloying elements

The alloying additions can alter both the α/β transformation temperature and different elements can result in different mechanical properties of Ti alloys [1]. Depending on whether the alloying elements increase or decrease the α/β transformation temperature, they are usually classified into α or β stabilizers.

The substitutional element Al and the interstitial elements O, N and C are all α stabilizers which can increase the α/β transus temperature with increasing the solute content, as shown by the schematic phase diagram in Fig. 1.3(a). Because Al is the only common metal which can raise the transition temperature and has large solubility in both the α and β phases, Al is the most widely used alloying element in Ti alloys. Generally, the Al content in multi-component Ti alloys is limited to about 6%, because the formation of a brittle Ti_3Al (α_2) phase at a higher content of Al can lead to a decrease in ductility. The different content of oxygen as an alloying element in Ti is used to obtain the desired strength level. This is especially true for the different pure Ti. Other α stabilizers, such as B, Ga, Ge and the rare earth elements, are not used commonly, because of their much lower solubility as compared to Al and O. In order to express the effect of α stabilizers in multicomponent Ti alloys, an equivalent Al content was made by the following equation [3]:

$$[Al]_{eq} = [Al] + 0.17[Zr] + 0.33[Sn] + 10[O] \qquad \text{(Eqn. 1.1)}$$

Other alloying elements, such as V, Mo, Nb, Hf, Ta, Mn, Cr, Cu, Ni, Fe, Co, Au, Ag, W, Pt and Pb, can decrease the α/β transus temperature with increasing the solute content and thus are known as β stabilizers. They are usually transition metals and noble metals in the periodic table which have unfilled or just-filled d-electron bands. These β stabilizers can be further divided into β isomorphous elements (in case of V, Mo, Nb, Hf and Ta) and β eutectoid forming elements (in case of Mn, Cr, Cu, Ni, Fe, Co, Au, Ag, W, Pt and Pb), depending on whether or not a solid solution / eutectoid compound exists at a sufficiently elevated temperature. Both types of phase diagrams are shown schematically in Fig. 1.3(b) and (c). Similarly to α stabilizers, the effect of β stabilizers were also expressed in terms of Mo equivalency depending on the amount of binary additions required to suppress the martensitic start temperature to go below room temperature. The equivalent equation is as follows [3]:

$$[Mo]_{eq} = [Mo] + 0.2[Ta] + 0.28[Nb] + 0.4[W] + 0.67[V] + 1.25[Cr] + 1.25[Ni] + 1.7[Mn] + 1.7[Co] + 2.5[Fe] \qquad \text{(Eqn. 1.2)}$$

In addition, there exist some elements, such as Zr, Hf and Sn, which have behave more or less neutrally (as shown in Fig. 1.3(d)), because they lower the α/β transformation temperature slightly but again increase it at higher concentrations. Zr and Hf are isomorphous with Ti and they exhibit allotropic phase transformation from β to α. Because of the chemical similarity of Zr to Ti, Zr is considered as α stabilizer. Sn on the other hand belongs to the β eutectoid forming elements but has no effect on the α/β transformation. But Sn is also considered as α stabilizer because Sn can replace Al in the hexagonal ordered Ti_3Al (α_2) phase.

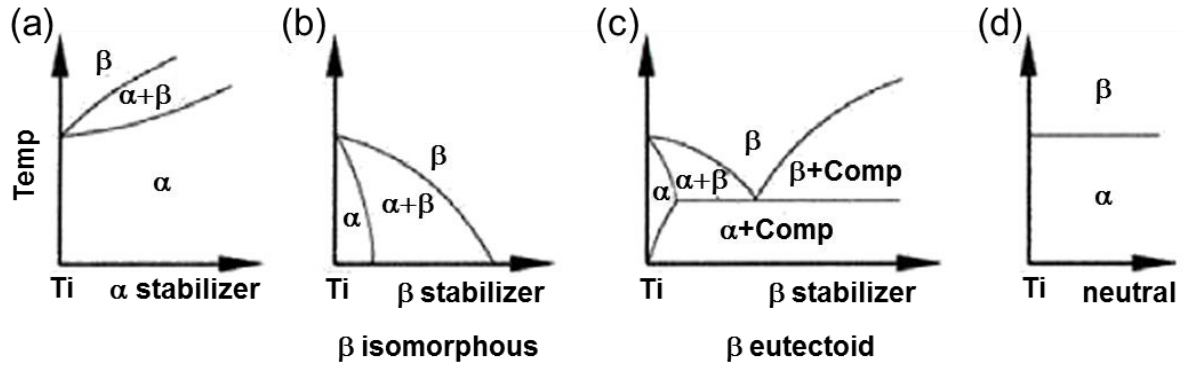

Fig. 1.3 Effect of alloying elements on phase diagrams of Ti alloys (schematically): (a) α stabilizers, (b) β isomorphous elements, (c) β eutectoid elements and (d) neutral elements [1].

1.1.3 Alloy classification

Commercial Ti alloys are classified conventionally into three different categories: α alloy, α+β alloy and β alloy, depending on the equilibrium phases at room temperature and metastable phases in as-quenched state, as shown in Fig. 1.4.

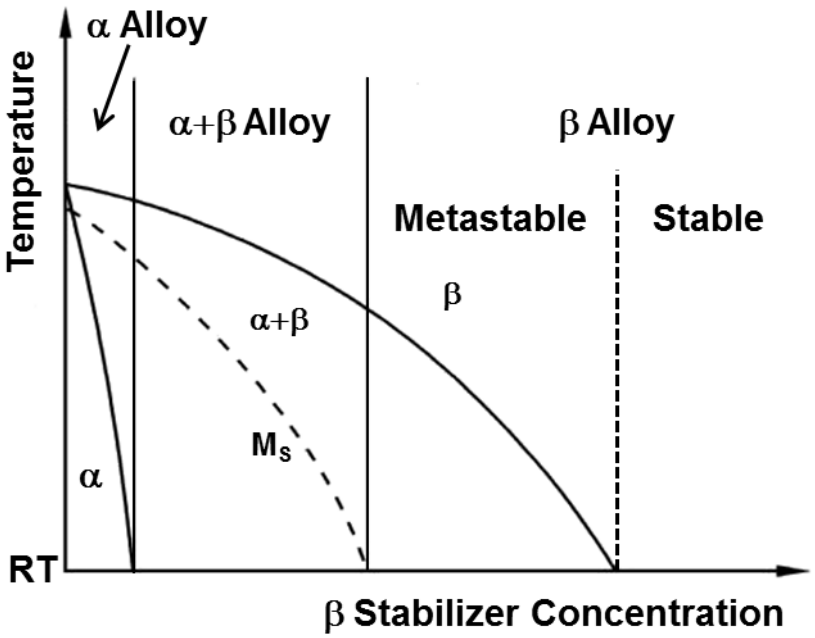

Fig. 1.4 Pseudo-binary section through a β isomorphous phase diagram (schematically), showing three types of Ti alloys [1].

1.1.3.1 Commercially pure (CP) α and α alloys

Alloys in this group include the various grades of CP Ti and alloys which contain only small amounts of α stabilizers, such as Fe and V. The microstructure mainly consists of α phase with a small amount of β phase presented to pin the grain boundaries [1]. The β phase is helpful in controlling the recrystallized α grain size and improves the hydrogen tolerance of these alloys. While all α alloys offer good corrosion resistance due to the stable oxide layer on the material, CP Ti does not meet the strength requirements for some applications due to the lack of solid solution strengtheners. α alloys usually exhibit good weldability due to a lack of response to heat treatment and are good for cryogenic applications as they do not have a ductile-to-brittle transition. In addition, some α alloys have good creep strength are preferred for elevated temperature applications up to about 400 ℃. The formability of α alloys is not good due to the hcp structure of α phase which require a high stress to activate the non-basal slip systems.

1.1.3.2 α+β alloys

The α+β alloys consist of a mixture of α and β phases. In this kind of Ti alloys, α stabilizers are used to stabilize and strengthen the α phase while β stabilizers with an amount of about 4-6% to allow considerable amounts of β phase to be retained at room temperature after quenching from the β or α+β phase fields. The alloys with a lower content of β stabilizers have high weldability while the alloys with a higher content of β stabilizers have high hardenability but low weldability. The α+β two phase field enables various heat treatments to be done, such as annealing, air cooling or quenching from the β or α+β phase fields. The α+β alloys can be further strengthened by solution treatment and aging, resulting in a variety of

microstructure/property combinations. The combination of the characteristics of α and β phases gives these alloys an attractive balance of properties, including a useful combination of strength, ductility, fatigue and fracture properties [1]. The α+β alloys can provide a weight savings in place of the lower strength aerospace type steels and have very superior corrosion resistance to Al alloys and low alloy steels. The α+β alloys are the most widely used Ti alloys for commercial applications. And the Ti-6Al-4V alloy is the workhorse of Ti industry because it accounts for about 60% of the total Ti production [4].

1.1.3.3 β alloys

The β alloys are those alloys which contain sufficient β stabilizers and can avoid martensitic transformation but retain a fully β structure when quenched from the β phase field. β alloys can be divided into stable β alloys which are non-hardenable and metastable β alloys which are hardenable and metastable β alloys are commonly used. Metastable β alloys exhibit high strength, which is controlled by the dispersion of α phase in the β matrix and good formability as a result of the simple body-centered cubic (bcc) structure in the as-quenched condition. The corrosion resistance is good and in some aspects better than α+β alloys due to the high hydrogen tolerance of the β phase. But metastable β alloys have poor high temperature creep and oxidation resistance except in the case of β-21S [5]. Currently these alloys are being used in aerospace applications and are emerging in the biomedical field due to their biocompatibility and useful range of bio-compatible mechanical properties. The usage in the aerospace will be talked later.

The properties for the three types of Ti alloys are summarized in Fig. 1.5. For CP α and α-Ti alloys, they usually have high young's modulus, high creep strength and high weldability. For b-Ti alloys, they usually have high heat-treatment sensitivity, high static strength, high fracture toughness and high formability at room temperature.

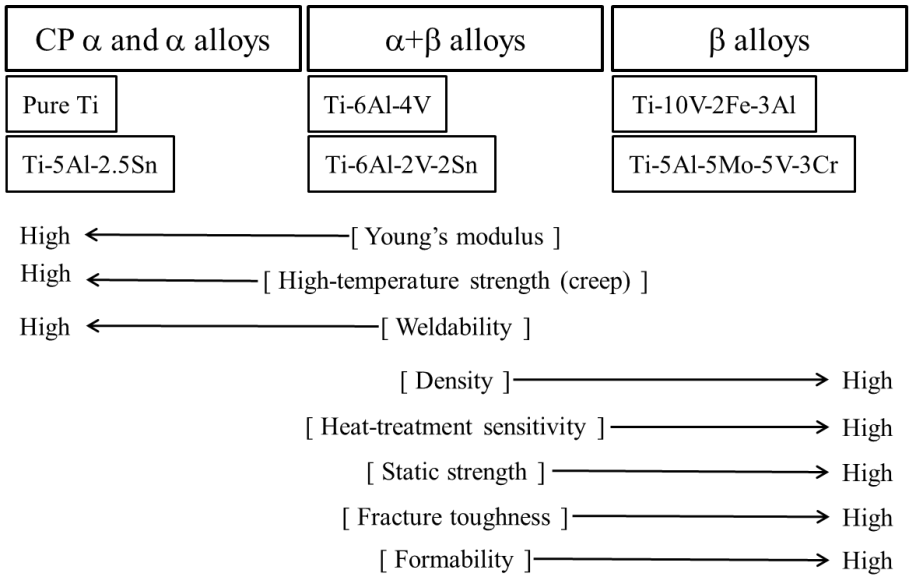

Fig. 1.5 Some properties for the three types of Ti alloys.

1.1.4 Phase transformation in metastable β-Ti alloys

Different phases can exist in β-Ti alloys depending on various factors, such as temperature, pressure, cooling rate and alloying additions. However, they can be broadly classified into equilibrium and non-equilibrium phases depending on whether enough time has been allowed to reach steady state conditions [1, 6, 7]. Equilibrium phases form only when sufficiently long time is given for phase transformation to reach the steady state conditions and will have the lowest possible Gibbs free energy. In β-Ti, there are two major equilibrium phases, namely α phase and β phase. Non-equilibrium phases essentially will represent either a local minima of the Gibbs free energy or can be a "frozen" unstable equilibrium state of the alloy due to kinetic constraints. Such non-equilibrium phases can be formed in thermal treatments faster than the treatment conditions required to form equilibrium phases. In β-Ti alloys, ω phase is one of the metastable phases. These higher free energy phases will transform to lower free energy equilibrium phases on availability of sufficient time and energy for the transformation.

1.1.4.1 β to ω phase transformation

The metastable ω phase can be classified into athermal ω phase and isothermal ω phase. The crystal structure of athermal ω phase and isothermal ω phase is essentially the same. The athermal ω phase is formed by quenching from the high-temperature β phase field. The formation of athermal ω phase is a diffusionless process, by the collapse of the {111} planes of the BCC phase via a displacive shuffle mechanism, retaining the composition of the parent β matrix [8-10]. The isothermal ω phase is usually formed by isothermal aging of β-Ti alloys below the ω-transus temperature. The formation mechanism of isothermal ω phase by the collapse of the {111} BCC planes is the same as that in athermal ω phase. But the formation of isothermal ω phase is a thermally-activated process involving diffusional composition partitioning [8, 11]. Fig. 1.6 shows the schematic diagram of the β to ω phase transformation by atomic collapse. The atom on layer 1 and layer 2 move to the position of layer 1.5 after the plane collapse. The ω phase exhibits two slightly different structures, namely as hexagonal symmetry (ideal ω) and trigonal symmetry (rumpled ω). The ω phase exhibits hexagonal symmetry when the collapse of {111} BCC planes is completely and the ω phase exhibits trigonal symmetry when the collapse of {111} BCC planes is partially [12, 13].

It is well known that the ω phase does not grow arbitrarily from the β matrix. The orientation relation between ω phase and β phase can be described as $[0001]_\omega$ // $(111)_\beta$ and $<11\bar{2}0>_\omega$ // $<011>_\beta$. From this orientation relationship, the lattice parameter of ideal ω phase can be defined as follows:

$$a_\omega = \sqrt{2}a_\beta \quad \text{and} \quad c_\omega = \left(\sqrt{3}/2\right)a_\beta \qquad \text{(Eqn 1.3)}$$

In addition, there are four crystallographic variants of the ω phase in the β matrix because of the four sets of <111> directions [8]. The presence of ω phase in the β matrix can be seen by the electron diffraction patterns along [113] and $[10\bar{1}]$ zone axis and all the four ω variants can be found along the [113] zone axis. In general,

the formation of these four ω variants is equal except in special cases, such as deformation or stress relaxation where preferential growth or reversion of certain ω variants may occur [14].

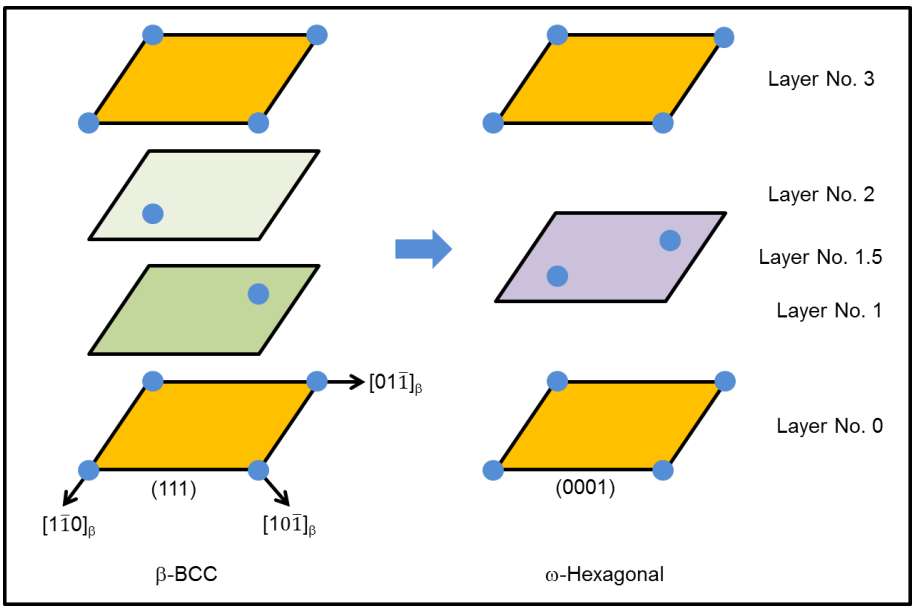

Fig. 1.6 Schematic diagram of the β to ω phase transformation by atomic collapse [8].

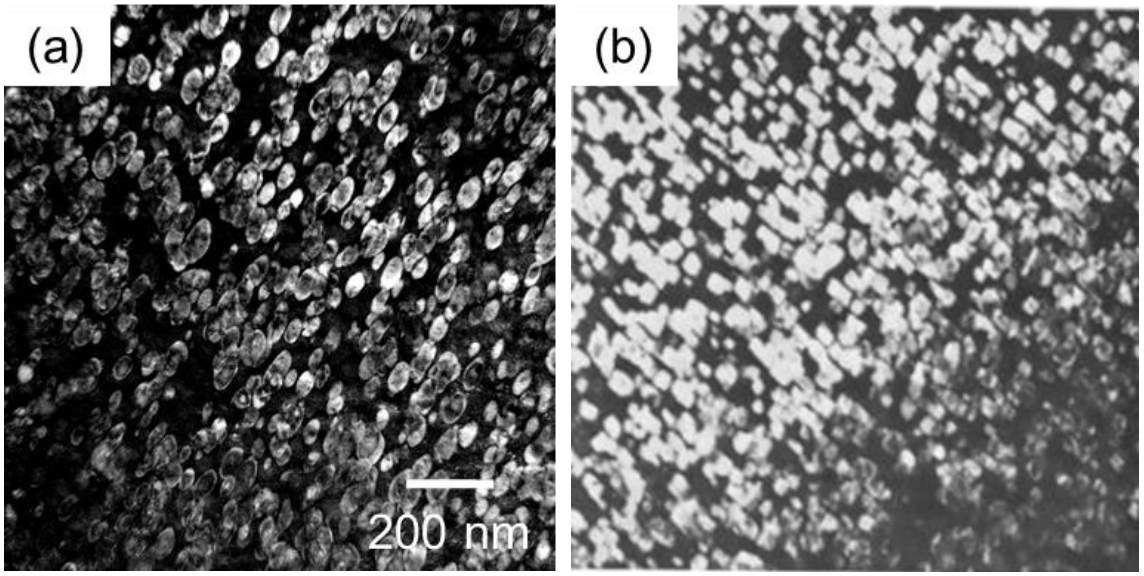

Fig. 1.7 (a) ellipsoidal morphology of isothermal w phase in Ti-15Mo (mass%) alloy, (b) cuboidal morphology of isothermal w phase in Ti-20V (mass%) alloy [21].

Both the athermal ω phase and isothermal ω phase are very fine. The size of athermal ω phase is ranging from several nanometers to around 20 nanometers in diameter. The isothermal ω phase is usually larger than the athermal ω phase depending on the aging temperature and aging time. In addition, the athermal ω phase can transform to isothermal ω phase by aging. The formation of isothermal ω phase upon aging is accompanied by a shift of the lattice parameter of β phase because of the enrichment of alloying elements in the β phase [15]. The isothermal ω phase has either an ellipsoidal or a cuboidal morphology

depending on the precipitate/matrix misfit [16-20]. The misfit is small in Ti-Mo and Ti-Nb alloys and the ellipsoidal morphology of ω phase is determined by minimizing the anisotropic surface energy. In contrast, in Ti-V, Ti-Mn, Ti-Fe and Ti-Cr alloys the misfit is large and cuboidal morphology of ω phase is formed by minimizing the matrix elastic strain. The isothermal ω phase with an ellipsoidal or a cuboidal morphology is respectively shown in Fig. 1.7(a) and (b). Blackburn *et al*. [16] also reported that the ω phase should be ellipsoidal in nature when the misfit was below 0.5% and be cuboidal when the misfit was higher than 0.5%.

1.1.4.2 β to α phase transformation

The β to α phase transformation is a diffusional process, requiring partitioning of alloying elements between α phase and β phase. The mechanical properties of metastable β-Ti alloys not only depend on the β phase matrix but, more importantly, depend on the α precipitates. The volume fraction, particle size, distribution and morphology of α precipitates are important microstructural parameters which can have pronounced effects on the mechanical properties [22-24]. Because of the strong influence on the mechanical properties of metastable Ti alloys, the nucleation and growth of α phase has been of great interest to numerous studies. However, controlling the precipitation of α phase as well as designing thermomechanical processes to obtain required high-level mechanical properties is still a widely known challenge.

During the formation of α phase, an orientation relationship is usually found between α phase and β matrix. The orientation relationships are preferred in order to minimize the interfacial energy. The most commonly observed orientation relationship between α phase β matrix is Burgers orientation relationship which can be described as $\{0001\}_\alpha$ // $\{011\}_\beta$; $<11\bar{2}0>_\alpha$ // $<1\bar{1}1>_\beta$ [25–27]. Each of the α phase with different orientation is called as a different variant and there are totally twelve α variants. One of the a variants with Burgers orientation relationship is shown in Fig. 1.8. In addition, some other orientation relationships have also been observed, including Pitsch-Schrader [28], Potter [29] and Rong-Dunlop [30].

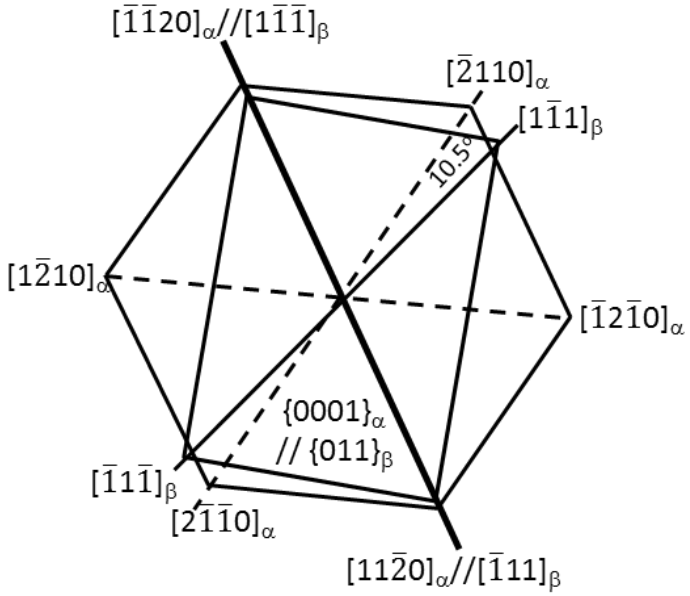

Fig. 1.8 Schematic presentation of Burgers orientation relationship between α phase and β matrix [26].

The α phase can be classified to three types depending on the nucleation sites, including the grain boundary α phase, intergranular α phase and intragranular α phase. The three types of α phase are indicated in Fig. 1.9, which shows the precipitation of α phase in Ti-5Al-5Mo-5V-3Cr (mass%) alloy after solution treatment at 850 ºC for 3.6 ks and aging at 600 ºC for 3.6 ks. Grain boundary α phase nucleates and grows along the β grain boundary. It is also named as allotrimorph α phase. One study on Ti-Cr alloys indicated that the grain boundary α phase was postulated to be formed by kink-on-edge mechanism [31]. Intergranular α phase nucleates at the β grain boundary or grain boundary α phase, growing into the interior of β grain and showing a lath shape. The intergranular α phase can have either the same or different orientations with the grain boundary α phase. The intergranular α phase with the same orientation as the grain boundary α phase is expected to be formed due to the instability of the α/β interface (between the grain boundary α and β matrix) formed by perturbation wavelength [32, 33]. The intergranular α phase with different orientation as the grain boundary α phase is expected to be formed by sympathetic nucleation mechanism. Sympathetic nucleation is defined as the nucleation of a precipitate crystal at an interphase boundary of a crystal of the same phase when these crystals differ in composition from their matrix phase throughout the transformation process [34]. For the intragranular α phase, the nucleation sites include the metastable phase such as ω phase [16, 35, 36] and defects such as vacancies and dislocations [37]. The intragranular α phase can also be divided into primary α phase and secondary α phase depending on the thermal mechanical processing sequence and the particle size [38]. Usually, the primary α phase forms earlier than the secondary α phase and has larger particle size. In β-Ti alloys, the α phase can be acicular shape or equiaxed shape. The acicular α phase as a transformation product upon aging is the most common. It is the result of the nucleation and growth of α phase maintain a specific crystallographic orientation with surrounding β matrix [27]. The equiaxed α phase is likely to be formed in severely deformed samples which have a high density of dislocations [37, 39-41].

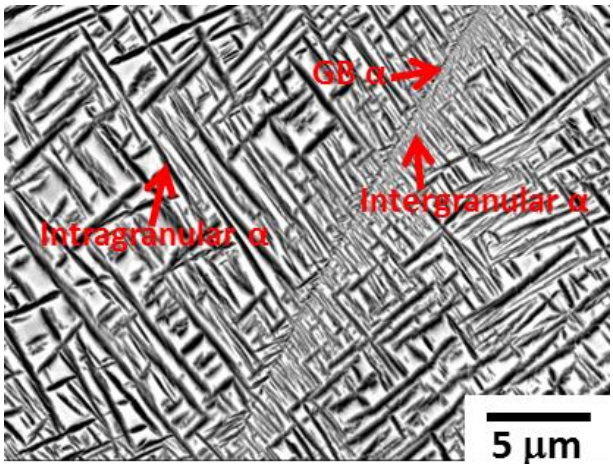

Fig. 1.9 Three types of α phase precipitated in Ti-5Al-5Mo-5V-3Cr (mass%) alloy after solution treatment at 850 ºC for 3.6 ks and aging at 600 ºC for 3.6 ks.

1.1.4.3 Nucleation of α from ω phase

At low isothermal aging temperatures, the athermal ω phase can undergo coarsening and act as uniformly distributed heterogeneous nucleation sites for α phase [16, 35, 36]. The ω-assisted heterogeneous nucleation results in a relatively large number of α precipitates which distribute in the β matrix uniformly. Furthermore, these α precipitates usually are of a fine particle size. The uniform distribution of fine α precipitates causes considerable strengthening of metastable β-Ti alloys.

Recently, different mechanisms have been proposed describing the role of ω phase in the nucleation of α phase. In case of the systems where the ω/β interfaces have a large misfit, a precipitates nucleate on the ledges and misfit dislocations at the ω/β interfaces [16, 42, 43]. As mentioned above, the ω phase in this system exhibits a cuboidal morphology and loses the coherency with the β matrix. However, there are considerable controversies about the ω-assisted nucleation of α phase in low ω/β misfit systems where the ω phase exhibits an ellipsoidal morphology.

1. Detailed studies on Ti-6.8Mo-4.5Fe-1.5Al (mass%) alloy indicated that the α phase nucleates near, but at a certain distance from the ω/β interfaces [44]. The local rejection of Al element, which is ω destabilizer but α stabilizer, from ω phase during the isothermal aging aids the precipitation of α phase in the vicinity of the ω phase. Such local enrichment of Al elements in the vicinity of isothermal ω phase has been confirmed by the atom probe analysis [45]. This is a possible mechanism for the nucleation of α phase in association with ω phase in low misfit ω/β systems.
2. α nucleates in the core of ω phase by a displacive transformation and consumes the latter during its growth [35]. This was suggested by high-resolution transmission electron microscopy (HPTEM) studies. However, it is should be noted that such a displacive mechanism should not be the only mechanism. Otherwise, the propensity of ω phase to act as potential nucleation sites for α phase should not be influenced by the ω/β misfit.

Recent study in Ti-5Al-5Mo-5V-3Cr (mass%) alloy by TEM and 3DAP indicates that a thermally activated diffusional process leads to the initial portioning of alloying elements during the isothermal coarsening of ω phase, resulting in the creation of favorable sites, marginally enriched in Al, for the nucleation of α phase. Subsequently, the α phase nucleates by a primarily displacive process, with a composition marginally enriched in Al as compared with the parent β matrix. Then the α phase grows via a coupled displacive-diffusional process with the diffusional portioning of the alloying elements being rate-controlling [36].

1.1.5 Metastable β-Ti alloys in aerospace industry

The first used β-Ti alloy on the aerospace industry was Ti-13V-11Cr-3Mo alloy on the Lockheed SR-71 Blackbird in the 1960s [46]. 93% of the aircraft was Ti and the majority of it was Ti-13V-11Cr-3Mo alloy. In the 1970s, metastable β-type Ti-13V-11Cr-3Al alloy was used as springs on commercial aircraft, but the

volume was small [5]. Metastable β-Ti alloys were used in significant amounts in 1980s. Over 250 parts per ship were fabricated from Ti-15V-3Cr-3Al-3Sn sheet. Compared with Ti-6Al-4V alloy, Ti-15V-3Cr-3Al-3Sn alloy had a lower cost and a better formability. In addition, it could be heated treated to obtain a high tensile strength of 1034 Mpa or higher. This alloy was used extensively in the nacelles and to form sine-wave spars for the empennage [5].

In the early 1990s, metastable β-Ti alloys were applied on Boeing 777 [5]. The most extensive usage was the high-strength Ti-10V-2Fe-3Al (Ti-1023) forgings in the structures of landing gear with a minimum ultimate tensile strength of 1193 MPa. This led weight savings and extended life due to the improved corrosion resistance of the β-Ti alloy compared with the high-strength low-alloy steel. There were over 200 Ti-1023 part numbers on the Boeing 777. Formed Ti-15V-3Cr-3Al-3Sn sheets were used in environmental control system ducting, clips and brackets, and floor support structure. It also was used for clock-type springs with a minimum ultimate tensile strength of 1034 MPa. Ti-3Al-8V-6Cr-4Mo-4Zr (β-C) alloy with a minimum ultimate tensile strength of 1240 MPa was used for coil-type springs. Ti-14.7Mo-2.7Nb-3Al-0.27Si (β-21S) alloy with excellent oxidation resistance, improved creep properties and good resistance to attack by thermally decomposed hydraulic fluid was used for high-temperature applications.

So it is evident that metastable β-Ti alloys are increasingly used in the aerospace industry in the past few decades. Also a lot of work is in progress to try to optimize the properties of these alloys or to design new metastable β-Ti alloys. For example, Ti-5Al-5Mo-5V-3Cr (Ti-5553) alloy is a recently developed metastable β-Ti alloy and will be in place of Ti-1023 alloy in some applications of Boeing 787. This alloy is the focus of the present work.

1.1.6 Mechanical properties in metastable β-Ti alloys

Typically, there are two deformation modes for the as-quenched β-Ti alloys which retain a fully β phase structure, including the {332} <113> twinning and the conventional dislocation slip [47]. The {332} <113> twinning occurred in metastable β titanium alloys is not observed in other metals and alloys with BCC structure, in which usually {112} <111> twinning happens. The presence of {332} <113> twining was first confirmed and regarded as stress-induced transformation in a Ti-15Mo-6Zr-4Sn (mass%) alloy by Blackburn and Feeney [48] depending on the TEM analysis. Then a series of studies was carried out by Hanada and Izumi [49] on the deformation modes of metastable β titanium alloys and demonstrated that the occurrence of {332} <113> twinning was closely related to the stability of β phase with respect to athermal ω phase. For the {332} <113> twinning system, there are 12 different variants [50]. However, the deformation by {332} <113> twining becomes more and more difficult as the alloying content increases and is practically suppressed by the precipitation of α phase [1]. In this case, the deformation by dislocation slip occurs. The slip systems in metastable β-Ti alloys with BCC structure include {110}, {112} and {123}, all with the same <111> direction which is a close-packed direction. And there are totally 48 slip systems. The influence of

different deformation modes on mechanical properties can be summarized as follows: deformation by {332} <113> twining leads to low yield strength, large uniform elongation, and high rate of work hardening; while deformation through dislocation slip leads to high yield strength, and small elongation in comparison [47].

The formation of isothermal ω phase by aging has a drastic change in the mechanical properties of metastable β-Ti alloys. There is an increase in the yield strength and a sharp decrease in the ductility. The ω-induced embrittlement has been studied by many previous works [51-53]. It is considered that the ω particles get sheared due to the passage of fairly large number of dislocations through them during deformation. The hardening by ω particles can be explained in terms of the high stress required for shearing these particles. The shearing of ω particles leads to the formation of slip bands in the metastable β-Ti alloys which contain a dense precipitation of ω particles. A set of dislocations glide along a particular slip plane and cut through a few ω particles, creating a softened channel. These channels slip can occur without much hindrance. Hence when slipping occurs, the plastic flow is confined within a limited number of slip bands. The crack nucleation occurs at the points where the slip bands meet either themselves or a grain boundary. Local deformation is pronounced in the narrow slip bands and high stress concentration favors crack propagation even at low macroscopic plastic strains.

Most metastable β-Ti alloys used in structural applications consist of two phase mixtures of α and β phase. A good combination of tensile strength and ductility can be obtained in metastable β-Ti alloys by controlling the precipitation of α phase. As mentioned above, the volume fraction, particle size, distribution and morphology of α phase are important microstructural parameters should be taken into account when modify the microstructures to improve the mechanical performance [22-24]. The precipitation of α phase in the β matrix is not coherent and thus can impede the motion of dislocations, leading to a strengthening of the material. Therefore, from the viewpoint of precipitation/dispersion hardening mechanism, a high volume fraction and a fine particle size of α phase are required to get a high strength [54]. The growth rate of α phase can be retarded by selecting an aging temperature as low as possible or by increasing the nucleation sites for α phase. In addition, a homogeneous distribution of α phase is necessary to avoid strain location during deformation in the areas not be hardened, which can result in a premature rupture. Homogeneous precipitation of α phase can be enhanced by controlling a high density of dislocations which are preferential nucleation sites for α phase or by using two-step aging treatment [55]. The morphology of α phase has almost no influence on the tensile strength but has a great influence on the ductility. It is reported that the equiaxed primary α phase could provide a higher ductility at a given strength level [22, 23, 56]. Continuous and thick grain boundary α phase must be avoided because it can act as preferential crack nucleation site and facilitate the propagation of cracks, which subsequently lead to a loss of the ductility [57-59]. The effective method to reduce the continuity and thickness of grain boundary α phase is grain refinement of β matrix [55, 60]. Also, due to the tendency for α phase to precipitate preferentially at grain boundaries when the β phase stability is too high, the stability should be properly adjusted to the required characteristics [55].

Among all these microstructural modifications, controlling a high density of dislocations is considered to be the most effective for obtaining homogeneous dispersed fine α phase which is desirable for attaining good combination of strength and ductility. An effective method to introduce a high density of dislocations is severe plastic deformation.

1.2 Severe plastic deformation

1.2.1 Definition of SPD

A formal definition of severe plastic deformation (SPD) states that SPD processing refers to any method of metal forming under an extensive hydrostatic pressure that may be used to impose a very high strain on a bulk solid and having the ability to produce exceptional grain refinement [61]. The way in which the initial sample shape is retained in SPD processing is by using special tool geometries which prevent the free flow of material and thereby produce a significant hydrostatic pressure; the plastic deformation under these conditions leads to a high density of lattice dislocations and consequent grain refinement. Different from the traditional cold working methods, SPD processing techniques should meet some requirements which are listed as follows [62]:

(1) Large plastic deformation (with true stains larger than 10) can be provided just by changing the fundamental parameters in the processing.
(2) Bulk ultrafine-grained (UFG) materials can be obtained. The generally-accepted definition of bulk UFG materials: bulk materials having fairly homogeneous deformed microstructure within the whole volume (with average grain sizes less than ~1 μm) and with a majority of boundaries having large angles of misorientations.
(3) The deformed samples should not have any mechanical damages and cracks, although samples are exposed to large plastic deformation.

1.2.2 Grain refinement mechanism by SPD

SPD can refine the grains by a combination of several different mechanisms, including the dislocation glide, accumulation, interaction, annihilation, tangling and spatial rearrangement [63-65]. In addition, deformation twinning can also play a significant role for the materials with medium or low stacking fault energies, especially in the nano-grain size range [65]. Detailed microstructural evolution may vary with the nature of the materials as well as the deformation mode, strain rate and temperature. Hansen and co-workers [63] have done extensive work on the grain refinement mechanism during rolling with strains less than 100%. Their general observations can also be applied to other deformation modes [64]. In FCC materials with coarse grains, each grain can be divided into many subgrains during plastic deformation [63]. Large subgrains may further be divided into smaller subgrains with increasing the strains, and the misorientation between subgrains may increase to form low angle and high angle (>15 °) grain boundaries. Although each subgrain deforms under less than five slip systems, a group of adjacent subgrains acts collectively to fulfill the Taylor criterion for maintaining uniform deformation. Usually, each subgrain can be subdivided into

dislocation cells. Lu *et al*. also systematically studied the formation of nanostructures under surface mechanical attrition treatment (SMAT) [65, 66]. It is found that the subgrains become elongated and their width becomes more and more smaller with increasing the plastic strain. When the width of the subgrains equals to the dislocation-cell size, lamellar subgrains containing a string of dislocation cells form. The misorientations across cell boundaries increase with further plastic strain, transforming dislocation cells into subgrains. The equiaxed subgrains further be divided into smaller dislocation cells, which, in turn, convert into smaller subgrains as well as nano-grains with increasing strain. Grain rotation may play a significant role in the formation of the nano-grains with high-angle boundaries. In addition, some authors relate them to in-situ recrystallization [67], their origin is most commonly placed in the formation or fragmentation of a dislocation cell structure whose size scale decreases as the stress rises during SPD processing [68-70].

1.2.3 SPD techniques

The most developed and significant SPD techniques are Equal-Channel Angular Pressing (ECAP), High-pressure Torsion (HPT), and Accumulative Rolling Bonding (ARB). Aside from the ones mentioned above, some other SPD techniques have been proposed in the last decades, including Multi-Directional Forging (MDF), Cyclic Extrusion and Compression (CEC), Twist Extrusion (TE), Repetitive Corrugation and Straightening (RCS), and others. In this section, ECAP and ARB will be introduced and discussed briefly. As the HPT processing is the SPD technique that utilized e in the present research, it will be discussed in a more detailed manner later.

1.2.3.1 Equal-Channel Angular Pressing (ECAP)

At present, ECAP is the most popular SPD processing technique and has been used for grain refinement in various metals and alloys. ECAP is a technique which processes a metallic billet through a simple shear [71]. The deformation principle of ECAP is shown schematically in Fig. 1.10. A billet is pressed through the special die in which the angle of intersection of two channels is Φ. The most used die angle is 90 °. A shear stress is introduced as the billet passes through the point of intersection between two channels, and it can be expressed as [72]:

$$\varepsilon = \left(\frac{N}{\sqrt{3}}\right)\left[2\cot\left\{\left(\frac{\phi}{2}\right)+\left(\frac{\psi}{2}\right)\right\}+\psi\csc\left\{\left(\frac{\phi}{2}\right)+\left(\frac{\psi}{2}\right)\right\}\right] \qquad \text{(Eqn 1.4)}$$

in which Ψ is the angle representing the outer arc of curvature where the two parts of the channels intersect (indicated in Fig. 1.10); *N* is the number of pass through the die. Each pass imposes an equivalent strain of around 1 for the 90° die. Since the cross-sectional dimensions of the billet remain unchanged after ECAP, the same billet can be processed repeatedly to impose exceptionally high strain, consequently achieving desired bilk nanostructured materials. Generally, by rotating the billet about its longitudinal axis between each pass, different slip systems may be introduced. And this leads to several processing routes: the orientation of a billet is not changed at each pass (route A); the orientation of a billet is rotated around its longitudinal axis

through the angle 90 ° after each pass (route B); the orientation of a billet is rotated around its longitudinal axis through the angle 180 ° after each pass (route C).

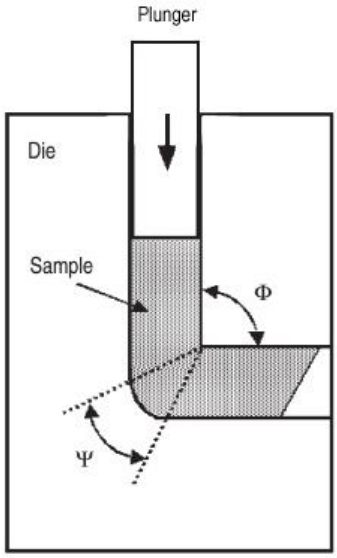

Fig. 1.10 The schematic principle of ECAP [61].

By ECAP processing, the ultrafine-grained microstructure can be obtained [62]. The grain refinement during ECAP is associated with some dislocation substructural characteristics, such as dislocation cells, subgrains and microbands, that are established during the first one or two passes [73, 74] and their transformation to ultrafine grains with further increasing the strain [75, 76].

1.2.3.2 Accumulative Rolling Bonding (ARB)

The technique of ARB uses conventional rolling deformation, realizing ultrahigh plastic strains in sheet materials for producing ultrafine-grained materials. Fig.1.11 illustrates the deformation principle of the ARB processing. A sheet is rolled by 50% reduction in thickness by a pre-rolling condition. Then the rolled sheet is cut into two pieces and stacked together to reform the initial dimensions. To achieve good bonding, the contact surfaces of the sheets are typically treated by degreasing and wire brushing. And then the stacking pieces are rolled again. The rolling in the ARB processing is a bonding process, which is known as roll bonding used for the production of clad sheets. Roll bonding is sometimes carried out at elevated temperatures, below the recrystallization temperature of the material in order to make the bonding better and to reduce the rolling force. By repeating the procedure, ultrahigh plastic strain can be applied on the sheet material without changing the dimensions. A natural limit of this approach lies in the increase in strength with increasing the ARB cycles and the gradually reduced surface quality of the roll-bonded sheets. During the ARB processing, the von Mises equivalent strain can be estimated by the following equation [61]:

$$\varepsilon_{eq} = 0.8n \qquad \text{(Eqn. 1.5)}$$

when 50% reduction in thickness per cycle is used. Here, n is the number of repeated ARB cycles. In this case, an equivalent strain of 4 can be achieved by five ARB cycles.

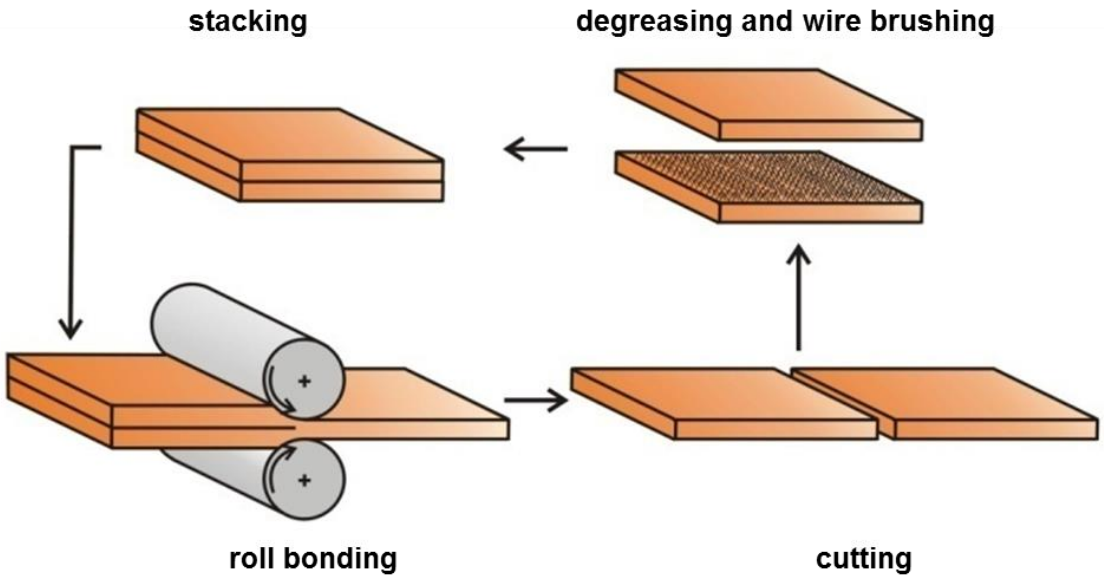

Fig. 1.11 Schematic illustration of the deformation principle of ARB processing [61].

1.3 High-pressure torsion (HPT)

HPT refers to a processing in which a thin disk sample is subjected to torsional straining under a high hydrostatic pressure [61]. The processing of metals by HPT has a long history dating back to the classic work by P.W. Bridgman at Harvard University in the 1930s [77]. Nevertheless, it is only within the last two decades that HPT processing has become a major research tool. This is mainly due to its ability to achieve a combination of exceptional grain refinement and a high density of dislocations [61, 78]. Typically, the grain sizes produced by HPT deformation are within the nanoscale range of about 50-100 nm.

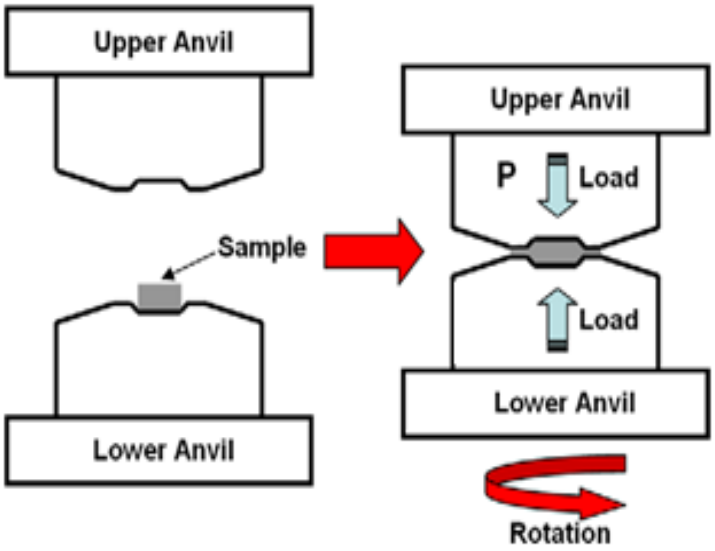

Fig. 1.12 Schematic illustration of the principle of HPT processing [79].

The schematic illustration of the principle of HPT processing is shown in Fig. 1.12. The disk sample is usually with a diameter of 10 or 20 mm and a thickness of 0.85 mm. This disk sample is placed between two

massive anvils, and it is held in place within a depression machined into the face of each anvil. During HPT processing, the disk sample is subjected to a high applied compressive pressure, P, which is usually up to several GPa. And the rotation of the lower anvil can introduce concurrent torsional straining. This type of HPT processing shown in Fig. 1.10 is designated quasi-constrained because there is some limited outward flow of the material around the periphery of the disk during the processing operation.

For HPT processing, the most potential limitation is that it uses the disk samples with relatively small dimensions. Recently, attempts are under way to expend the application of HPT processing to cylindrical samples with large height [80]. But the maximum practical volume of the processed parts is limited by the incurrence of large microstructural inhomogeneities within the vertical sections of these cylinders. The disk samples with larger diameters [81] or the ring-shaped samples [82] are also tried for HPT processing. The relatively small size of the sample limits the application of HPT processing in industry. But HPT processing is very useful for fundamental studies in laboratories, as it can provide the chance for obtaining ultrafine-grained materials, including the relatively brittle or high-strength materials which cannot be processed by other SPD methods.

1.3.1 Accumulated strain by HPT

The accumulated straining imposed on the disk sample by HPT processing can be estimated by using the parameters indicated in Fig. 1.13. For an infinitely small rotation, $d\theta$, and the displacement, dl is given by

$$dl = rd\theta \qquad \text{(Eqn. 1.6)}$$

where the r is the radius of the disk sample. The incremental shear strain, $d\gamma$, is given by

$$d\gamma = \frac{dl}{t} = \frac{rd\theta}{t} \qquad \text{(Eqn. 1.7)}$$

where t is the disk thickness.

By further assuming that the thickness of the disk sample is independent of the rotation angle, θ, it follows from formal integration that, since $\theta = 2\pi N$, the shear strain, γ, is given by

$$\gamma = \frac{2\pi N \cdot r}{t} \qquad \text{(Eqn. 1.8)}$$

where N is the number of rotation. Finally, the von Mises equivalent strain is then calculated using the relationship shown as follows [84-86]:

$$\varepsilon_{eq} = \frac{\gamma}{\sqrt{3}} = \frac{2\pi N \cdot r}{\sqrt{3}t} \qquad \text{(Eqn. 1.9)}$$

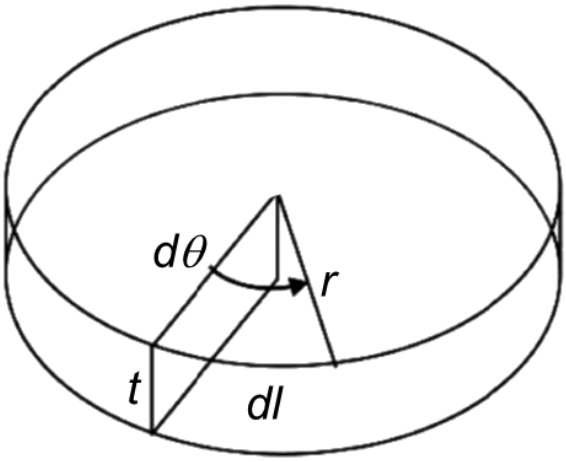

Fig. 1.13 Parameters used in estimating the total strain during HPT processing [83].

There are two remarks are true in respect to the equation 1.8. Firstly, the initial thickness of the sample is reduced under high compression pressure during HPT deformation, so the traditional use of the initial thickness of the sample, t, underrates the calculated strain values as compared to the true ones. Secondly, calculations by this equation have led to the conclusion that the shear strain should change linely from zero in the center of the disk sample to the maximum value on the edge. However, this is not confirmed by experiments. In addition, because HPT processing imposes a strain that is directly proportional to the radial distance from the rotation axis, there should be a significant strain inhomogeneity across the disk. In practice, however, HPT experiments demonstrated that the microstructure gradually evolves with increasing strain, so that, ultimately, the structure becomes reasonably homogeneous throughout the disk [80]. This development of homogeneity has been successfully modeled using strain gradient plasticity and incorporating a microstructure-related constitutive description of the material behavior.

1.3.2 Application of HPT on Ti and its alloys

HPT processing has been used successfully for investigating the phase transformation during the heavy deformation as well as the evolution of microstructure and mechanical properties concerning various pure metals and alloys. Some research on Ti and its alloys that processed by HPT are also reported. Todaka *et al*. reported that HPT processing could lead to the formation of submicron ω phase in pure Ti [87]. Valiev *et al*. reported that the application of HPT processing on CP Ti at room temperature resulted in the grain refinement with an average grain size of around 120 nm, the ultimate strength of 980 MPa and elongation to fracture of 12% [88]. Islamgaliev *et al*. observed that the ultimate strength of CP Ti was up to 1600 MPa while the ductility was around 5% as a result of isothermal HPT processing at 300 ^{o}C [89]. The α+β type Ti-6Al-4V alloy that processed by HPT exhibited ultrafine grains with the size of 100-200 nm, outstanding room temperature strength of 1.5 GPa and superplastic elongation of up to 500 % [90]. For β-type Ti alloys, a significant grain size effect on the reversible β to ω phase transformation in a Ti-36Nb-2.2Ta-3.7Zr-0.3O alloy during HPT processing was reported [91]. The decomposition of the ω phase to β phase was also

reported in Ti-15Mo alloy [92]. Farjami *et al*. reported that the significant grain refinement in Ti-30Nb-10Ta-5Zr alloy and Ti-15Mo alloy was achieved by HPT processing [93]. These HPT processed β-type Ti alloys showed an ultrafine grain size of about 50 nm and a marked increase in the hardness. In addition, Xu *et al*. reported the formation of ultrafine equiaxed α phase in HPT processed Ti-20Mo alloy upon isothermal aging [40]. However, there is limited analysis on the precipitation behavior of α phase in HPT processed β-type Ti alloy. More detailed studies needs to be carried out.

1.4 Materials (Ti-5553 alloy)

Ti-5Al-5Mo-5V-3Cr (Ti-5553) alloy was developed as an improved version of the Russian alloy VT22 (Ti-5.7Al-5.1V-4.8Mo-1Cr-1Fe). This alloy was initially produced for thick section forgings for high strength airframe components like landing gear and flap tracks [5, 94]. Ti-5553 alloy exhibits more favorable combinations of strength, ductility and toughness than the VT22.

Compared with Ti-1023 alloy, Ti-5553 alloy also exhibits some advantages. Firstly, Ti-5553 alloy has a wider processing window compared with Ti-1023 alloy. The processing is simple for Ti-5553 alloy and is all α/β worked. For Ti-1023 alloy, the primary forging is performed above the β transus, which is followed by about 15% α/β forging to achieve the right balance between strength, ductility and toughness. Secondly, Ti-5553 alloy has a much better hardenability than Ti-1023 alloy. Ti-5553 alloy can be heat treated in a section size up to 152 mm accompanied with only a slight drop in properties at the thicker section size by air cooling, whereas Ti-1023 alloy requires a water quenching and the section size is limited to 76 mm. This is mostly due to the more sluggish precipitation of α phase in Ti-5553 alloy because of the addition of Mo and Cr alloying elements. Finally, Ti-5553 alloy can be heat treated to a higher strength, with a minimum tensile strength of 1240 MPa as opposed to the 1192 MPa for Ti-1023 alloy.

Compared with the most commonly used α+β type Ti-6Al-4V (Ti-64) alloy, Ti-5553 alloy can exhibit higher strength, as summarized in Fig. 1.14. In addition, Ti-5553 alloy also exhibits outstanding high-cycle fatigue property compared with Ti-64 alloy, as shown in Fig. 1.15.

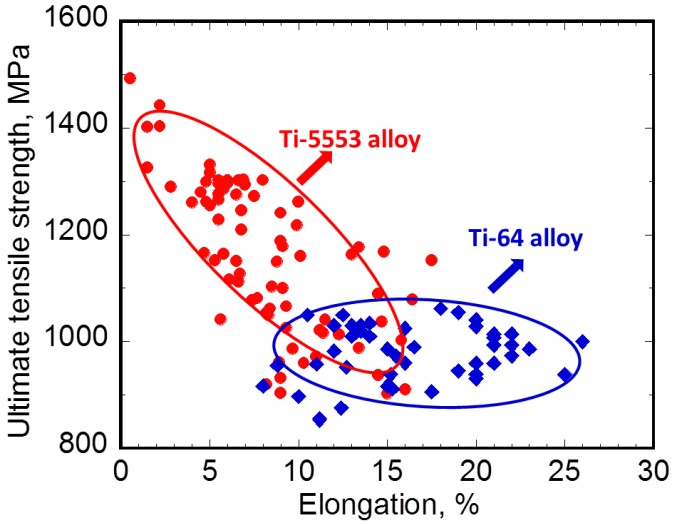

Fig. 1.14 Ultimate tensile strength and elongation of Ti-5553 alloy compared with Ti-64 alloy [24, 95-98].

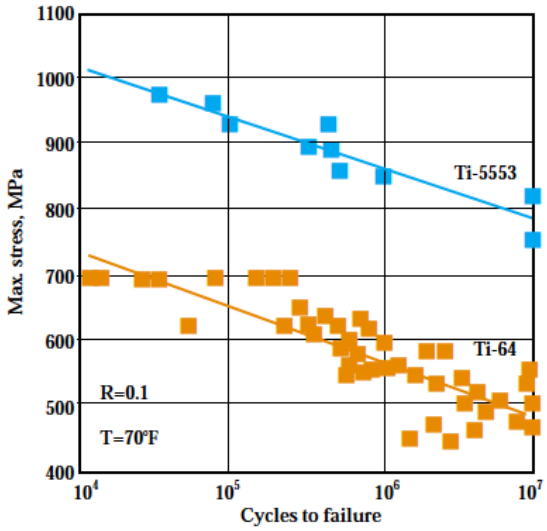

Fig. 1.15 High-cycle fatigue property of Ti-5553 alloy compared with Ti-64 alloy [99].

Ti-5553 alloy is capable of achieving strength up to 1517 MPa, although it is not typically used at this strength level. The application of Ti-5553 alloy in aerospace industry can be divided into two groups, including the high-strength version and low-strength version. The Ti-5553 alloy in high-strength version has a minimum tensile strength of 1240 MPa, a minimum elongation of 5%, and a minimum fracture toughness of 33 MPa $m^{1/2}$. This kind of Ti-5553 alloy is salted as bill-of-material for landing gear components on the Boeing 787. The Ti-5553 alloy in low-strength version has a minimum tensile strength of 1100 MPa and a minimum fracture toughness of 77 MPa $m^{1/2}$. This kind of Ti-5553 alloy is being studied for applications in the nacelles, fuselage and wing [5].

The mechanical properties of Ti-5553 alloy are very sensitive to the microstructure and can vary over a wide range depending on the microstructure. As shown in Fig. 1.14, a variety of ultimate tensile strength and elongation can be obtained for Ti-5553 alloy. Fig. 1.16 shows two typical microstructures in Ti-5553 alloy, which correspond to very different mechanical properties. Fig. 1.16(a) shows the microstructure in Ti-5553 alloy which is solution treated at 910 ºC for 0.42 ks, then fast cooled to 540 ºC and aged for 14.4 ks, and finally fast cooled to room temperature. In this kind of microstructure, the volume fraction of α phase is 40.1% and the thickness of α phase is 0.06 μm. And the corresponding ultimate tensile strength is 1302 MPa, along with an elongation of 6.6%. Fig. 1.16(b) shows the microstructure in Ti-5553 alloy which is solution treated at 910 ºC for 0.9 ks, then fast cooled to 675 ºC and aged for 57.6 ks, and finally fast cooled to room temperature. In this kind of microstructure, the volume fraction of α phase is 35.9% and the thickness of α phase is 0.38 μm. And the corresponding ultimate tensile strength is 972 MPa, along with an elongation of 11%.

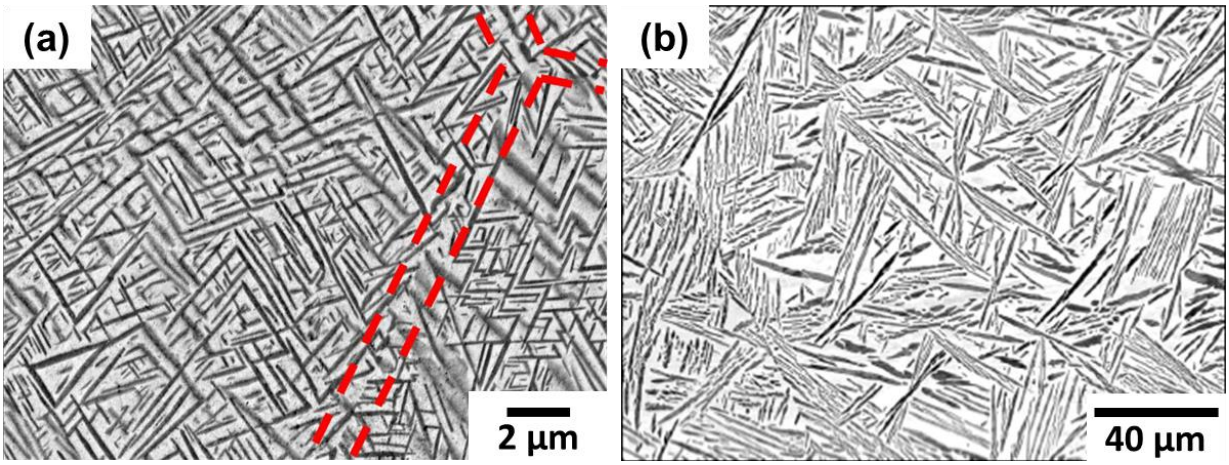

Fig. 1.16 The microstructure in Ti-5553 alloy: (a) solution treated at 910 °C for 0.42 ks, then fast cooled to 540 °C and aged for 14.4 ks, and finally fast cooled to room temperature (the red dotted lines show no grain boundary α), and (b) solution treated at 910 °C for 0.9 ks, then fast cooled to 675 °C and aged for 57.6 ks, and finally fast cooled to room temperature [96].

As a newly developed alloy, the current issue for Ti-5553 alloy is that the microstructure-mechanical properties relationship is limited studied. Therefore, to improve the mechanical properties, more detailed investigations are required to develop a deep fundamental understanding of the microstructural evolution and the corresponding mechanical properties.

1.5 Motivation

It has been known that HPT processing on Ti and its alloys van result in ultrafine-grained microstructure. According to the grain refinement mechanism, a high density of dislocations can also be produced. In the present research, HPT processing was applied on β-type Ti-5553 alloy:

(1) To investigate the evolution of microstructure and mechanical properties after HPT processing with different strains.

(2) To investigate the precipitation behavior of α phase in the HPT processed samples upon isothermal aging, and compared with that in the samples without HPT processing.

(3) To investigate the mechanical properties of the samples with different processing and heat treatments. Confirm the microstructure-mechanical properties relationship in Ti-5553 alloy.

1.6 References

[1] G. Lutjering, J.C. Williams, Titanium, second ed., Springer, Berlin, 2007 pp. 1-52.

[2] http://www.kobelco.co.jp/english/titan/files/details.pdf, KOBELCO.

[3] H.W. Rosenberg, The Science, Technology and Application of Titanium, Pergamon press, Oxford, UK (1970) pp.851.

[4] R.R. Boyer, An overview of the use of titanium in the aerospace industry, Mater. Sci. Eng. A 213 (1996) 103-114.

[5] R.R. Boyer, R.D. Briggs, The use of β titanium alloys in the aerospace industry, J. Mater. Eng. Perform. 14 (2005) 681-685.

[6] E. Collings, The physical metallurgy of titanium alloys, American Society for Metals, 1984 pp.261.

[7] E. Collings, Equilibrium phases in titanium alloys, American Society for Metals, 1994. 29.

[8] S.K. Sikka, Y.K. Vohra, R. Chidambaram, Omega phase in materials, Prog. Mater. Sci. 27 (1982) 245-310.

[9] D.D. Fontaine, N.E. Paton, J.C. Williams, The omega phase transformation in titanium alloys as an example of displacement controlled reactions, Acta Metall. 19 (1971) 1153-1162.

[10] J.C. Williams, D.D. Fontaine, N.E. Paton,The omega phase an an example of an unusual share transformation, Metall. Trans. A 4 (1973) 2701-2708.

[11] B.S. Hickman, Omega phase precipitation in alloys of titanium with transition metals, Trans. TMS-NIME 245 (1969) 1329-1336.

[12] R. Pynn, J. Phys. F: Met. Phys. 8 (1978) doi:10.1088/0305-4608/8/1/006.

[13] S. Banerjee, P. Mukhopadhyay, Phase transformations, examples from titanium and zirconium alloys, Oxford, Elsevier, 2007.

[14] T.S. Luhman, A.E. Curzon, An electron diffraction study of a Ti-22 at.% Nb alloy containing unequal populations of the four variants of the ω-phase, J. Mater. Sci. 7 (1972) 710-712.

[15] J.M. Silcock, An x-ray examination of the ω phase in TiV, TiMo and TiCr alloys, Acta Metall. 6 (1958) 481-493.

[16] M.J. Blackburn, J.C. Williams, Phase transformation in Ti-Mo and Ti-V alloys, Trans. TMS-AIME, 242 (1968) 2461-2469.

[17] W.G. Brammer, C.G. Rhodes, Determination of omega phase morphology in Ti-35% Nb by transmission electron microscopy, Phil. Mag. 16 (1967) 477-486.

[18] J.C. Williams, Titanium Technology: Present Status and Future Trends, TDA, Dayton, USA (1985) pp.75.

[19] J.C. Williams, M.J. Blackburn, The influence of misfit on the morphology and stability of the omega phase in titanium-transition metal alloys, Trans. TMS-AIME, 245 (1969) 2352-2355.

[20] M.J. Blackburn, Some aspects of phase transformation in titanium alloys, The Science, Technology and Application of Titanium, (1970) 633-643.

[21] B.S. Hickman, The formation of omega phase in titanium and zirconium alloys: a review J. Meter. Sci. 4 (1969) 554-563.

[22] G.T. Terlinde, T.W. Duerig, J.C. Williams, Microstructure, tensile deformation and fracture in aged Ti-10V-2Fe-3Al, Metall. Trans. A 14A (1983) 2101-2105.

[23] G. Terlinde, H.J. Rathjen, K.H. Schwalbe, Microstructure and fracture toughness of the aged β-Ti alloy

Ti-10V-2Fe-3Al, Metall. Trans. A 19A (1988) 1037-1049.

[24] N. Clement, A. Lenain, P.J. Jacques, Mechanical property optimization via microstructural control of new metastable beta titanium alloys, JOM 59 (2007) 50-53.

[25] W.G. Burgers, Physics, 1 (1934) 561-586.

[26] D. Bhattacharyya, G. Viswanathan, R. Denkenberger, D. Furrer, H.L. Fraser, The role of crystallographic and geometrical relationships between alpha nad beta phases in an alpha/beta titanium alloys, Acta Mater. 51 (2003) 4679-4691.

[27] T. Furuhara, T. Makino, Y. Idei, H. Ishigaki, A. Takada, T. Maki, Morphology and crystallography of α precipitates in β Ti-Mo binary alloys, Mater. Trans. 39 (1998) 31-39.

[28] W. Pitsch, A. Schrader, Arch. Eisenhutt Wes. 29 (1958) 715-719.

[29] D.I. Potter, Jour. Less-common Metals 31 (1973) 299-309.

[30] W. Rong, G.L. Dunlop, The crystallography of secondary carbide precipitation in high-speed steel, Acta Metall. 32 (1984) 1591-1599.

[31] T. Furuhara, H.I. Aaronson, Crystallography and interfacial structure of proeutectoid alpha grain boundary allotriomorphs in a hypoeutectoid Ti-Cr alloy, Acta Metall. Mater. 39 (1991) 2887-2899.

[32] W.W. Mullins, R.F. Sekerka, Morphological stability of a particle growing by diffusion or heat flow, Jour. Appl. Phys. 34 (1963) 323-329.

[33] W.W. Mullins, R.F. Sekerka, Stability of a planar interface during soludification of a dilute binary alloy, Jour. Appl. Phys. 35 (1964) 444-451.

[34] H.I. Aaronson, G. Spanos, R.A. Masamura, R.G. Vardiman, D.W. Moon, E.S.K. Menon, M.G. Hall, Sympathetic nucleation: an overview, Mater. Sci. Eng. B 32 (1995) 107-123.

[35] F. prima, P. Vermaut, G. texier, D. Ansel, T. Gloriant, Evidence of α-nanophase heterogeneous nucleation from ω particles in a metastable Ti-based alloy by high-resolution electron microscopy, Scripta Mater. 54 (2006) 645-648.

[36] S. Nag, R. Banerjee, R. Srinivasan, J.Y. Hwang, M. Harper, H.L. Fraser, ω-assisted nucleation and growth of α precipitates in the Ti-5Al-5Mo-5V-3Cr-0.5Fe β titanium alloy, Acta Mater. 57 (2009) 2136-2147.

[37] T. Makino, R. Chikaizumi, T. Nagaoka, T. Furuhara, T. Makino, Microstructure development in a thermomechanically processed Ti-15V-3Cr-3Al alloy, Mater. Sci. Eng. 213 (1996) 51-60.

[38] R.R. Boyer, G. Welsch, E.W. Collings, Materials properties Handbook: titanium alloys, ASM, 1994 pp1051.

[39] T. Inaba, K. Ameyama, M. Tokizane, Formation of (a+b) microduplex structure in a Ti-15V-3Ct-3Sn-3Al alloy, ISIJ International, 31 (1991) 792-798.

[40] W. Xu, D.P. Edwards, X. Wu, M. Stoica, M. Calin, U. Kuhn, J. Eckert, K. Xia, Promoting nano/ultrafine-duplex structure via accelerated α precipitation in a β-type titanium alloy severely deformed by high-pressure torsion, Scripta Mater. 68 (2013) 67-70.

[41] W. Xu, X. Wu, M. Stoica, M. Calin, U. Kuhn, J. Eckert, K. Xia, on the formation of an ultrafine-duplex structure facilitated by severe plastic deformation in a Ti-20Mo β-type titanium alloy, Acta Mater. 60 (2012) 5067-5078.

[42] Y. Ohmori, T. Ogo, K. Nakai, K. Kobayashi, Effects of ω-phase on β to α, α″ transformations in a metastable

β titanium alloy, Mater. Sci. Eng. A 312 (2001) 182-188.

[43] Y. Ohmori, H. Natsui, K. Nakai, H. Ohtsubo, Efffects of ω phase formation on decomposition of α'/β duplex phase structure in a metastable β-Ti alloy, Mater. Trans. JIM 39 (1998) 40-48.

[44] S. Azimzadeh, H.J. Rack, Phase transformations in Ti-6.8Mo-4.5Fe-1.5Al, Matall. Mater. Trans. A 29 (1998) 2455-2467.

[45] A. Vassel, In: D. Eylon, R.R. Boyer, D.A. Koss, editors. Beta titanium alloys in the 1990s, Warrendale, PA: TMS, (1993) pp. 173.

[46] R.R. Boyer, Applications of beta titanium alloys in airframs, Beta Titanium Alloys in the 1990's, D. Eylon, R.R. Boyer, and D.A. Koss, Ed., the Materials Society, 1993, pp. 335-346.

[47] S. Hanada, O. Izumi, Correlation of tensile properties, deformation modes, and phase stability in commercial β-phase titanium alloys, Metall. Trans. A, 18 (1987), 265-271.

[48] M. J. Blackburn, J. A. Feeney, Stress-induced transformations in Ti-Mo alloys, J. Inst. Metals. 99 (1971) 132-134.

[49] S. Hanada, O. Izumi, transmission electron microscopic observations of mechanical twinning in metastable beta titanium alloys, Metall. Trans. A 17 (1986) 1409-1420.

[50] E. Bertrand, P. Castany, I. Péron, T. Gloriant, Twining system in a metastable β-titanium alloy by Schmid factor analysis, Script Mater. 64 (2001), 1110-1113.

[51] J.C. Williams, B.S. Hickman, H.L. Marcus, The effect of omega phase on the mechanical properties of titanium alloys, Met. Trans. 2 (1971) 1913-1919.

[52] A.W. Bowen, Omega phase embrittlement in aged Ti-15Mo, Scripta mater. 5 (1971) 709-716.

[53] A.W. Bowen, On the strengthening of a metastable β-titanium alloy by ω- and α- precipitation, Titanium '80: Sceience and technology, (1980) 1317-1326.

[54] F.H. Froes, J.C. Chesnutt, C.G. Rhodes, J.C. Williams, Toughness and fracture behavior of titanium, ASTM STP651, ASTM, OH, 1978, pp. 115.

[55] Y. Kawabe, S. Muneki, Strengthening and toughening of titanium alloys, ISIJ International, 31 (1991) 785-791.

[56] R. Boyer, G. Welsch, E.W. Collings, Materials Properties Handbook: Titanium Alloy. Materials Park, OH: ASM International (1994) 829-865.

[57] A. Ghosh, S. Sivaprasad, A. Bhattacharjee, S.K. Kar, Microstructure-fracture toughness correlation in an aircraft structural component alloy Ti-5Al-5Mo-5V-3Cr, Mater. Sci. Eng. A 568 (2013) 61-67.

[58] G. Lutjering, J.Albrecht, C. Sauer, T. Krull, the influence of soft, precipitate-free zones at grain boundaries in Ti and Al alloys on their fatigue and fracture behavior, Mater. Sci. Eng. A 468 (2007) 201-209.

[59] J.W. Foltz, B. Welk, P.C. Collins, H.L. Fraser, J.C. Williams, Formation of grain boundary α in β Ti alloys: its role in deformation and fracture behavior of three alloys, Metall. Mater. Trans. A 42A (2011) 645-650.

[60] O.M. Ivasishin, R.V. Teliovich, Potential of rapid heat treatment of titanium alloys and steels, Mater. Sci. Eng. A 263 (1999) 142-154.

[61] R.Z. Valiev, Y. Estrin, Z. Horita, T. G. Langdon, M. J. Zehetbauer, Y.T. Zhu, Producing bulk ultrafine-grained materials by severe plastic deformation, JOM 58-4 (2006) 33-39.

[62] R.Z. Valiev, R.K. Islamgaliev, Bulk nanostructured materials from severe plastic deformation, Prog. Mater.

Sci. 45 (2000) 103-189.

[63] B. Bay, N. Hansen, D.A. Hughes, D. Kuhlmannwilsdorf, Overview no. 96: Evolution of FCC deformation structures in polyslip, Acta Metal. Mater. 40 (1992) 205-219.

[64] J.Y. Huang, Y.T. Zhu, H. Jiang, T.C. Lowe, Microstructures and dislocation configurations in nanostructured Cu processed by repetitive corrugation and straightening, Acta Mater. 49 (2001) 1497-1505.

[65] K. Lu, N. Hansen, Structural refinement and deformation mechanisms in nanostructured metals, Scripta Mater. 60 (2009) 1033-1038.

[66] K. Lu, J. Lu, Surface nanocrystallization (SNC) of metallic materials-presentationof the concept behind a new approach, J. Mater. Sci. Technol. 15 (1999) 193-197.

[67] R. Lapovok, P. F. Thomson and R. Cottam, The effect of grain refinement by warm equal channel extrusion on room temperature twining in magnesium alloy ZK 60, J. Mater. Sci. 40 (2005), 1699-1708.

[68] Y. Estrin, L.S. Tóth, Y. Brechet and H.S. Kim, Modelling of the evolution of dislocation cell misorientation under severe plastic deformation, Mater. Sci. Forum 503-504 (2006) 675-680.

[69] T. Ungár and M. Zehetbauer, Stage IV work hardening in cell forming materials, part II: a new mechanism, Scripta Mater. 35 (1996), 1467-1473.

[70] M. Zehetbauer, T. Ungár, R. Kral, A. Borbély, E. Schafler, B. Ortner, H. Amenitsch, S. Bernstorff, Scanning X-ray diffraction peak profile analysis in deformed Cu-polycrystals by synchrotron radiation, Acta Mater. 47 (1999), 1053-1061.

[71] V.M. Segal, V.I. Reznikov, A.E. Drobyshevkij, V.I. Kopylov, Plastic working of metals by simple shear, Russ. Metall. 99 (1981) 99-105.

[72] Y. Iwahashi, J. Wang, Z. Horita, M. Nemoto, T.G. Langdon, Principle of equal-channel angular pressing for the processing of ultra-fine grained materials, Scripta Mater. 35 (1996) 143-146.

[73] S.C. Baik, R.J. Hellmig, Y. Estrin, H.S. Kim, Modeling of deformation behavior of copper under equal channel angular pressing, Z. Metallkd. 94 (2003) 754-760.

[74] Q. Xue, I.J. Beyerlein, D.J. Alexander, G.T. Gray, Mechanisms of initial grain refinement of OFHC copper in equal channel angular extrusion, Acta Mater. 55 (2007) 655-668.

[75] A. Vinogradov, T. Suzuki, S. Hashimoto, K. Kitagawa, A. Kuznetsov, S. Dobatkin, Structure and mechanical properties of submicrocrystalline copper produced by ECAP to very high strains, Mater. Sci. Forum, 503–504 (2006) 971-976.

[76] Y. Iwahashi, Z. Horita, M. Nemoto, T.G. Langdon, An investigation of microstructural evolution during equal-channel angular pressing, Acta Mater. 45 (1997) 4733-4741.

[77] P.W. Bridgman, Effects of high shearing stress combined with high hydrostatic pressure, Phys. Rev. 48 (1935) 825-847.

[78] A.P. Zhilyaev, T.G. Langdon, Using high-pressure torsion for metal processing: fundamentals and applications, 53 (2008) Prog. Mater. Sci. 893-979.

[79] K. Edalati, Z. Horita T.G. Langdon, The significance of slippage in processing by high-pressure torsion, Scripta Mater. 60 (2009) 9-12.

[80] G. Sakai, K. Nakamura, Z. Horita, T.G. Langdon, Developing high-pressure torsion for use with bulk samples, Mater. Sci, Eng. A 406 (2005) 268-273.

[81] Y. Todaka, M. Umemoto, A. Yamazaki, J. Sasaki, K. Tsuchiya, Effect of strain path in high-pressure torsion process on hardening in commercial purity titanium, Mater. Trans. 49 (2008), 47-53.

[82] Y. Harai, Y. Ito and Z. Horita, High-pressure torsion using ring specimens, Scripta Mater. 58 (2008), 469-472.

[83] A.P. Zhilyaev, G.V. Nurislamova, B.K. Kim, M.D. Baro, J.A. Szpunar, T.G. Langdon, Experimental parameters influencing grain refinement and microstructural evolution during high-pressure torsion, Acta Mater. 51 (2003) 753-765.

[84] F. Wetscher, R. Pippan, S. Sturm, F. Kauffmann, C. Scheu, G. Dehm, TEM investigations of the structural evolution in a pearlitic steel deformed by high-pressure torsion, Metall. Mater. Trans. A 37 (2006) 1963-1968.

[85] F. Wetscher, A. Vorhauer, R. Stock, R. Pippan, Structural refinement of low alloyed steels during severe plastic deformation, Mater. Sci. Eng. A 387-389 (2004) 809-816.

[86] R.Z. Valiev, Y.V. Ivanisenko, E.F. Rauch, B. Baudelet, Structure and deformaton behaviour of Armco iron subjected to severe plastic deformation, Acta Mater. 44 (1996) 4705-4712.

[87] Y. Todaka, J. Sasaki, T. Moto, M. Umemoto, Bulk submicrocrystalline w-Ti produced by high-pressure torsion straining, Scripta Mater. 59 (2008) 615-618.

[88] R.Z. Valiev, A.V. Sergueeva, A.K. Mukherjee, The effect of annealing on tensile deformation behavior of nanostructured SPD titanium, Scripta Mater. 49 (2003) 669-674.

[89] R.K. Islamgaliev, V.U. Kazyhanov, L.O. Shestakova, A.V. Sharafutdinov, R.Z. Valiev, Microstructure and mechanical properties of titanium (Grade 4) processed by high-pressure torsion, Mater. Sci. Eng. A 493 (2008) 190-194.

[90] A.V. Sergueeva, V.V. Stolyarov, R.Z. Valiev, A.K. Mukherjee, Superplastic behavior of ultrafine-grained Ti-6Al-4V alloys, Mater. Sci. Eng. A 323 (2002) 318-325.

[91] Y.B. Wang, Y.H. Zhao, Q. Liao, R.Z. Valiev, S.P. Ringer, Y.T. Zhu, E.J. Lavernia, Grain size and reversible beta-to-omega phase transformation in a Ti alloy, Scripta Mater. 63 (2010) 613-616.

[92] K. Tsuchiya, S. Farjami, B.Z. Jiang, X.H. Min, S. Emura, S. Ii, Effect of high-pressure torsion deformation on isothermal ω phase in β-Ti alloys, Proceedings of 12th world Conference on Titanium, Volume I, (2011) 584-587.

[93] S. Frajami, K. Tsuchiya, Y. Todaka, M. Umemoto, Nanocrystallization of β-titanium alloys by high-pressure torsion, Processing and Fabrication of Advanced Materials – XVIII, (2009) 1053-1060.

[94] S.L. Nyakana, J.C. Fanning, R.R. Boyer, Quick reference guide for β titanium alloys in the 00s, J. Mater. Eng. Perform. 14 (2005) 799-811.

[95] J.C. Fanning, Properties of TIMETAL 555, J. Mater. Eng. Perform. 14 (2005) 788-791.

[96] B.A. Welk, Microstructural and property relationships in β-titanium alloy Ti-5553, Master's thesis, The Ohio State University, 201 West 19th Avenue, Columbus, OH 43210, 2010.

[97] R.P. Giosa, Microstructure evolution and mechanical properties in Ti-5Al-5Mo-5V-3Cr after solution treatment and aging in the alpha-beta range, Mc Master University.

[98] R. Boyer, G. Welsch, E.W. Collings, Materials Properties Handbook: Titanium Alloy. Materials Park, OH: ASM International (1994) 525-527.

[99] S. Veeck, D. Lee, R.R. Boyer, R. Briggs, The castability of Ti-5553 alloy: Its microstructure and properties, Adv. Mater. Processes 162 (2004) 47-49.

Chapter 2 Microstructure and mechanical properties of Ti-5553 alloy processed by high-pressure torsion

2.1 Introduction

Metastable β-Ti alloys have great potentials as structural materials due to their good formability at room temperature, high strength-to-density ratio, excellent age hardenability and good corrosion resistance [1-3]. In the past two decades, the metastable β-Ti alloys are increasingly used in aerospace industry. For example, Ti-5Al-5Mo-5V-3Cr (mass%, Ti5553) alloy, which is a newly developed metastable β-Ti alloy, is being used for landing gear components on Boeing 787 [4]. The required high-level mechanical properties of metastable β-Ti alloys depend on several strengthening mechanisms, including the solid solution strengthening, precipitation strengthening (such as precipitation of ω phase and α phase), grain refinement strengthening and dislocation strengthening [5].

In recent years, severe plastic deformation (SPD) by high-pressure torsion (HPT) processing has attracted much attention. The advantage of HPT processing is that a combination of exceptional grain refinement (< 100 nm) and high density of dislocations can be produced by the large shear strain [6]. Previous studies on the microstructure and mechanical properties of commercially pure titanium (CP Ti) and α+β Ti alloys processed by HPT were reported. Valiev *et al.* reported that the application of HPT processing at room temperature resulted in the grain refinement of CP Ti with a mean grain size of around 120 nm, the ultimate tensile strength of 980 MPa and elongation to fracture of 12% [7]. Islamgaliev *et al.* observed that as a result of isothermal HPT processing at 300 ^{o}C the ultimate tensile strength of CP Ti was up to 1600 MPa while the ductility was around 5% [8]. Ti-6Al-4V alloy processed by HPT exhibited ultrafine grains of 100-200 nm, outstanding room temperature tensile strength of 1.5 GPa and superplastic elongation of up to 500 % [9]. Meanwhile, there are few reports on the microstructure and mechanical properties of β-Ti alloys that processed by HPT.

The motivation of the present study is to investigate the evolution of the microstructure and mechanical properties of Ti-5553 alloy processed by HPT with different shear strainings.

2.2 Experimental procedures

2.2.1 Materials preparation

An ingot of Ti-5553 alloy was prepared by cold crucible levitation melting (CCLM) furnace. The size of the ingot was about 70 mm in diameter and 60 mm in length and the weight is around 1.2 kg. CCLM furnace

is a type of induction melting furnace which is very useful for preparing alloys with a uniform composition. The schematic illustration of CCLM furnace is shown in Fig. 2.1. The oxygen-free and high-purity copper segments are used to make the water-cooled crucible. There are two coils (upper and lower coils) wrapping around the crucible and connecting separately to a high frequency inverter power supply. High frequency current flows through the coils. Eddy currents are induced in the crucible and in the metals to be melted. The metals in the crucible are levitated with electromagnetic repulsion forces. The eddy currents generate joule heat in the crucible and metals, and the metals can be melted. There are three advantages of CCLM furnace, showing as follows:

(1) Metals are melted without contamination because metals are levitated in a crucible.

(2) Metals with a high melting point can also be melted.

(3) The strong stirring effect by an electromagnetic force enables an alloy of uniform composition.

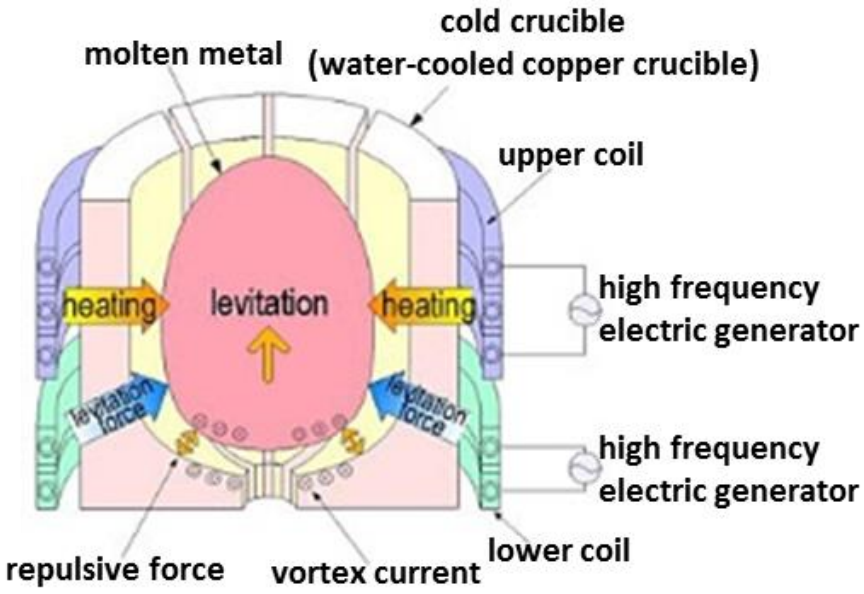

Fig. 2.1 Schematic illustration of CCLM furnace [10].

Fig. 2.2 shows a schematic drawing of the heat treatment of Ti-5553 alloy. The ingot was homogenized at 1200 ^{o}C for 3.6 ks, hot forged at 1200 ^{o}C in to a 40 mm square block and then hot rolled into a 17 mm square bar, followed by air cooling. Then the bar was wrapped by a Mo foil and treated at 1200 ^{o}C for 10.8 ks, followed by water quenching. All the heat treatments were carried out in air. After grinding the oxide layer on the surface, the bar was cold swaged to the diameter of 10 mm. Then the chemical composition of the Ti-5553 bar was measured, which is shown as Ti-5.04Al-5.14Mo-4.91V-3.04Cr (mass%). The bar was solution treated (ST) above the β transus temperature, which is 856 ^{o}C, at 1000 ^{o}C for 3.6 ks. The solution treatment was performed in an Ar atmosphere and followed by water quenching. The disks for HPT processing were sliced from the bar with a thickness of 0.85 mm. HPT processing was carried out under a compressive pressure of 5 GPa and a rotation speed of 0.2 rpm. And the rotation number of HPT processing

(*N*) was ranging from 1/2 to 20.

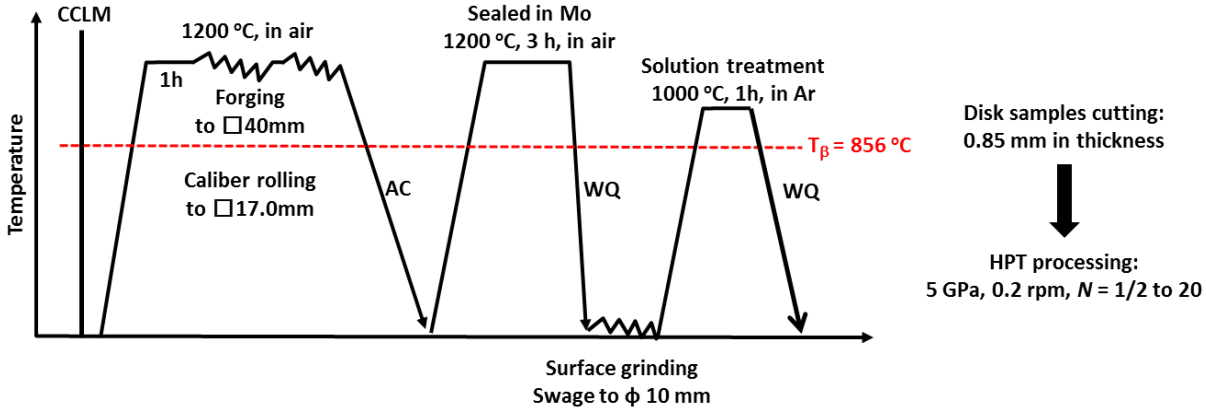

Fig. 2.2 Schematic drawing of the heat treatment of Ti-5553 alloy.

2.2.2 Materials characterization

Planar samples were mechanically ground down to roughly the median plane and polished to mirror surface for X-ray diffraction (XRD) characterization performing on a RIGAKU RINT-TTR3 diffractometer with Cu-Kα radiation (40 kV, 150 mA). The microstructural characterization was carried out using optical microscopy (OM), scanning electron microscopy (SEM, JSM-7001F), transmission electron microscopy (TEM, JEM-2100F, 200 kV) and low-angle annular dark field scanning transmission electron microscopy (LAADF-STEM, Tecnai G2 F30, 300 kV). OM and SEM observations (backscattered electron (BSE) images) were carried out on the cross-section of the sample, and samples were prepared by conventional mechanical grinding and polishing. Samples for OM observations were etched by a mixture of HNO_3: HF: H_2O = 8:2:90 in volume percent. Disk samples for TEM analysis and LAADF-STEM analysis were cut from the median plane and polished by double-jet electropolishing at a temperature of -45 °C in the solution of the following compositions: 6%$HClO_4$, 30%$C_4H_{10}O$ and 64%CH_3OH in volume.

Vickers microhardness measurements were carried out with an applied load of 0.98 N for 15 seconds along the radius of the disks on the cross-section. And the hardness was measured on the position 1/4 and 1/2 of the thickness, which is about the surface region and the central region, respectively. The schematic illustration of microhardness measurements on the cross-section is shown in Fig. 2.3.

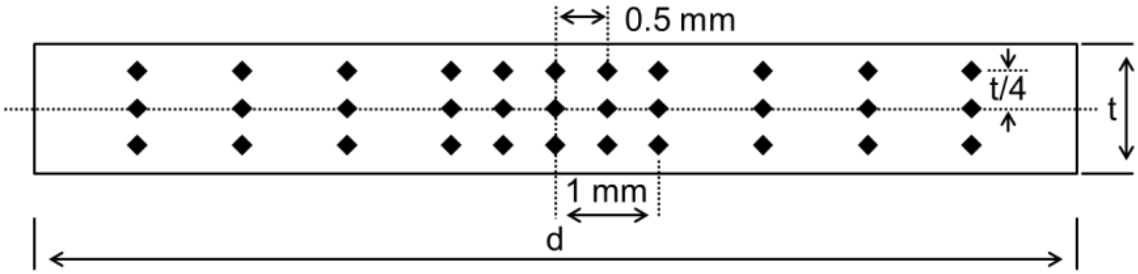

Fig. 2.3 Schematic illustration of Vickers microhardness on the cross-section.

The miniature tensile specimens with a gauge section of 4 mm x 1 mm x 0.6 mm, as shown in Fig. 2.4,

were cut by electron discharge machine (EDM) from the disks so that the center of the gauge section locates at the position 1.5 mm away from the disk center. The tensile specimens were electrochemical polished to make sure a smooth surface. The tensile tests were carried out at room temperature with a strain rate of 2 x 10^{-3} s^{-1} and the strain was monitored by video-extensometer with 3 μm resolution.

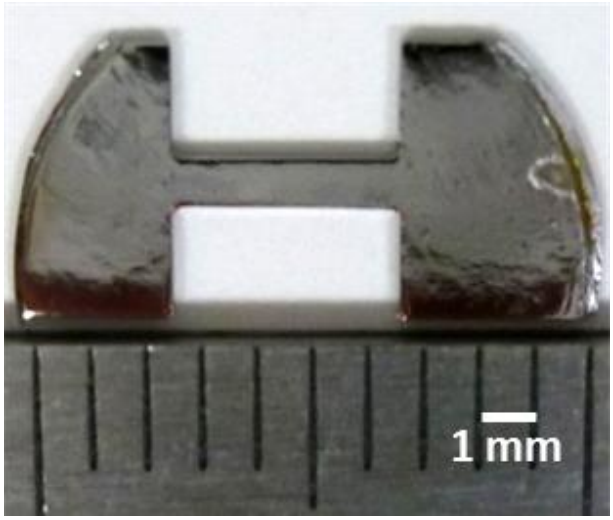

Fig. 2.4 Specimen for tensile-testing (the gauge size is 4 mm x 1mm x 0.6 mm).

2.3 Results and discussion

2.3.1 Microstructural evolution

XRD profiles of the Ti-5553 samples after ST and HPT processing with different revolutions are shown in Fig. 2.5(a). The peaks of β phase are indicated in the XRD profiles. In comparison with the ST samples, the HPT processed samples exhibit a marked decrease in the peak intensity. The main peak corresponds to the one for β{110} after HPT processing. Fig. 2.5(b) shows the change in the {211}/{110} diffraction intensity ratio (I_{211}/I_{110}) with increasing the revolutions of HPT processing. The I_{211}/I_{110} value is 1.03 for the ST sample and shows a significant decrease after HPT processing. The relatively intensity of the main reflection peaks in an XRD patterns indicates the presence of texture introduced by the shear strain during HPT processing. The texture obtained by the shear strain during HPT processing is {110}. As reported by Hosokawa *et al*. [11] that the {110} texture introduced by HPT processing in the pure iron with BCC structure is parallel to the disc plane. Indeed, several researchers have also reported that the shear deformation texture is composed of {110}<112> and {110}<001> in ferritic steels with BCC crystal structure [12, 13]. In addition, peak broadening can be seen in HPT processed samples, as shown in Fig. 2.5(c), indicating significant grain refinement and an increase in the density of defects such as dislocations.

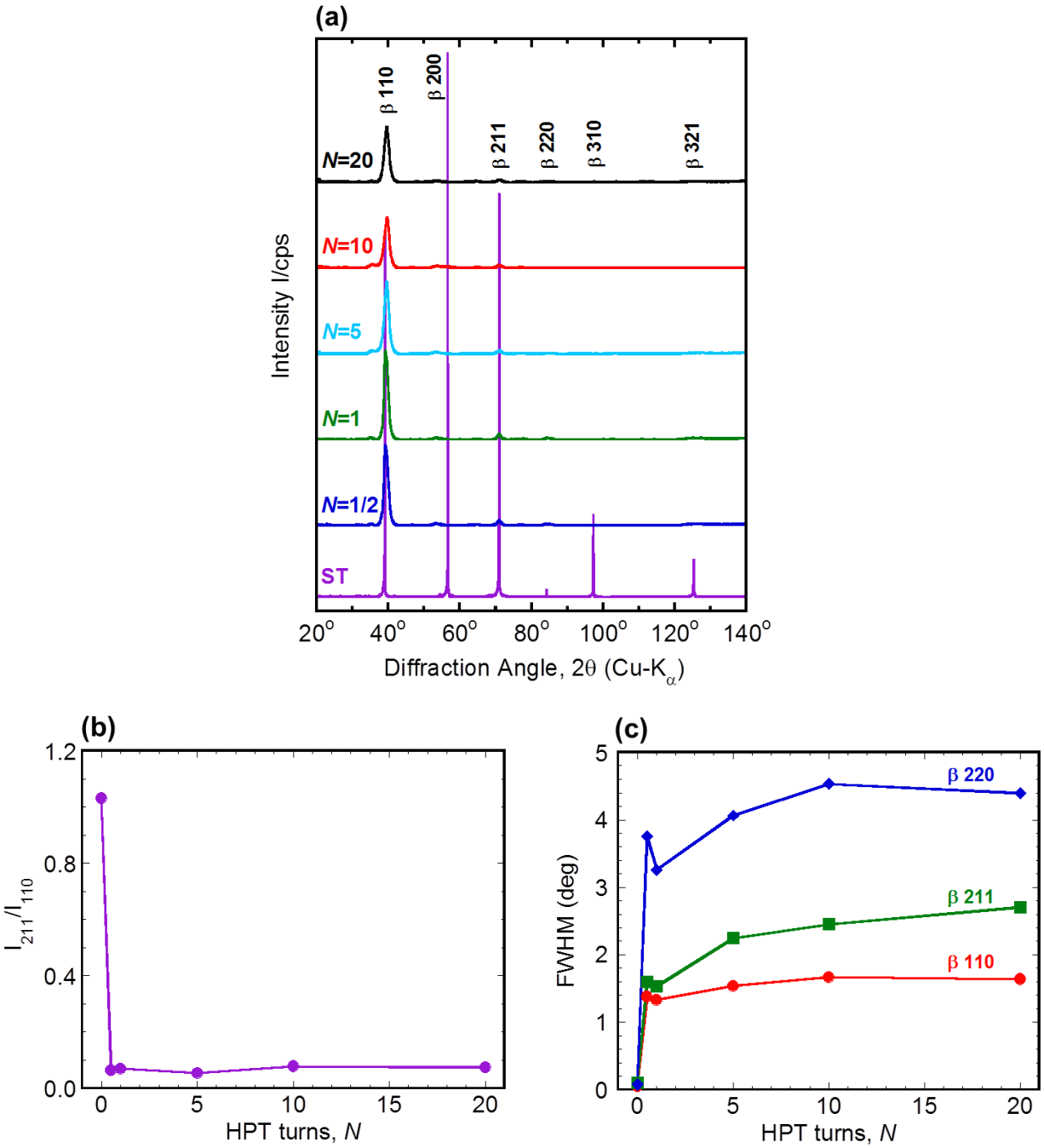

Fig. 2.5 (a) XRD patterns of Ti-5553 alloy after ST and HPT processing, (b) Change in the {211}/{110} diffraction intensity ratio (I_{211}/I_{110}) with increasing HPT turns, and (c) Change in the full width at half maximum (FWHM) with increasing HPT turns.

The OM observations on the etched cross-section of the Ti-5553 samples after ST and HPT processing with different revolutions are shown in Fig. 2.6. Coarse β phase with an average grain size of around 220 μm can be seen in the sample subjected to ST. After HPT processing, the microstructure on the cross-section exhibits different structures in the middle region and near the both sides of the surface. The microstructure in the middle region consists of a white band structure aligned into radial direction, which is called as white etching layer (WEL). The formation of the WEL is considered to be due to their high resistance to etching.

The OM observations also indicate that the WEL starts to form on the head region of the cross-section (as shown by the microstructure of the Ti-5553 sample subjected to HPT of 1/2 revolution) and then expands to the center region of the cross-section with increasing the HPT revolutions. It is clearly that the thickness of the WEL increases with increasing the HPT revolutions. After HPT processing of 10 or 20 revolutions, the WEL microstructure is the most dominant on the cross-section, implying a very homogeneous deformation.

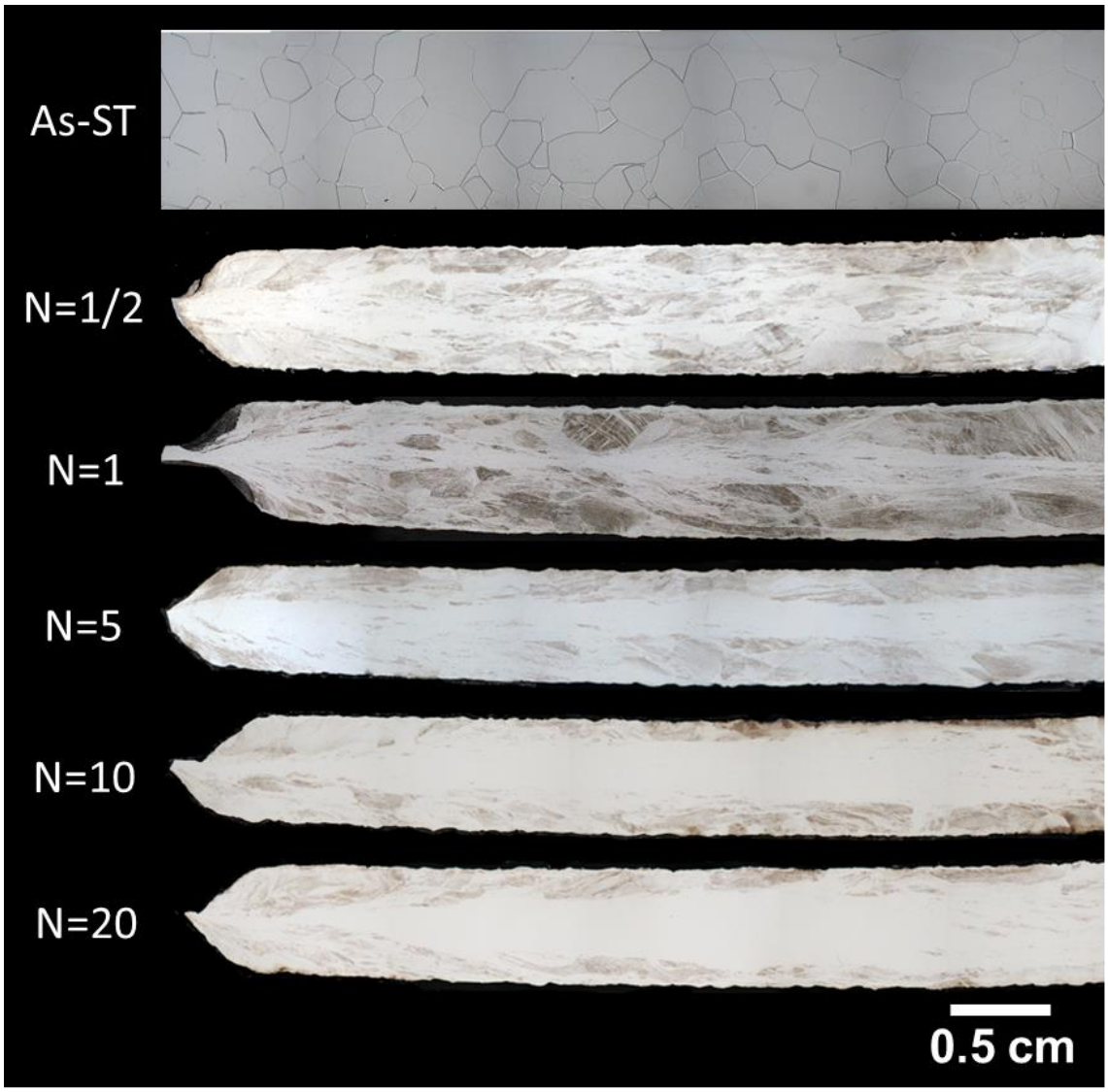

Fig. 2.6 Optical micrographs on the cross-section of Ti-5553 alloy after ST and HPT processing.

Details of the microstructures were further studied by backscatter electron SEM observation on the cross-section of the sample subjected to HPT processing of 10 revolutions, as shown in Fig. 2.7. Fig. 2.7(a) shows the SEM image contains the microstructure outside (upper region) and inside (lower region) the WEL. The microstructure outside the WEL shows numerous shear bands passing through the β grains. The shear bands show a bright contrast and the β grains show a dark contrast. The microstructure inside the WEL is uniform and featureless, showing a bright contrast. The enlarged views on the microstructure outside and inside the WEL are shown in Fig. 2.7(b) and (c), respectively. It is clearly that the deformation inside the WEL is more intense and homogeneous. And it is considered that the coalescing and the accumulation of the

shear bands during HPT processing results in the formation of WEL.

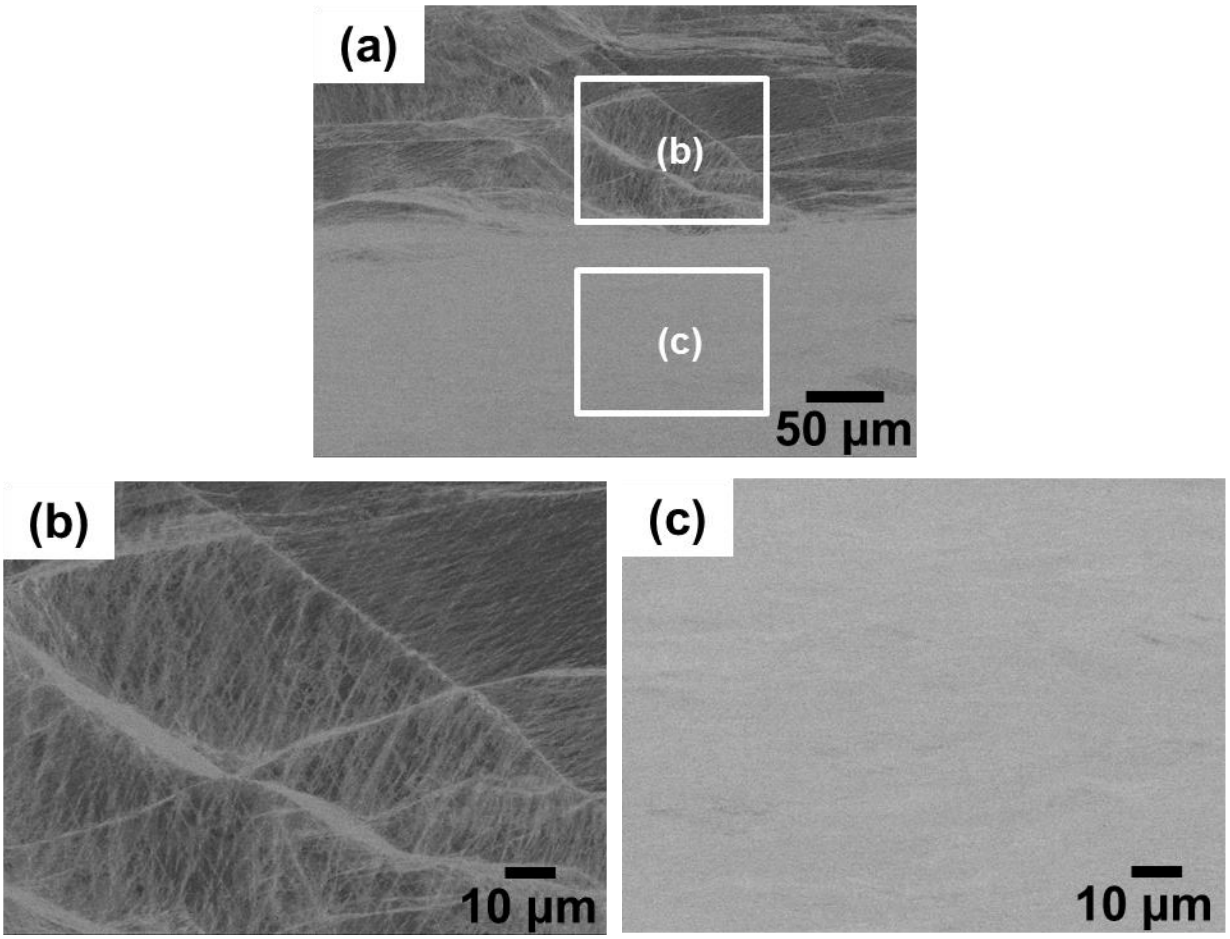

Fig. 2.7 (a) Backscatter electron SEM micrographs on the cross-section of Ti-5553 alloy subjected to HPT processing of 10 revolutions. (b) Enlarged view outside the WEL. (b) Enlarged view inside the WEL.

The microstructure inside the WEL after HPT processing of different revolution was also investigated by TEM. Fig. 2.8(a) and (b) respectively show the bright field (BF) micrographs with the selected area electron diffraction (SAED) patterns as an insert and corresponding dark field (DF) micrographs in the sample subjected to HPT processing of 1 turn. It is evident that an ultrafine-grained microstructure is obtained. Complex strain contrast, which possibly originates from a high density of dislocations uniformly distributed, can be seen from both the BF image and DF image. The SAED pattern appears as Debye-Scherrer rings with the distortion of diffraction spots along the hoop direction suggests a high degree of lattice distortions associated with a large internal stress. They also imply that the ultrafine-grained microstructure is of large misorientations. The diameter of the rings corresponds to those for β phase and no diffraction rings from ω phase can be detected. It is should be noted that it is rather difficult to determine the true grain size in such severely deformed TEM microstructure, because the grain boundaries are not well-defined and grains are highly strained. The small bright areas on the DF image are not single grains but only a part of grains. By increasing the HPT processing to 10 turns (Fig. 2.8(c) and (d)) and 20 turns (Fig, 2.8(e) and (f)), the samples show a more ultrafine-grained and homogeneous microstructure.

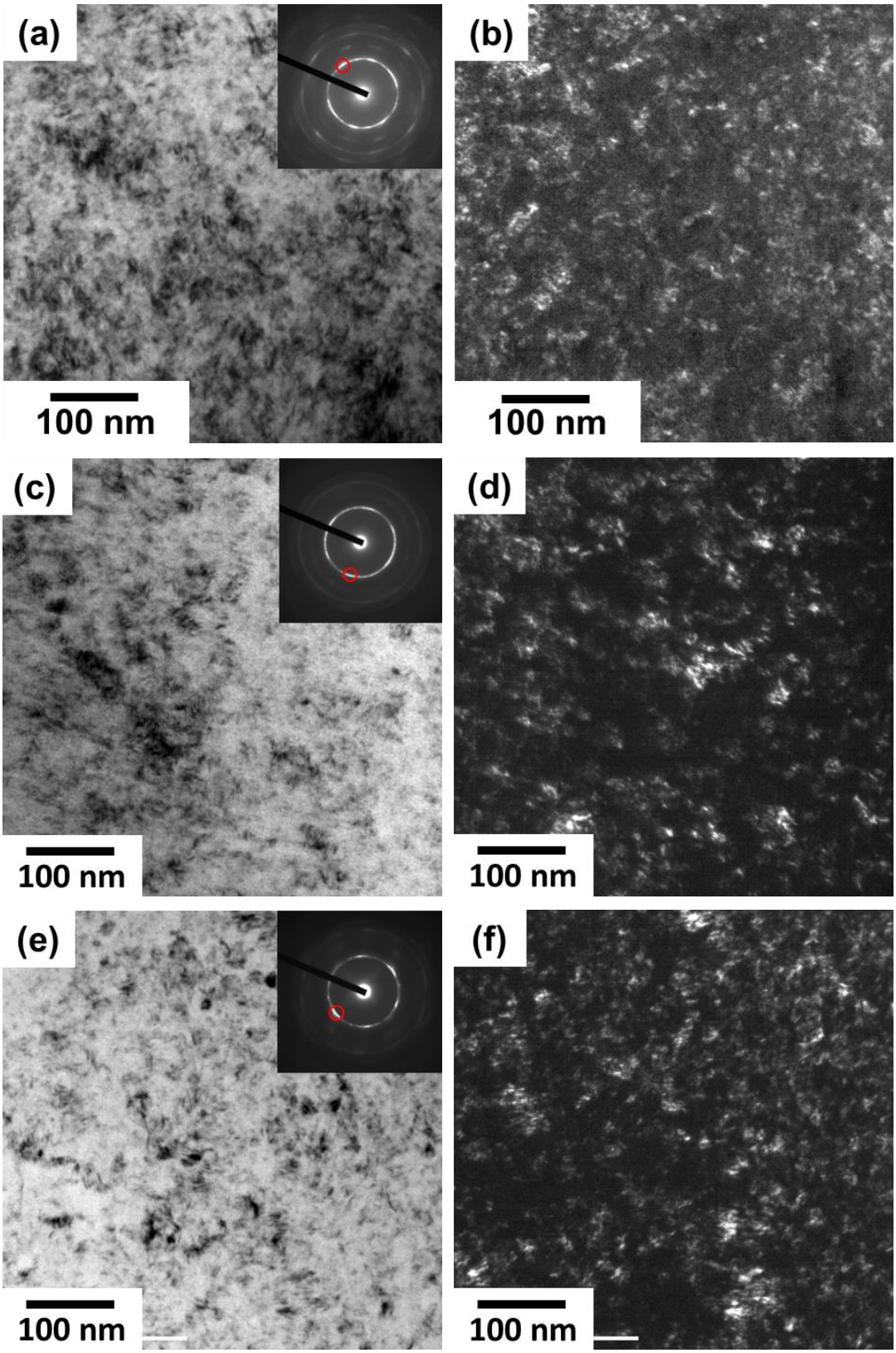

Fig. 2.8 Bright field (BF) micrographs with the selected area electron diffraction (SAED) pattern as an insert and corresponding dark field (DF) image of Ti-5553 alloy subjected to HPT processing of different turns: (a, b) N = 1, (c, d) N = 10 and (e, f) N = 20.

In order to further investigate the ultrafine-grained microstructure inside the WEL, low-angle annular dark-field scanning transmission electron microscopy (LAADF-STEM) observations were performed. Fig. 2.9 shows the LAADF-STEM images inside the WEL in the sample subjected to HPT processing of 10 turns. It is still difficult to see the separate grains with well-defined grain boundaries from these LAADF-STEM images. However, dislocation cells with the grain around 20 nm can be detected.

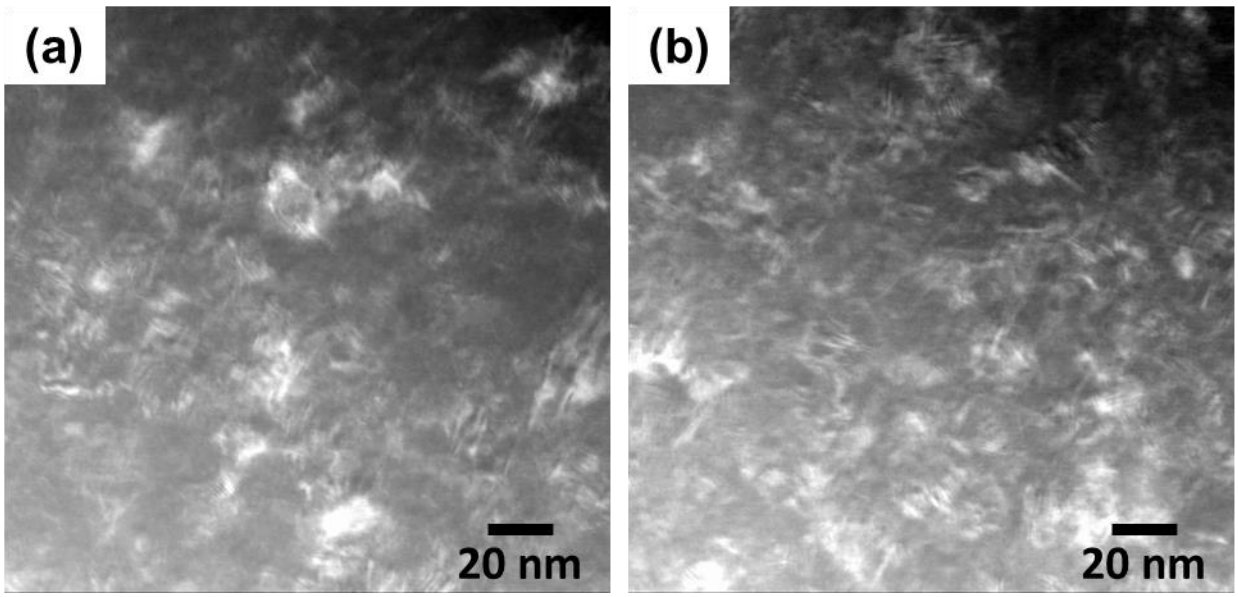

Fig. 2.9 (a) and (b) the LAADF-STEM microstructure inside the WEL in the sample subjected to HPT processing of 10 turns.

2.3.2 Mechanical properties

The evolution of microhardness on the cross-section is plotted as a function of distance from the center, as shown in Fig. 2.10(a). The level of microhardness in ST sample is indicated by the broken line. It is clearly that HPT processing can increase the hardness significantly. After HPT processing of 1/2 revolution, the distribution of hardness on the cross-section is inhomogeneous. The hardness is lower in the center region and higher in the edge region of the disk. But the hardness becomes homogeneous across the cross-section of the disk by continuous HPT processing to the higher number of turns. Results of the average microhardness of Ti-5553 alloy after ST and HPT processing are summarized in Fig. 2.10(b). The average hardness of the sample after ST is 288.1 ± 5.3 *H*v and the hardness increases to 329.8 ± 17.3 *H*v after HPT processing of 1/2 turn. The hardness shows a continuous increase with increasing the turns of HPT processing and a saturated hardness can be achieved after HPT processing of 10 turns with a value of 380.7 ± 20.7 *H*v.

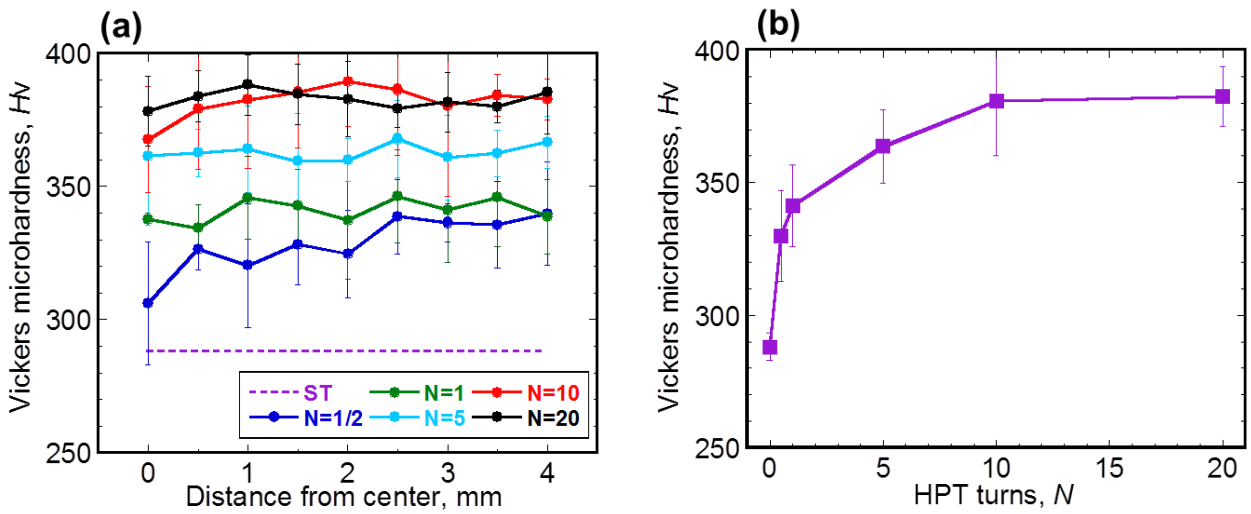

Fig. 2.10 (a) the evolution of microhardness on the cross-section as a function of distance from the center, (b) the evolution of average microhardness as a function of HPT turns.

The large scatters of deviation in the hardness are due to the different deformed structure inside and outside the WEL which should have different hardness. The optical micrograph in Fig. 2.11 shows the measured hardness inside and outside the WEL in the sample subjected to HPT processing of 5 turns. The different microstructure inside and outside the WEL can be seen. It also shows the indentations from the microhardness measurements and numbers on the side indicate the microhardness values of each indentation. It is obvious that the hardness is much higher inside the WEL than outside the WEL. The average hardness is 394.9 ± 2.9 *H*v inside the WEL and 337.7 ± 8.7 *H*v outside the WEL.

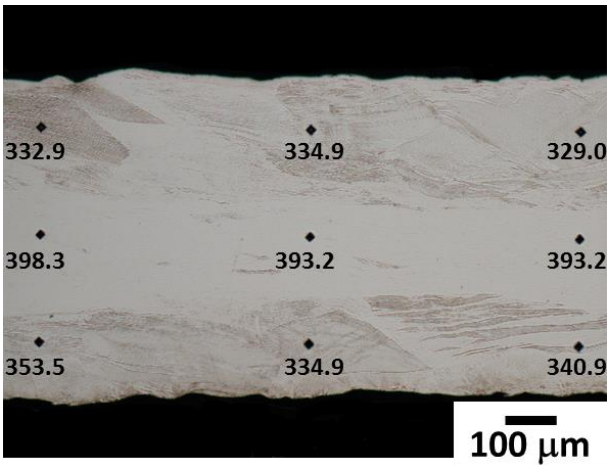

Fig. 2.111 Optical micrograph of Ti-5553 alloy subjected to HPT processing of 5 turns. The numbers indicate the microhardness value of each indentation.

Fig. 2.12 shows the tensile stress-strain curves of Ti-5553 alloy after ST and HPT processing. For the ST sample, the ultimate tensile strength and elongation to failure are 924 MPa and 14.6%, respectively. The first 1 turn of HPT processing changes the stress-strain curve drastically. By the HPT processing of 1/2 turn, the ultimate tensile strength increases a little but the ductility is lost significantly. Following the yield and

rapid work hardening, the flow stress decreases to about 4% strain. This is a typical behavior in ultrafine grained materials. After applying the HPT processing of 1 to 20 turns, the ultimate tensile strength increases markedly accompanied with a brittle failure. The ultimate tensile strength after HPT processing of 10 turns can be up to 1470 MPa.

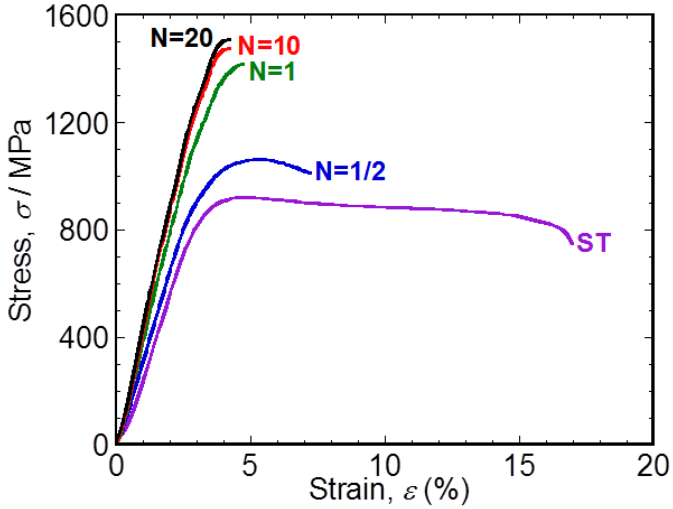

Fig. 2.12 Tensile stress-strain curves of Ti-5553 alloy after St and HPT processing.

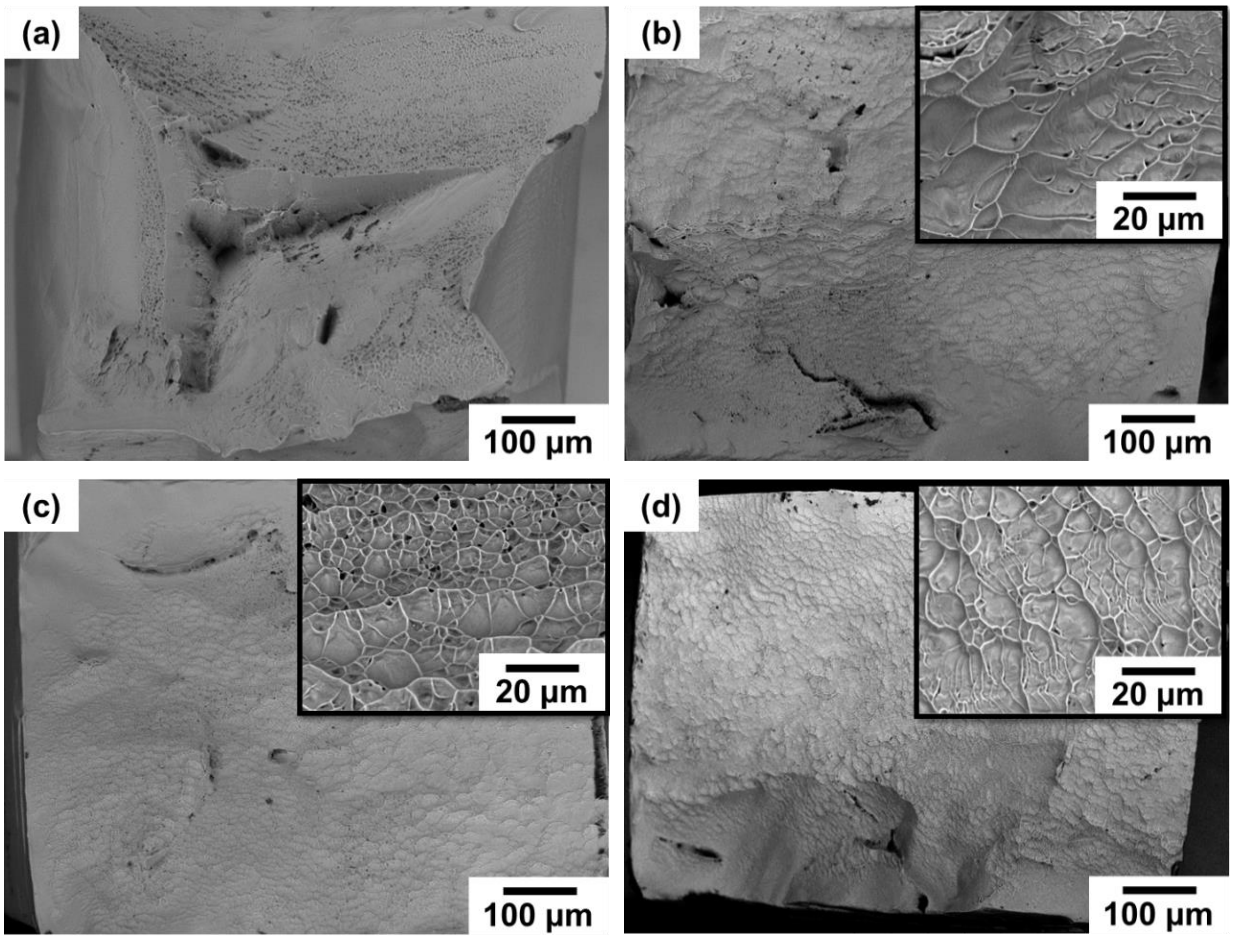

Fig. 2.13 SEM images of the fracture surface: (a) ST, (b) *N*= 1/2, (c) *N* = 1 and (d) *N* = 10.

Fig. 2.13 shows the SEM images of the fracture surface. Fig. 2.13(a) shows the fracture surface of the ST sample. A big and deep pit is observed in the central region, and it is considered to be the crack source. For the HPT processed samples, the fracture surface is flat and covered with small dimples, as shown in Fig. 2.13(b) to (d).

The increase in the hardness and ultimate tensile strength by HPT processing is due to the reduction in grain size and the increase in the dislocation density. The grain refinement strengthening can be explained by the Hall-Petch equation [14, 15] and the dislocation strengthening can be explained by the Taylor equation [16]. Accompanied by an increase in the strength, there is a sharp decrease in the ductility. As reported previously [17], the low ductility of many ultrafine-grained materials is often attributed to the relatively fine grain size. The movement of the dislocations is most likely to be limited due to the strong interactions of dislocations within nanoscale grains, consequently leading to a low ductility. In the HPT processed Ti-5553 alloy, the WEL and shear banded regions should have the finest grains and the highest density of dislocations because of the localized intense deformation. So it is considered that the mechanical properties of HPT processed Ti-5553 alloy are mostly dominated by the shear banded region and the WEL.

2.4 Summary

In this chapter, the effects of HPT processing on the evolutions of microstructure and mechanical properties in Ti-5553 alloy were studied.

(1) HPT processing produced numerous shear bands which increase with the HPT rotation numbers, forming a white etching layer (WEL) in the middle region of the cross-section. The thickness of WEL increased with increasing HPT turns and the WEL became the most dominant structure after HPT processing of 10 turns.

(2) The microstructure analysis showed that an ultrafine-grained microstructure with high density of dislocations was obtained by HPT processing. The dislocation seems to distribute uniformly in the β grains without forming the subgrains. The low-angle annular dark field observations indicated the formation of dislocation cells.

(3) The grain refinement and high density of dislocations led to an increase in the hardness and ultimate tensile strength, accompanied by a sharp loss in the ductility.

2.5 References

[1] R.R. Boyer, An overview of the use of titanium in the aerospace industry, Mater. Sci. Eng. A 213 (1996) 103-114.

[2] I. Weiss, S.L. Semiatin, Thermomechanical processing of beta titanium alloys – an overview, Mater. Sci. Eng. A 243 (1998) 46-65.

[3] S. Ankem, C.A. Greene, Recent developments in microstructure/property relationships of beta titanium alloys, Mater. Sci. Eng. A 263 (1999) 127-131.

[4] R.R. Boyer, R.D. Briggs, The use of β titanium alloys in the aerospace industry, J. Mater. Eng. Perform. 14 (2005) 681-685.

[5] N. Clement, A. Lenain, P.J. Jacques, Mechanical property optimization via microstructural control of new metastable beta titanium alloys, JOM 59 (2007) 50-53.

[6] A.P. Zhilyaev, T.G. Langdon, Using high-pressure torsion for metal processing: fundamentals and applications, 53 (2008) Prog. Mater. Sci. 893-979.

[7] R.Z. Valiev, A.V. Sergueeva, A.K. Mukherjee, The effect of annealing on tensile deformation behavior of nanostructured SPD titanium, Scripta Mater. 49 (2003) 669-674.

[8] R.K. Islamgaliev, V.U. Kazyhanov, L.O. Shestakova, A.V. Sharafutdinov, R.Z. Valiev, Microstructure and mechanical properties of titanium (Grade 4) processed by high-pressure torsion, Mater. Sci. Eng. A 493 (2008) 190-194.

[9] A.V. Sergueeva, V.V. Stolyarov, R.Z. Valiev, A.K. Mukherjee, Superplastic behavior of ultrafine-grained Ti-6Al-4V alloys, Mater. Sci. Eng. A 323 (2002) 318-325.

[10] A. Moritaa, H. Fukuib, H. Tadanoa, S. Hayashia, J. Hasegawab, M. Niinomic, Alloying tatinium and tantalum by cold crucible levitation melting (CCLM) furnace, Mater. Sci. Eng. A 280 (2000) 208-213.

[11] A. Hosokawa, S. Ii, K. Tsuchiya, Work hardening and microstructural development during high-pressure torsion in pure iron, Mater. Trans. 55 (2014) 1097-1103.

[12] J. Baczynski, J.J. Jonas, Texture development during the torsion testing of α-iron and two IF steels, Acta Mater. 44 (1996) 4273-4288.

[13] E. Aernoudt, J.G. Sevillano, Influence of mode of deformation on hardening of ferritic and pearlitic carbon-steels at large strains, J. Iron Steel Inst. 211 (1973) 718-725.

[14] E.O. Hall, Yield point phenomena in metals and alloys, Plenum Press, New York (1970).

[15] T.G. Nieh, J. Wadsworth, Hall-Petch relation in nanocrystalline solids, Scripta Metal. Mater. 25 (1991) 955-958.

[16] L. Balogh, R.B. Figueiredo, T. Ungar, T.G. Langdon, The contributions of grain size, dislocation density and twining to the strength of a magnesium alloy processed by ECAP, Mater. Sci. Eng. A 528 (2010) 533-538.

[17] B.Q. Han, E.J. Lavernia, F.A. Mohamed, mechanical properties of nanostructured materials, Rev. Adv. Mater. Sci. 9 (2005) 1-16.

Chapter 3 Precipitation of α phase in HPT processed Ti-5553 alloy by isothermal aging

3.1 Introduction

The grain refinement strengthening and dislocation strengthening are important strengthening mechanisms for metastable β-Ti alloys, as discussed in chapter 2. However, the most commonly used strengthening mechanism for β-Ti alloys is the precipitation/dispersion strengthening mechanism. The second phases precipitated by aging include the metastable ω phase formed at lower aging temperatures and α phase formed at higher aging temperatures. Since the precipitation of ω phase usually leads to severe embrittlement [1-3], the α phase plays a more important role in strengthening β-Ti alloys.

The precipitation of α phase in β-Ti alloys processed by severe plastic deformation (SPD) has been reported by Xu *et al*. [4, 5]. They reported that ultrafine equiaxed α phase formed in the ECAP or HPT processed Ti-20mass%Mo alloy after aging instead of the coarse acicular α phase. The increased disorder originating from the excess vacancies resulted in a more random rather than the Burgers orientation relationship between the α phase and β matrix. And the enhanced the diffusivity facilitated a rapid growth of the α nuclei into equiaxed precipitates. However, the formation and growth process of the equiaxed α phase were not studied in details.

The growth of α phase requires the partitioning of the alloying elements between α phase and β phase. For the Ti-5553 alloy, aluminum is known to be an α stabilizer, while other alloying elements, such as Mo, V and Cr, are β stabilizers. The present research will be devoted to the growth process and compositional evolution of the equiaxed α phase in the HPT processed Ti-5553 alloy. The crystallographic orientation relationship between equiaxed α phase and β phase will also be discussed. Moreover, as a comparison, the formation and growth of acicular α phase in the Ti-5553 alloy without HPT processing will also be presented. After aging at various conditions, the α phase in the Ti-5553 alloy with or without HPT processing should have different volume fraction, particle size, distribution and morphology. The effects of the α phase on the mechanical properties will be discussed.

3.2 Experimental procedures

3.2.1 Materials preparation

The Ti-5553 alloy was prepared and processed as shown in Section 2.2.1 and 2.2.2. The Ti-5553 alloy

was solution treated (ST) above the β transus temperature, which is 856 ºC, at 1000 ºC for 3.6 ks. HPT processing was carried out under a compressive pressure of 5 GPa, a rotation speed of 0.2 rpm and the rotation number of HPT processing (*N*) was $N = 10$. For the solution treated samples or the HPT processed samples, isothermal aging was performed at various temperatures ranging from 450 ºC to 750 ºC for 14.4 ks or performed at 650 ºC for various time ranging from 0.3 ks to 360 ks. The ST and isothermal aging were performed in an Ar atmosphere and followed by water quenching. Hereafter, the solution treated samples are referred to as ST samples and the HPT processed samples are referred to as HPT samples.

3.2.2 Materials characterization

Microstructural characterization was carried out using scanning electron microscopy (SEM, JEOL JSM-7001F, 20 kV) and transmission electron microscopy (TEM, JEOL JEM-2100, 200 kV). Backscattered electron (BSE) SEM observations and electron backscattered diffraction (EBSD) were carried out on the cross-sections of the samples mounted in resin and the samples were prepared by conventional mechanical grinding and polishing. The step size of EBSD was set to 20 nm. The average particle size and volume fraction of α phase were measured by the image analysis with the SEM images. Disk samples (3 mm in diameter) for TEM analysis were cut from the median plane of the disk and thinned to perforation using a Gatan precision ion polishing system.

Vickers microhardness measurements were carried out with an applied load of 0.98 N for 15 seconds along the radius of the disks on the cross-section. And the hardness was measured on the position 1/4 and 1/2 of the thickness, which is about the surface region and the central region, respectively. The schematic illustration of the microhardness measurements on the cross-section is shown in Fig. 2.3 in Section 2.2.3. The miniature tensile specimens with a gauge section of 4 mm x 1 mm x 0.6 mm, as shown in Fig. 2.4 in Section 2.2.3, were cut by electron discharge machine (EDM) from the disks so that the center of the gauge section locates at the position 1.5 mm away from the disk center. The tensile specimens were electrochemical polished to make sure a smooth surface. The tensile tests were carried out at room temperature with a strain rate of 2×10^{-3} s^{-1} and the strain was monitored by video-extensometer with 3 μm resolution.

The quantitative analysis on the composition of α phase was carried out by electron probe microanalysis (EPMA, JEOL JXA-8900F) at a voltage of 15 kV and a probe current of 10 nA. EPMA is a promising method for quantitative analysis of elemental concentrations with high sensitivity and accuracy on the sample surface. In the introduction part another chemical composition technique named Energy-dispersive spectroscopy (EDS) in SEM was also introduced for Mo content quantitation. Basically there are two types of X-ray spectroscopy, one is energy-dispersive spectroscopy (EDS) and the other one is wavelength-dispersive spectroscopy (WDS). For EPMA, WDS is used as spectroscopy for measuring characteristic X-rays because of the high sensitivity. That's the reason why EPMA is more suitable in this study for measuring the composition content of α phase with fine particle size. In the present research, at least 5 α particles were chosen in each sample and the analyzed spot size was around the order of 0.1 μm in diameter.

The nanohardness of α and β phase was measured by nanoindentation using a Hysitron Triboindenter TI950 in a load control mode. Both α and β phases were indented in at least 30 positions with a peak load of 500 μN at a loading/unloading rate of 50 μN/s. The indenter was held at peak force for 5 s before unloading. The hardness (*H*) was calculated by the Oliver and Pharr method [6], as shown by the followed equations;

$$H = \frac{P_{max}}{A_c} \qquad \text{(Eqn. 3.1)}$$

where P_{max} is the maximum load applied during nanoindentation and A_c is the contact area which can be determined from the calibrated indenter shape function. The observation of nanoindentation was performed by the scanning probe microscopy (SPM) equipped on the Hysitron Triboindenter TI950.

3.3 Results

3.3.1 Microstructural evolution in ST and HPT samples

3.3.1.1 BSE-SEM analysis

The BSE-SEM images on the cross-section of the ST samples isothermally aged at different temperatures for 14.4 ks are shown in Fig. 3.1. The morphology of α phase in the BSE-SEM images shows a dark contrast. After aging at 450 °C, as shown in Fig. 3.1(a), fine α phase precipitates. By increasing the aging temperature form 450 °C to 750 °C, the growth of α phase is obvious. And it shows that the volume fraction of α phase is lower at higher aging temperatures. As indicated in Fig. 3.1(e), the α phase formed in the ST samples includes the grain boundary (GB) α phase, intergranular α phase and transgranular α phase. The transgranular α phase shows an acicular morphology.

The BSE-SEM images on the cross-section of the HPT samples isothermally aged at different temperatures for 14.4 ks are shown in Fig. 3.2. It is important to note that these images show the morphology of α phase inside the white etching layer (WEL). The WEL was shown in Section 2.3.1. The α phase in the BSE-SEM images shows a dark contrast. There are α phase formed after aging at 450 °C. But it is difficult to see the α phase clearly in Fig. 3.2(a), because of the relatively fine particle size. The α phase can be seen clearly after aging at 550 °C, as shown in Fig. 3.2(b). The growth of α phase is evident with increasing the aging temperature; meanwhile, the volume fraction of α phase shows a decrease. The α phase formed in the HPT samples shows an equiaxed morphology and a homogeneous distribution.

The BSE-SEM images outside the WEL on the cross-section of the HPT samples aged at different temperatures for 14.4 ks are shown in Fig. 3.3. It is difficult to see the α phase after aging at 450 °C, but the precipitation of α phase can be seen clearly by increasing the aging temperature to 550 °C (Fig. 3.3 (b)) and 750 °C (Fig. 3.3(f)). There are two types of α phase formed outside the WEL. One is the equiaxed α phase formed inside the shear bands (SB) and the other one is the acicular α phase formed in the β matrix surrounding the SBs. The β matrix surrounding the SBs is not severely deformed, as discussed in Section 2.3.1 and 2.3.2.

In addition, it is important to note that, these microstructures shown in Fig. 3.3 are subordinate for the samples subjected to HPT processing of 10 turns. The dominant microstructure for the sample subjected to

HPT processing of 10 turns is the WEL. Therefore, the present research focuses on the formation of α phase inside the WEL, where the formation of α phase is shown in Fig. 3.2.

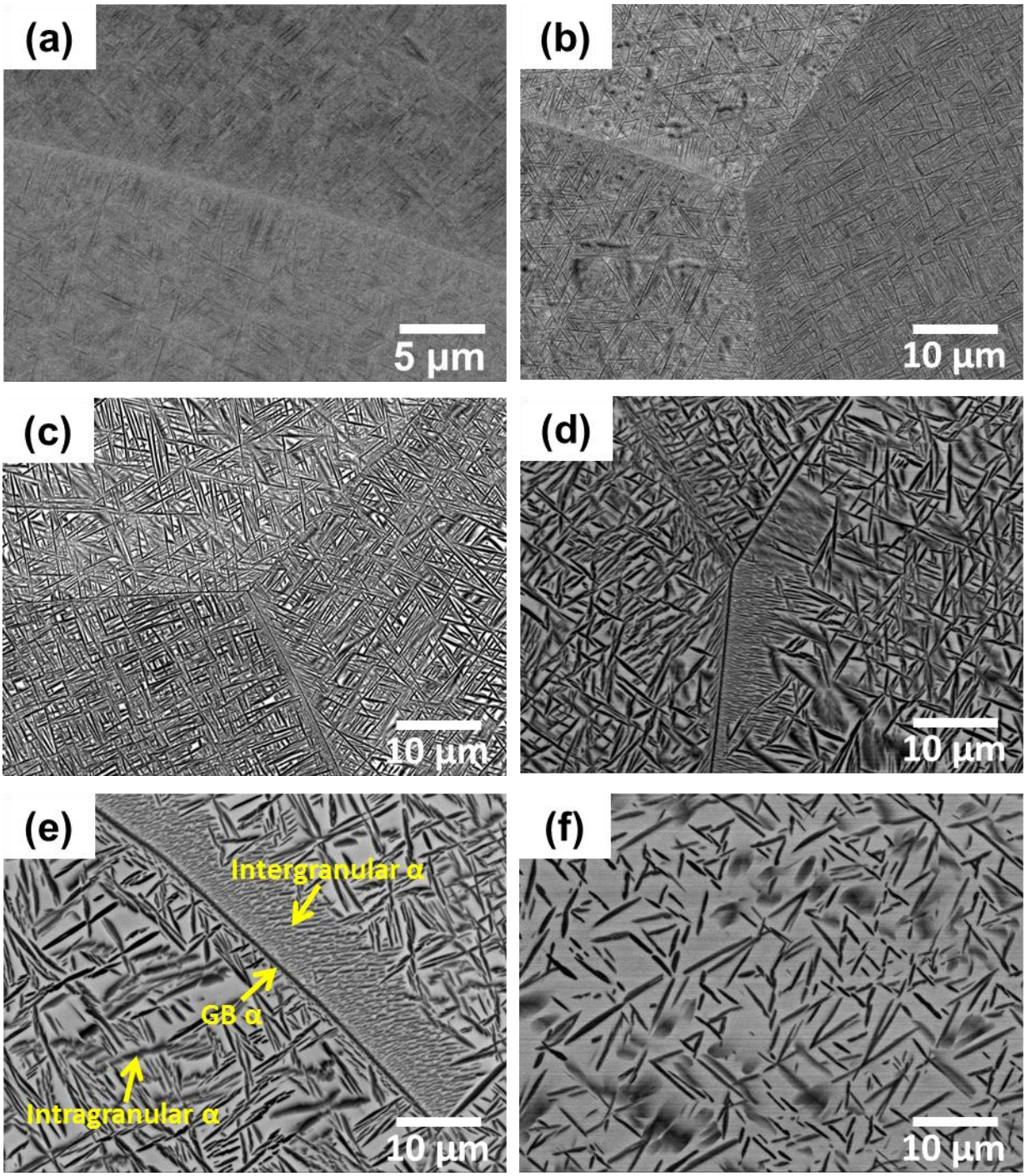

Fig. 3.1 BSE-SEM images on the morphology of α phase in the ST samples after aging at different temperatures for 14.4 ks. (a) 450 ºC, (b) 550 ºC, (c) 600 ºC, (d) 650 ºC, (e) 700 ºC, and (f) 750 ºC.

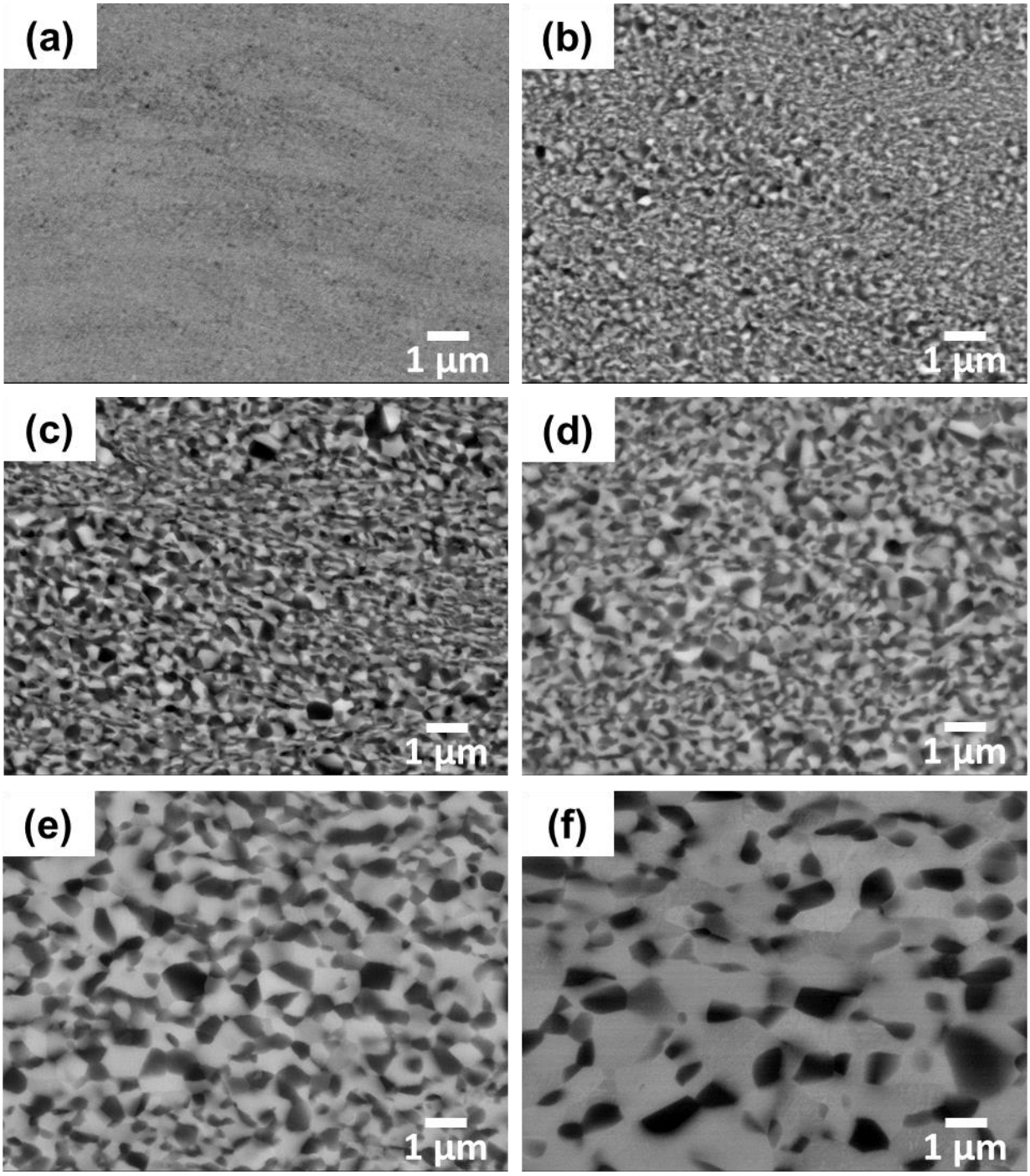

Fig. 3.2 BSE-SEM images on the cross-section of the HPT samples aged at different temperatures for 14.4 ks. (a) 450 °C, (b) 550 °C, (c) 600 °C, (d) 650 °C, (e) 700 °C, and (f) 750 °C. These images show the morphology of α phase inside the white etching layer.

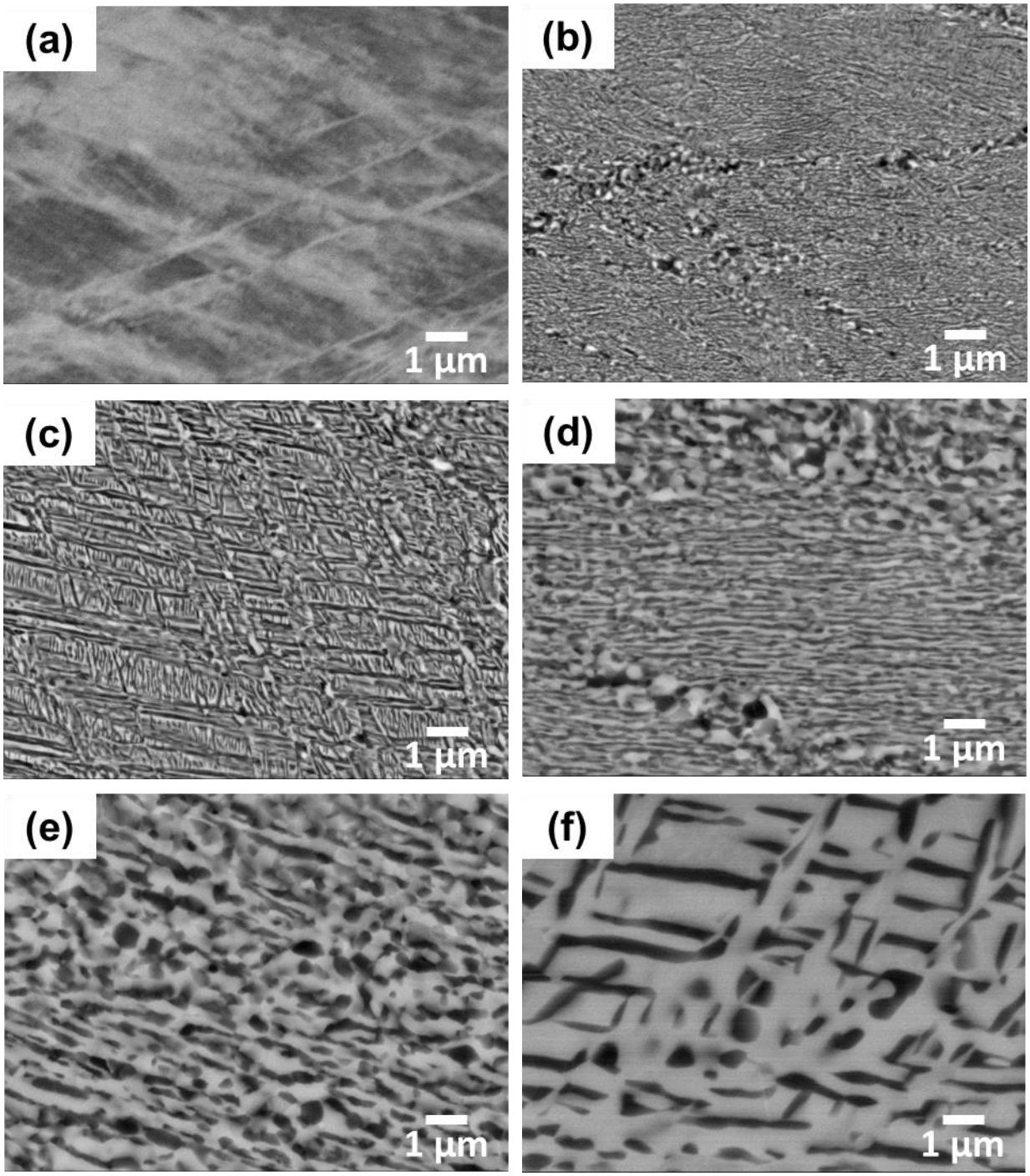

Fig. 3.3 BSE-SEM images on the cross-section of the HPT samples aged at different temperatures for 14.4 ks. (a) 450 °C, (b) 550 °C, (c) 600 °C, (d) 650 °C, (e) 700 °C, and (f) 750 °C. These images show the morphology of α phase outside the white etching layer.

The BSE-SEM images on the morphology of α phase in the ST samples isothermally aged at 650 °C for different time are shown in Fig. 3.4. After aging for 0.3 ks, as shown in Fig. 3.4(a), it is clear that the nucleation of α phase takes place preferentially at grain boundaries, forming grain boundary α phase (also named as allotriomorph α phase) which grows along the grain boundary and intergranular α phase which grows into the interior of β phase grain. The grain boundary α phase and intergranular α phase are

respectively indicated by the arrows in Fig. 3.4(a). There is a few number of intragranular α particles formed in the interior of β grain. The dense precipitation and significant growth of intragranular α phase with acicular morphology can be seen after aging for 1.2 ks, as shown in Fig. 3.4(b). Continuous aging for 360 ks, as shown in Fig. 3.4(d), leads to a growth of the intragranular α phase, especially in the thickness direction.

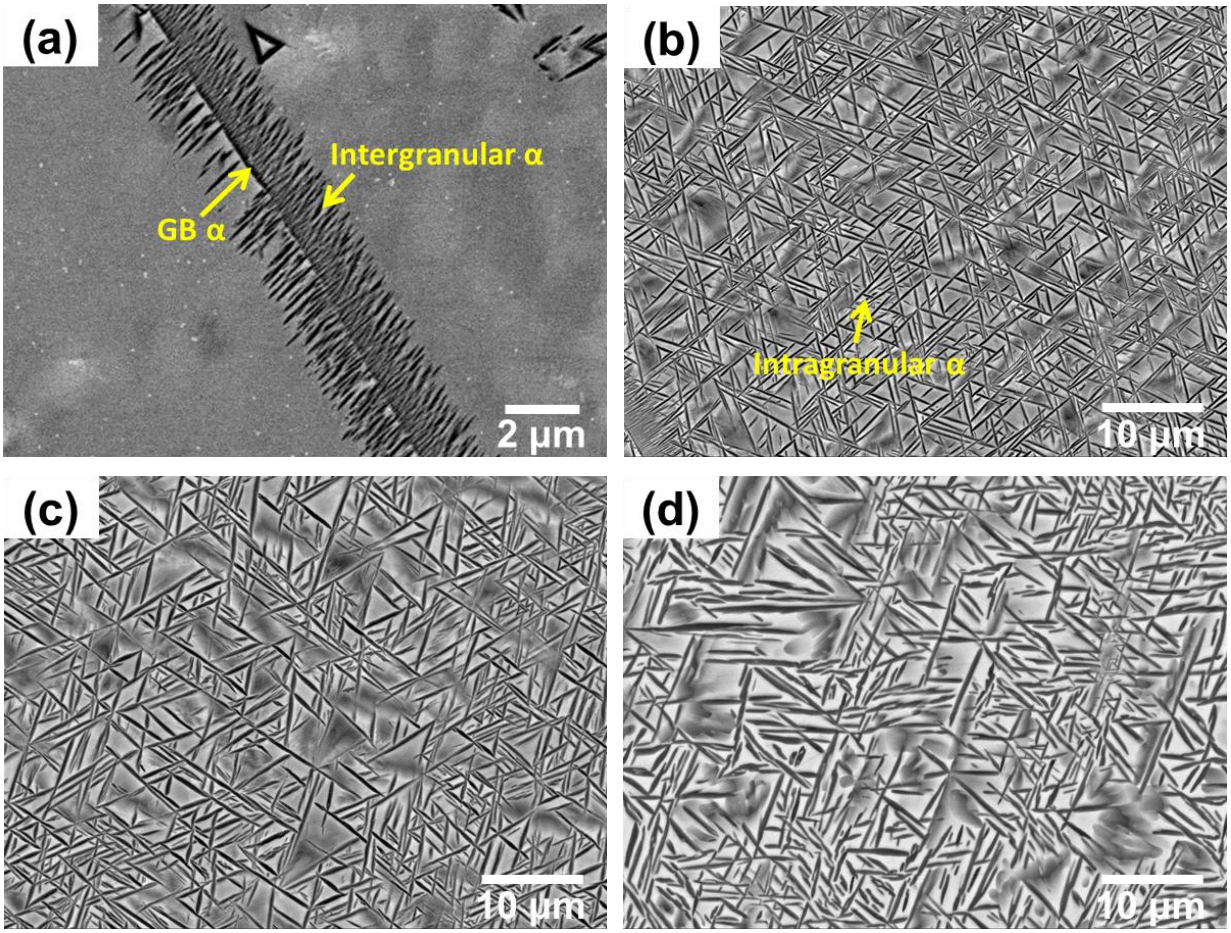

Fig. 3.4 BSE-SEM images on the morphology of α phase in the ST samples aged at 650 ºC for different time. (a) 0.3 ks, (b) 1.2 ks, (c) 3.6 ks, and (d) 360 ks.

The BSE-SEM images on the morphology of α phase in the HPT samples isothermally aged at 650 ºC for different time are shown in Fig. 3.5. After aging for 0.3 ks, as shown in Fig. 3.5(a), numerous ultrafine α particles can be seen. It suggests that the nucleation and growth of α phase in the HPT samples is much more rapid than those of α phase in the ST samples. The further growth of α phase can be seen as an increase in the aging time to 360 ks, as shown in Fig. 3.5(d). All the α precipitates show an equiaxed shape with some tendency of faceting.

The precipitation of α phase in the ST samples and HPT samples aged at 550 ºC and 750 ºC for different time were also studied. Because the similar precipitation behavior of α phase with aging at 650 ºC, these BSE-SEM images will not be shown here.

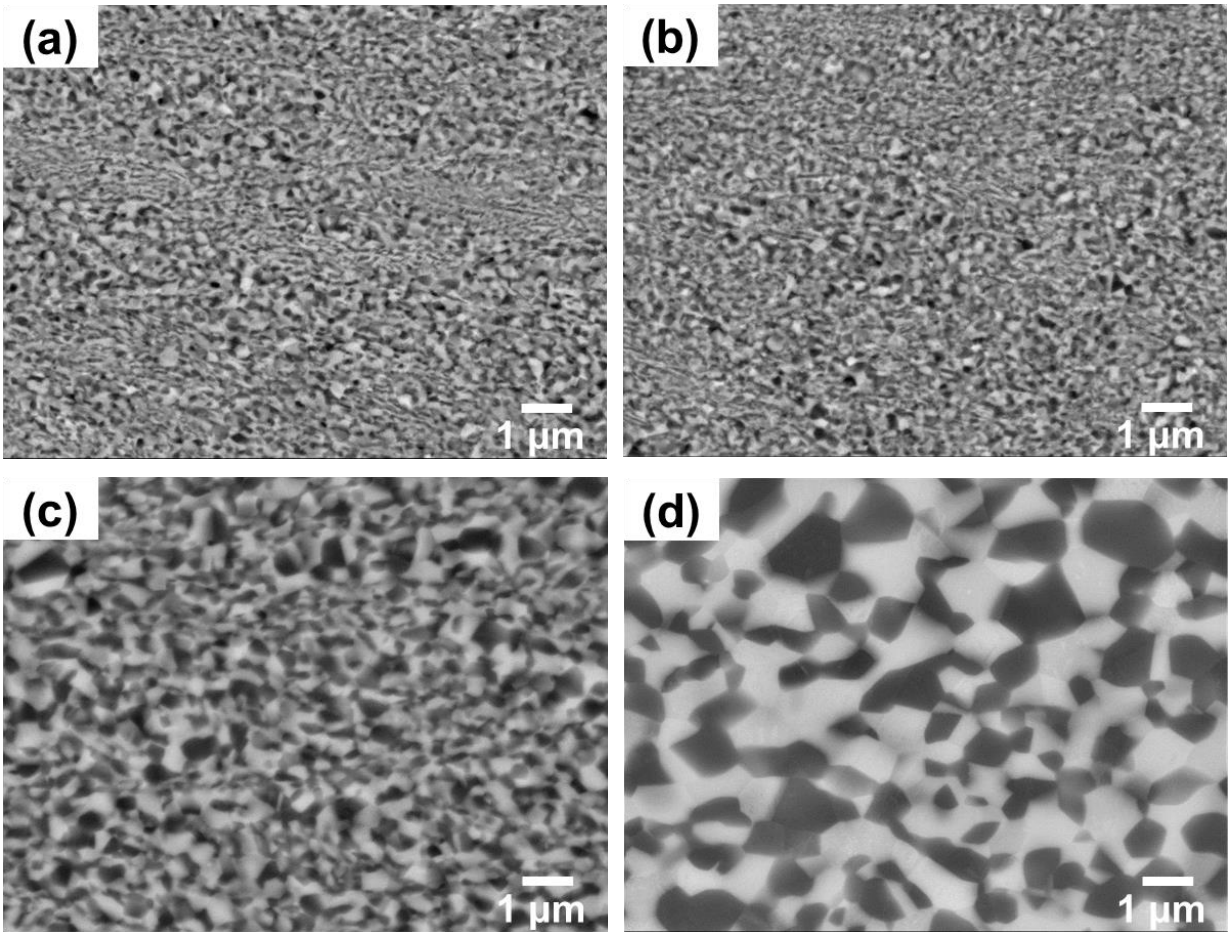

Fig. 3.5 BSE-SEM images on the morphology of α phase inside the WEL of the HPT samples aged at 650 °C for different time. (a) 0.3 ks, (b) 1.2 ks, (c) 3.6 ks, (d) 360 ks.

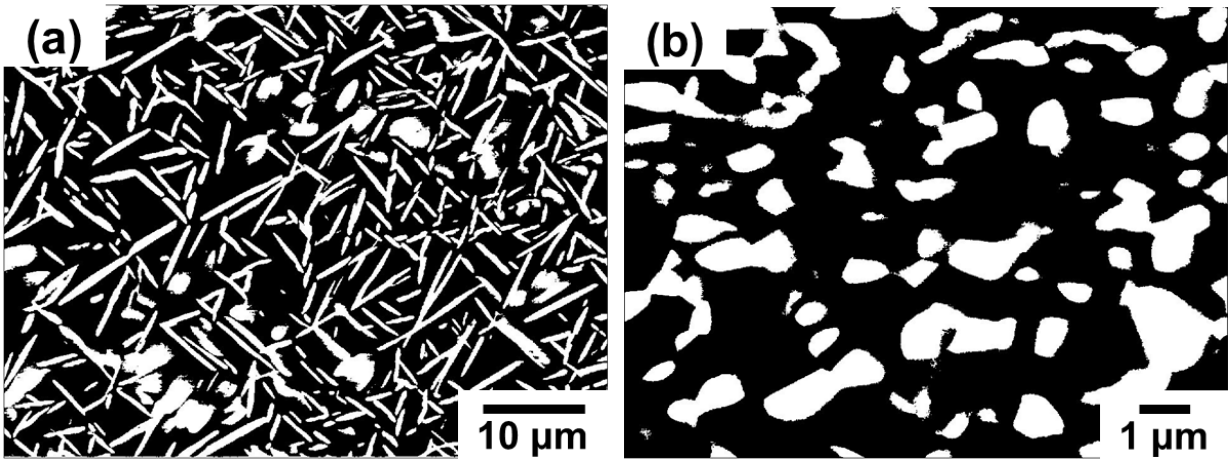

Fig. 3.6 Adjusted images by the ImageJ software for the calculation of the volume fraction of a phase (white contrast). (a) correspond to the SEM image shown in in Fig. 3.1(f) and (b) correspond to the SEM image shown in Fig. 3.2 (f).

The average particle size and volume fraction of α phase in the ST samples and HPT samples (inside the WEL) were measured by the image analysis based on the SEM images. The ImageJ software can

distinguishes the α phase and β phase which have different contrast in the SEM image. And the ImageJ software can adjust the α phase and β phase to white contrast and black contrast, respectively. Fig. 3.6 shows the images adjusted by the ImageJ software. Fig. 3.6(a) corresponds to the SEM image shown in Fig. 3.1(f) and Fig. 3.6(b) corresponds to the SEM image shown in Fig. 3.2 (f).

Fig. 3.7(a) shows the evolution of the average particle size of acicular α phase in the ST samples with changing the aging temperature or aging time. The tendency is that the particle size increases with increasing the aging time. For example, the length of the acicular α phase increases from 2.88 ± 1.11 μm to 3.16 ± 1.07 μm and the thickness of the acicular α phase increases from 0.18 ± 0.03 μm to 0.37 ± 0.09 μm after aging at 650 °C from 1.2 ks to 360 ks. The particle size also increases with increasing the aging temperature. For example, after aging from 550 °C to 750 °C for 14.4 ks, the particle size of the acicular α phase increases from 1.22 ± 0.82 μm in length and 0.07 ± 0.04 μm in thickness to 3.94 ± 1.88 μm in length and 0.42 ± 0.13 μm in thickness.

Fig. 3.7 (b) shows the evolution of the average particle size of equiaxed α phase in the HPT samples with changing the aging temperature or aging time. There is a similar tendency with the ST samples that the particle size increases with increasing the aging time or aging temperature. The particle size of the equiaxed α phase increases from 0.15 ± 0.05 μm to 0.73 ± 0.30 μm after aging at 650 °C from 0.3 ks to 360 ks. And the particle size of the equiaxed α phase increases from 0.17 ± 0.04 μm to 0.78 ± 0.26 μm after aging from 550 °C to 750 °C for 14.4 ks. It can be seen from the diagrams that the equiaxed α phase in the HPT samples is much finer than the acicular α phase in the ST samples. The particle size of the equiaxed α phase is much smaller than the length of the acicular α phase, but similar to or a little larger than the thickness of the acicular α phase.

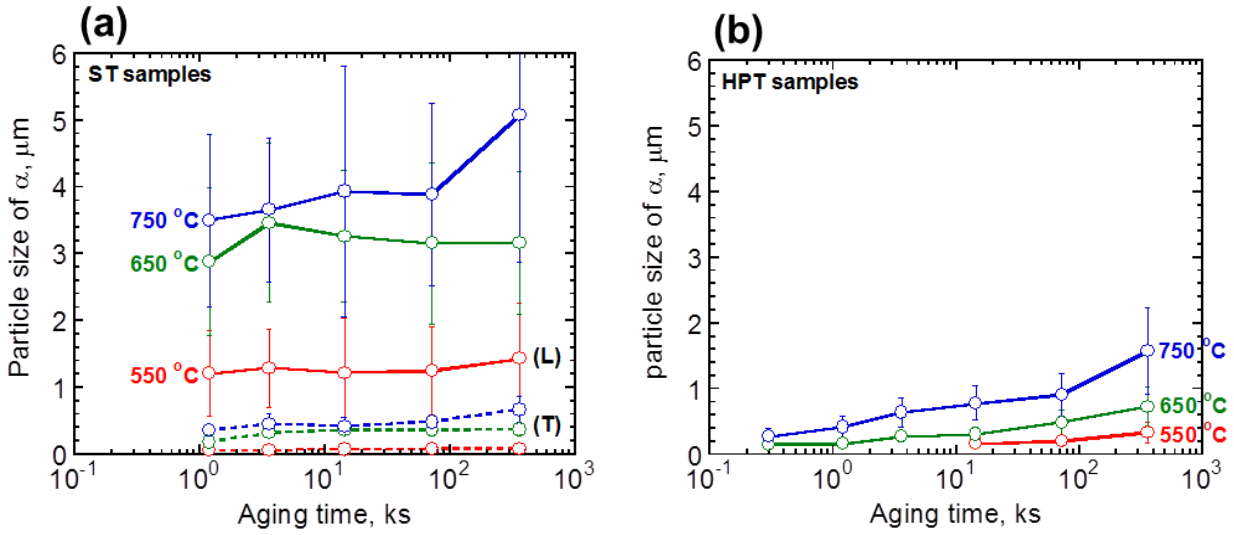

Fig. 3.7 Evolution of the average particle size of α phase with changing the aging time or aging temperature. (a) ST samples, and (b) HPT samples. The length (L) and the thickness (T) of the acicular α phase are respectively shown by the solid lines and dotted lines.

Fig. 3.8(a) shows the evolution of the volume fraction of acicular α phase in the ST samples with changing the aging time or aging temperature. In general, the volume fraction of α phase increases with increasing the aging time. Take the ST samples aged at 650 °C for example, the volume fraction of α phase increases rapidly from 3.1% to 44.7 ± 2.1% after aging from 0.3 ks to 1.2 ks. But continuous aging leads to a slow increase in the volume fraction of α phase. The volume fraction of α phase after aging for 360 ks is 48.4 ± 0.2%. For the ST samples aged at 750 °C, the volume fraction of α phase increases from 0 to 34.94 ± 0.80% after aging from 0.3 ks to 72 ks. Then the volume fraction of α phase shows a little decrease after aging for 360 ks, with a value of 31.37 ± 0.66%. With increasing the aging temperature, there is a decrease in the volume fraction of α phase. For example, the volume fraction decreases from 53.79 ± 2.02% to 30.70 ± 0.56% after aging from 550 °C to 750 °C for 14.4 ks.

Fig. 3.8(b) shows the evolution of the volume fraction of equiaxed α phase in the HPT samples with changing the aging time or aging temperature. A high volume fraction of α phase is obtained after aging for 0.3 ks. For example, the volume fraction of α phase is 43.2 ± 0.8% after aging at 650 °C for 0.3 ks. Continuous aging to 360 ks leads to a slow increase in the volume fraction, with a value of 46.2 ± 0.2%. This suggests that the growth of the equiaxed α phase progresses at the expense of the smaller equiaxed α phase. Similar to the ST samples, the volume fraction of α phase also decreases with increasing the aging temperature. The volume fraction decreases from 52.28 ± 0.14% to 30.15 ± 0.33% after aging from 550 °C to 750 °C for 14.4 ks.

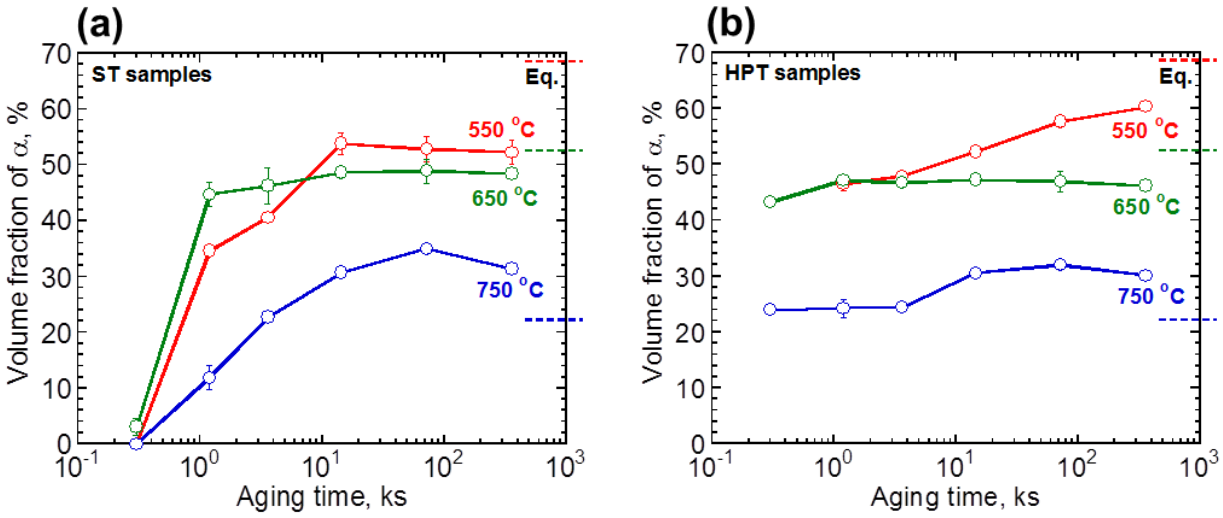

Fig. 3.8 Evolution of the volume fraction of α phase with changing the aging time or aging temperature. (a) ST samples, and (b) HPT samples. The dotted lines show the calculated equilibrium volume fractions of α phase in the Ti-5553 alloy aged at different temperatures.

The results shown by Fig. 3.8 also show that the ST samples and the HPT samples have the almost similar volume fraction of α phase after aging at the same conditions, except aging for 0.3 ks. Thermodynamic calculations by Pandat software predicted the equilibrium volume fraction of α phase in the Ti-5553 alloy aged at different temperatures, as indicated by the dotted lines in Fig. 3.8(a) and (b). The

equilibrium volume fraction of α phase is respectively 68.2%, 52.6% and 22.2% after aging at 550 ºC, 650 ºC and 750 ºC. Aged at 550 ºC and 650 ºC, the observed volume fraction of α phase is lower than the equilibrium values. But the observed volume fraction of α phase is higher than the equilibrium values after aging at 750 ºC.

3.3.1.2 TEM analysis

Further investigations on the formation of the equiaxed α phase in the HPT samples were carried out by TEM analysis. Fig. 3.9 depicts the precipitation of the equiaxed α phase after aging at low temperature 450 ºC for 14.4 ks. The bright-field (BF) image in Fig. 3.9(a) shows an ultrafine duplex microstructure composed of α and β phases. Ultrafine equiaxed α phase with the particle size less than 50 nm disperses in the β matrix, as shown by the dark-field (DF) image in Fig. 3.9(b). The TEM microstructures show that both the α phase and β phase are not well-defined and cannot exhibit clear grain boundaries. Fig. 3.9(c) shows the selected area electron diffraction (SAED) pattern. The SAED pattern indicates that the grains both the α phase and β phase have high-angle misorientations. The weak ω reflections in the SAED pattern reveal the precipitation of isothermal ω phase at this low aging temperature.

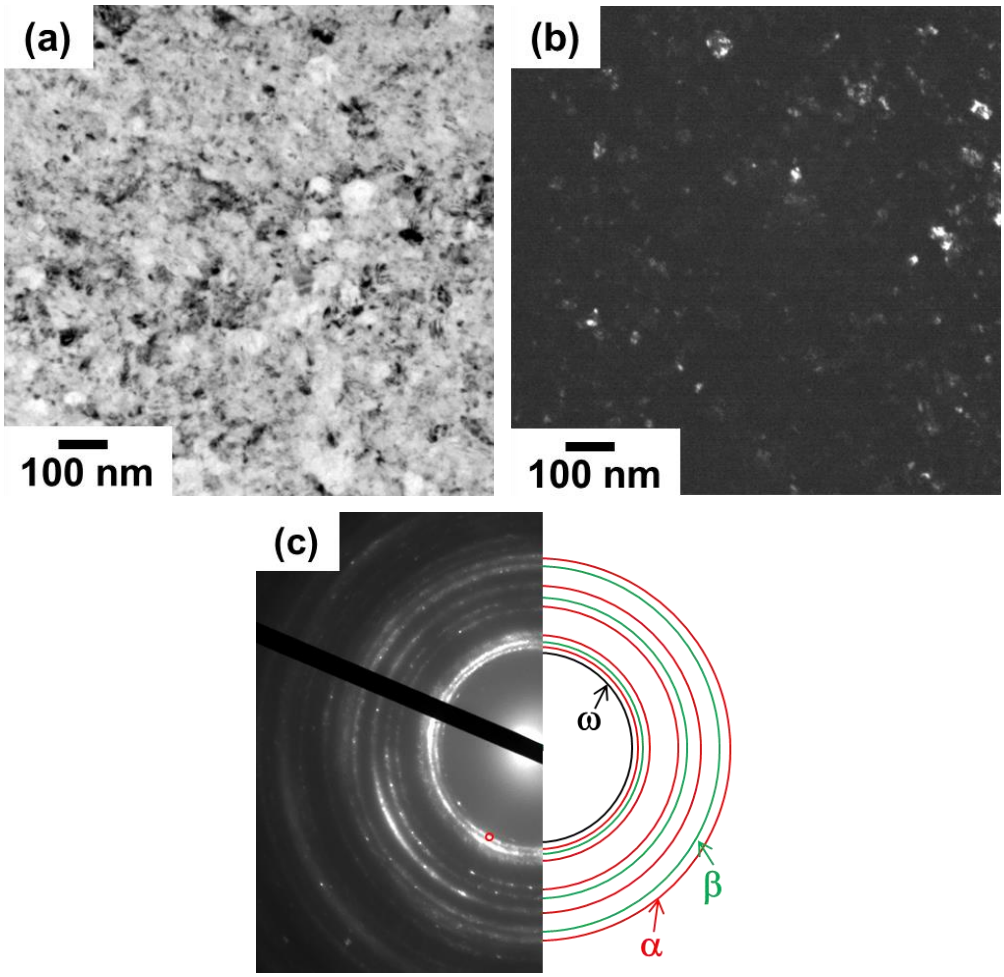

Fig 3.9 TEM micrographs of the HPT sample aged at 450 ºC for 14.4 ks. (a) BF image, (b) DF image from α(100) as indicated by the red circle in (c), and (c) corresponding SAED pattern.

Fig. 3.10 shows the formation of the equiaxed α phase aged at 550 ºC for 14.4 ks. Aging at 550 ºC leads to much coarser and well-defined α and β phases, as shown in Fig. 3.10(a) and (b). As shown by the SAED pattern in Fig.3.10(c), no ω reflections can be detected.

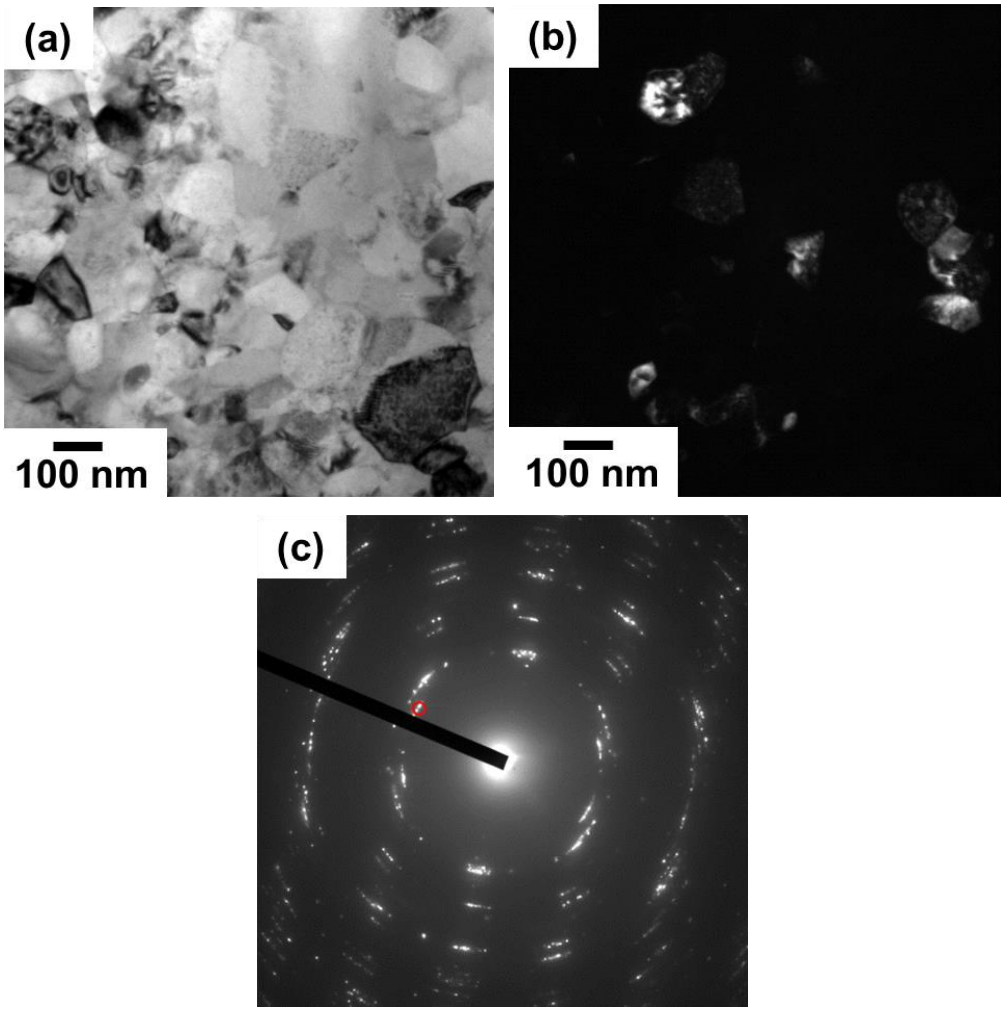

Fig 3.10 TEM micrographs of the HPT sample aged at 550 ºC for 14.4 ks. (a) BF image, (b) DF image from α(100) as indicated by the red circle in (c), and (c) corresponding SAED pattern.

The TEM micrographs on the precipitation of the equiaxed α phase after aging at 650 ºC and 750 ºC for 14.4 ks are respectively shown in Fig. 3.11 and Fig. 3.12. It is clearly that the equiaxed α phase becomes coarser with increasing the aging temperature. The interfaces between the α phase and β phase are sharp with no significant sign of stress between the two adjacent phases. Fig. 3.11(c) and (d) show the SAED pattern and its indexed diagram, respectively. The reflection from α phase is superimposed on $[1\bar{1}0]$ β diffraction pattern, which confirm the formed equiaxed α phase has the Burgers orientation relationship with the β phase. The same reflections of α phase can also be obtained aged at 750 ºC, as shown in Fig. 3.12(c).

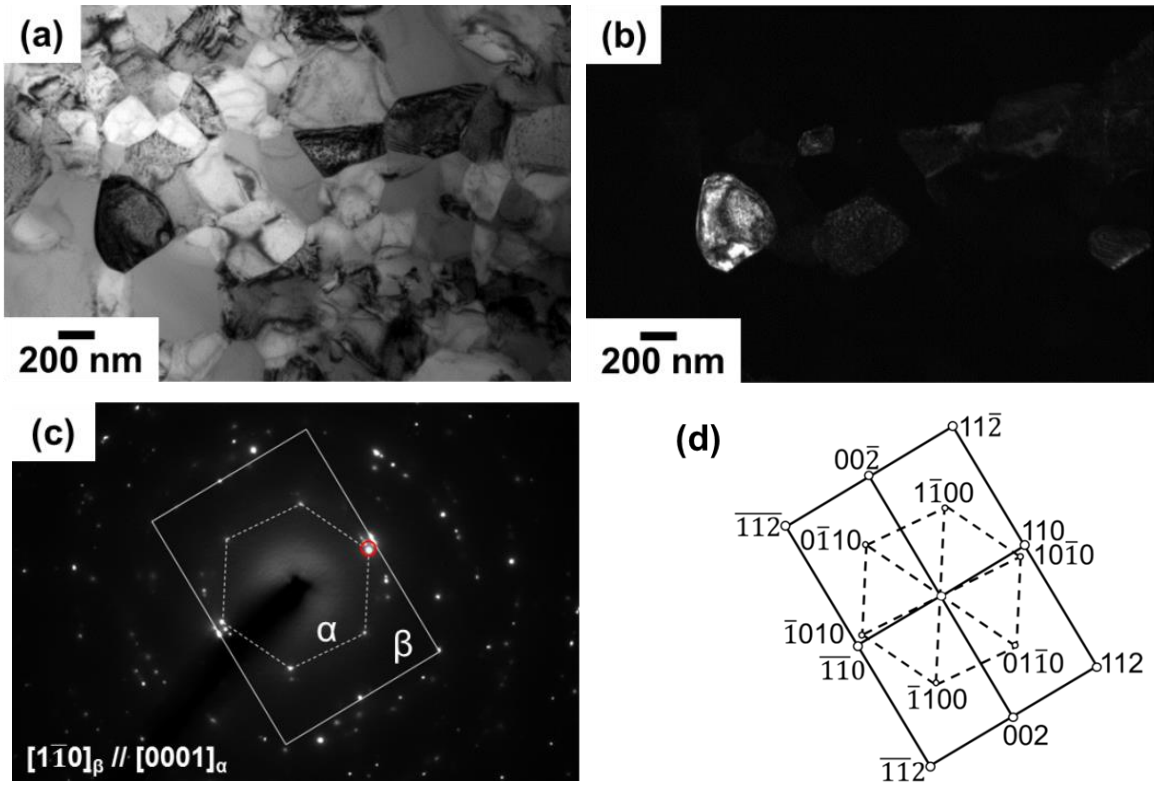

Fig. 3.11 TEM micrographs of the HPT sample aged at 650 ºC for 14.4 ks. (a) BF image, (b) DF image from the α reflection as indicated by the red circle in (c), (c) corresponding SAED pattern, and (d) schematic of the SAED.

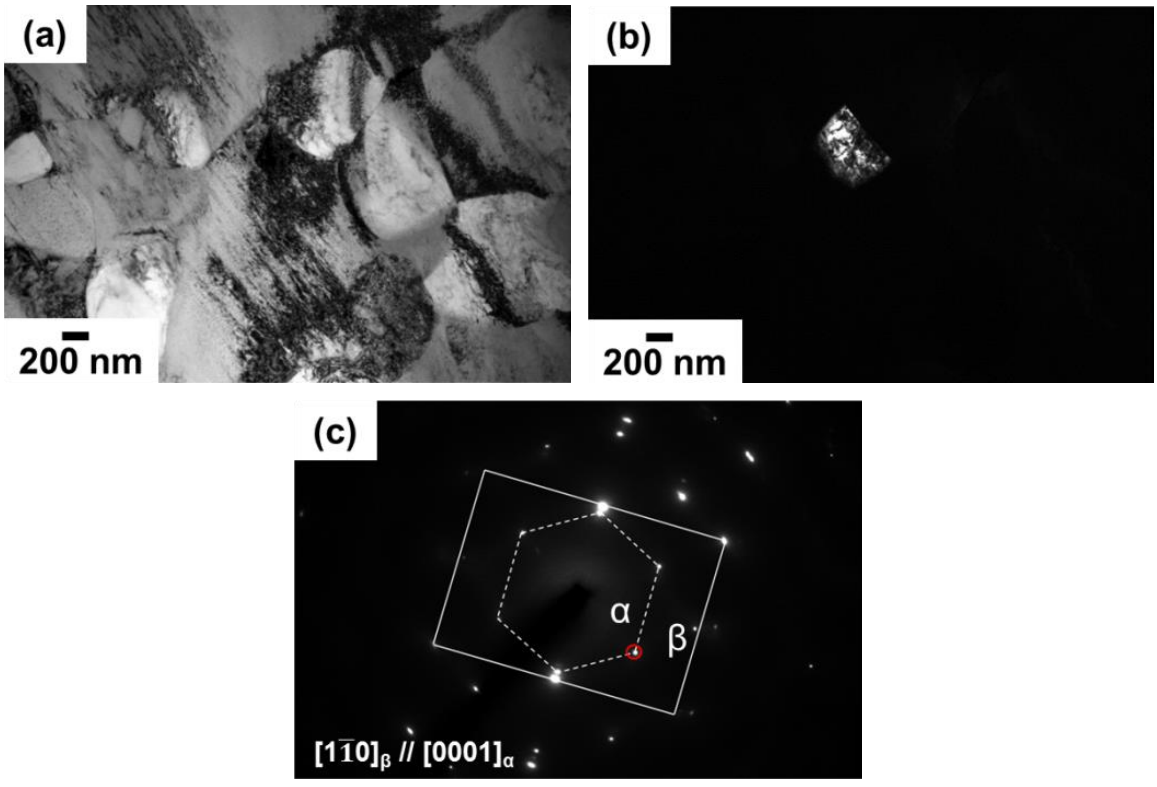

Fig. 3.12 TEM micrographs of the HPT sample aged at 750 ºC for 14.4 ks. (a) BF image, (b) DF image from the α reflection as indicated by the red circle in (c), and (c) corresponding SAED pattern.

3.3.2 Composition analysis of α phase

The growth of α phase is a diffusion controlled process, requiring partitioning of alloying elements between α and β phases. To confirm the growth process of α phase, the chemical composition of α phase was measured by EPMA. The composition of α phase after aging at 650 ºC and 750 ºC for different time is respectively shown in Fig. 3.13(a) and (b). The partitioning of alloying elements between α phase and β phase occurs during aging. Al enriches in α phase, while Mo, V and Cr are rejected from α phase. A higher content of Al and a lower content of Mo, V and Cr in the α phase can be obtained after aging for a longer time, which is consistent with the growth of α phase. The chemical composition of the equiaxed α phase formed in the HPT samples is found to be different from that of the acicular α phase formed in the ST samples. The chemical composition is Ti-5.37Al-3.92Mo-4.37V-2.88Cr (mass%) in the equiaxed α phase and Ti-5.42Al-3.55Mo-3.83V-2.47Cr (mass%) in the acicular α phase after aging at 650 ºC for 3.6 ks. Meanwhile, the chemical composition is Ti-5.94Al-3.01Mo-3.45V-2.03Cr in the equiaxed α phase and Ti-6.28Al-1.99Mo-2.63V-1.33Cr (mass%) in the acicular α phase after aging at 750 ºC for 3.6 ks. The equiaxed α phase contains a similar content of Al but higher content of Mo, V and Cr than the acicular α phase. The difference in the composition between the equiaxed α phase and the acicular α phase is much larger when aging at 750 ºC. After aging at 650 ºC for 360 ks, the chemical composition is Ti-6.20Al-1.72Mo-2.45V-1.12Cr (mass%) in the equiaxed α phase and Ti-5.93Al-2.55Mo-3.03V-1.69Cr (mass%) in the acicular α phase. And after aging at 750 ºC for 360 ks, the chemical composition is Ti-6.88Al-0.64Mo-1.84V-0.56Cr in the equiaxed α phase and Ti-6.63Al-0.92Mo-2.02V-0.7Cr in the acicular α phase. The equiaxed α phase contains a little higher content of Al but slightly lower contents of Mo, V and Cr compared with the acicular α phase. However, considering the fact that the minimum obtainable precision from EPMA is 0.5mass%, some of these compositional differences between equiaxed and acicular α phases are within the error range. In addition, the α phase formed at 750 ºC has a higher content of Al and a lower content of Mo, V and Cr compared with the α phase formed at 650 ºC, implying a higher diffusion rate of alloying elements at higher temperature.

The calculated equilibrium chemical composition of α phase by Pandat software is Ti-5.97Al-0.58Mo-1.42V-0.45Cr at 650 ºC and Ti-6.36Al-0.51Mo-1.37V-0.41Cr at 750 ºC. It shows a similar distribution tendency of alloying elements in α phase with the results in the present research. But the measured content of Al aged for 360 ks is similar with or higher than the equilibrium content of Al, while the measured content of Mo, V and Cr is higher than the equilibrium content of Mo, V and Cr. It seems like that much longer aging time is needed for the Mo, V and Cr achieve the equilibrium content in both the acicular and equiaxed α phase.

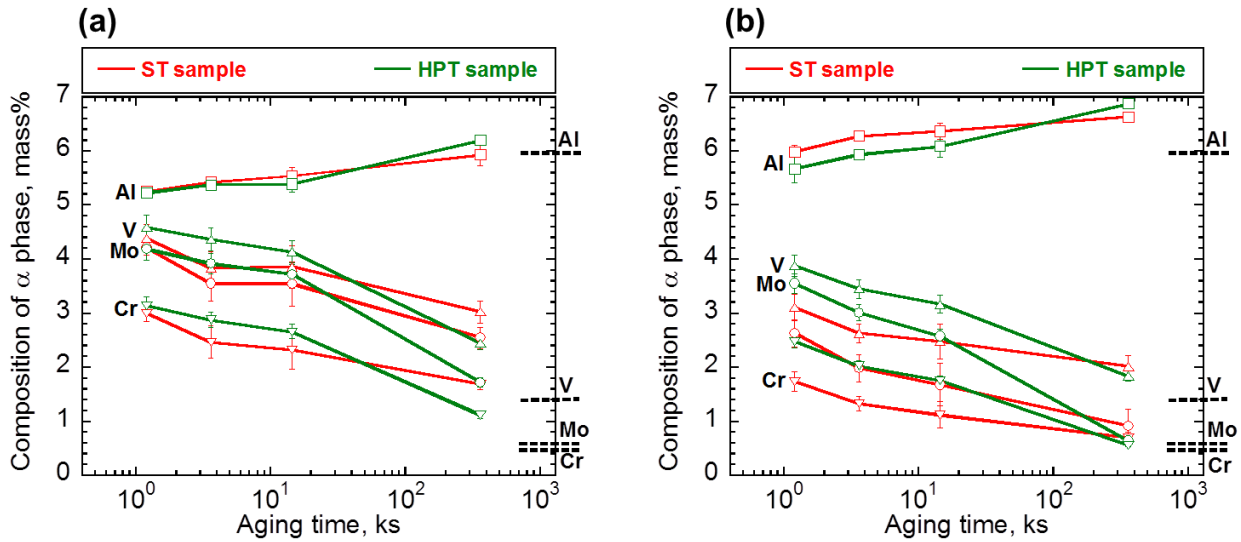

Fig. 3.13 Evolution of the chemical composition of α phase in the ST samples and HPT samples with changing the aging temperature or aging time. (a) 650 ºC, and (b) 750 ºC. The black dotted lines show the equilibrium composition of α phase calculated by Pandat software.

3.3.3 Orientation relationship between α and β phases

The TEM analysis shown in Fig.3.11 and Fig. 3.12 show that Burgers orientation relationship is maintained between the equiaxed α phase and β phase in HPT samples. However, only very limited areas can be observed by TEM, and thus it is difficult to determine whether these observations are isolated cases or representative results for the equiaxed α phase in the HPT samples. Therefore, EBSD analysis was performed to clarify the orientation relationship between the equiaxed α phase and β phase.

As a comparison, let's firstly see the EBSD analysis on the ST samples. Fig. 3.14 shows the EBSD analysis on the ST samples aged at 750 ºC for 14.4 ks. Fig. 3.14(a) shows the inverse pole figure (IPF) map. The acicular a phases show different color based on their crystallographic orientation. Here it should be noted that, in the present research, the crystallographic orientation of the grains shown in the inverse pole figure (IPF) is represented based on a cylindrical coordinate (Thickness, radial, and Hoop directions) instead of the ordinary Cartesian coordinate (i.e., ND, TD, RD) for EBSD analysis. The EBSD observations were carried out on the cross-section of the disk sample, which can also be described as the observed plane is parallel to the hoop direction (normal to the thickness direction and the radial direction). The pole figures (PF) in Fig. 3.14(b) show the {011} poles of the β matrix together with the {0001} poles of all the α variants. The orientation distributions of the poles for the α phase are sharp and indicate the presence of all the 12 α variants. It is evident from these PFs that the acicular α phase exhibit Burgers orientation relationship with surrounding β matrix.

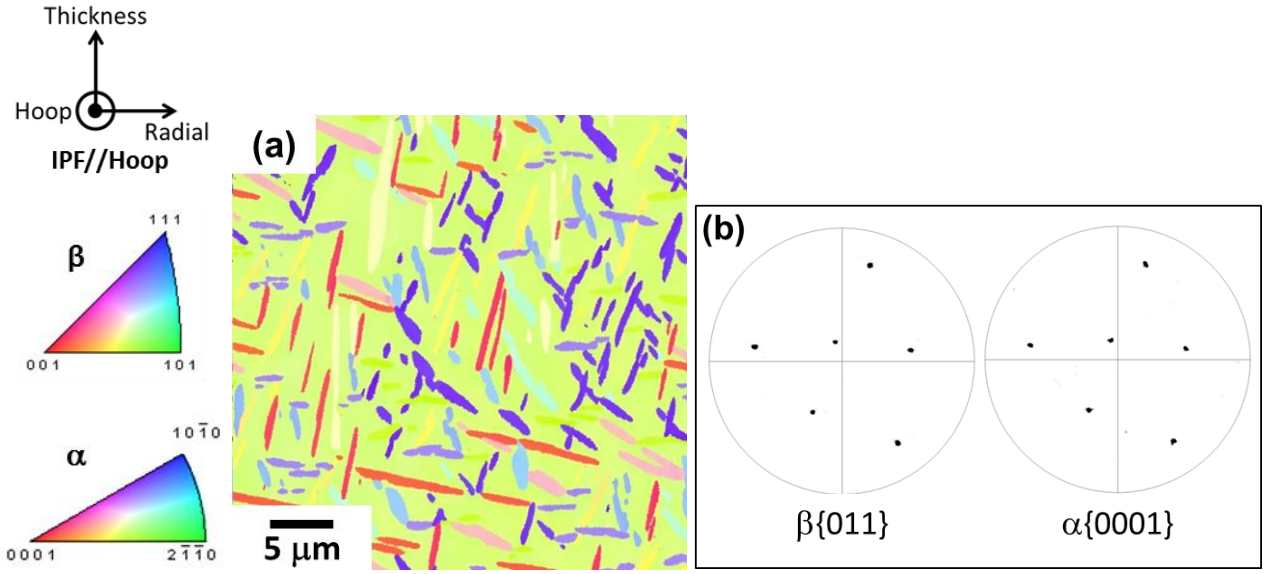

Fig. 3.14 (a) IPF map in the ST sample aged at 750 °C for 14.4 ks, and (b) the {011} PF from the β matrix and the {0001} PF from all the α variants.

The EBSD analysis on the HPT sample aged at 650 °C for 360 ks is shown in Fig. 3.15. Fig. 3.15(a) shows an overall IPF map of the α and β phases. PFs showing the {011} poles of all the β variants together with the {0001} poles of all the α variants are shown in Fig. 3.15(b). The orientation distributions of the poles for the α phase and β phase are scattered. The poles for the β phase can be mainly divided into two groups, as indicated by the red and green colors in the PF. Also, the poles for the α phase can be divided into two groups. From the {0001} poles of the α and the {011} poles of the β, it is evident that the α variants exhibit Burgers orientation relationship with the β variants.

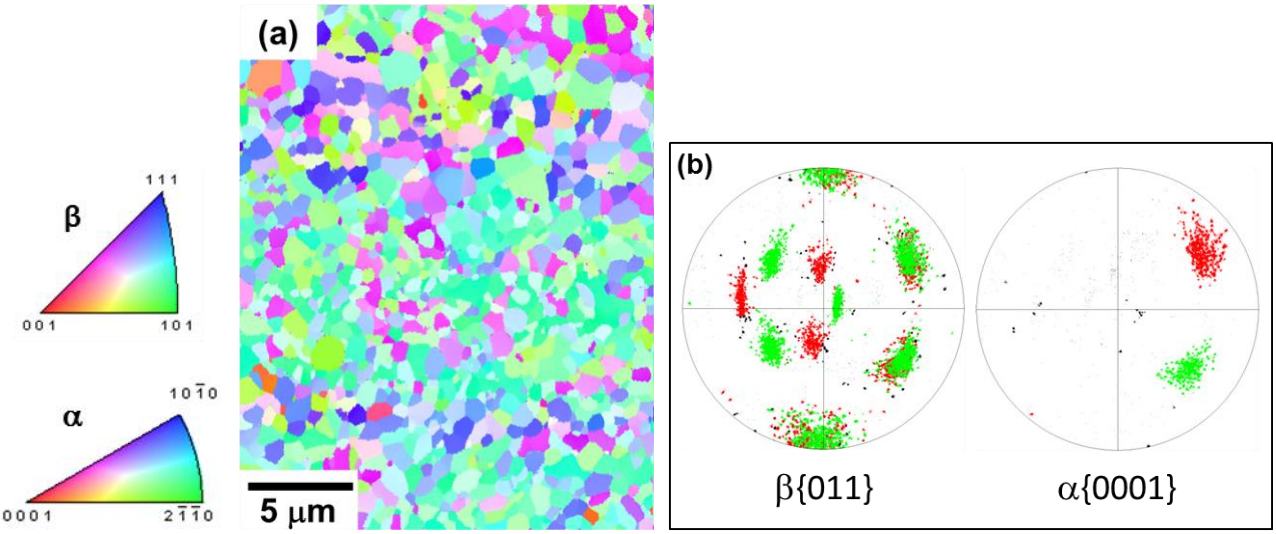

Fig. 3.15 (a) An overall IPF map of the α and β phases in the HPT sample aged at 650 °C for 360 ks, and (b) the {011} PF from the β phase and the {0001} PF from the α phase.

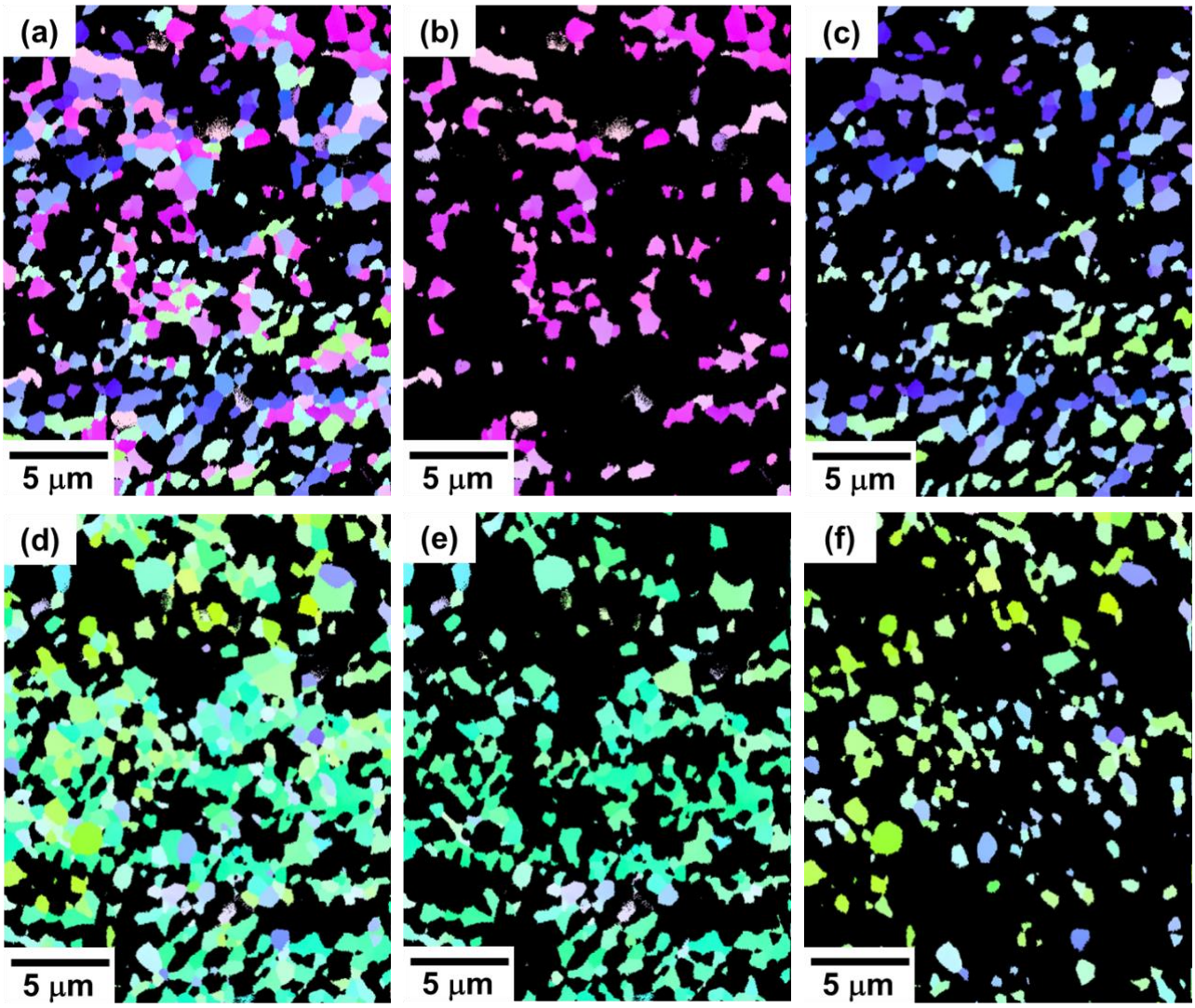

Fig. 3.16 IPF maps of Group A (correspond to the poles with red color in Fig. 3.15(b)): (a) α+β phase, (b) β phase, and (c) α phase; IPF maps of Group B (correspond to the poles with green color in Fig. 3.15(b)): (d) α+β phase, (e) β phase, and (f) α phase.

The group showing red color is named as Group A and the group showing green color is named as Group B. The IPF maps correspond to Group A and Group B are shown in Fig. 3.16. Fig. 3.16 (a), (b) and (c) respectively shows the IPF map of the α+β phase, β phase and α phase in Group A. And Fig. 3.16 (d), (e) and (f) respectively shows the IPF map of the α+β phase, β phase and α phase in Group B. It is very clearly that there are two groups of β phase depending on their crystallographic orientations. And these two groups of β phase distribute uniformly across the whole structure.

The IPF map of the HPT sample aged at 750 ^{o}C for 14.4 ks is shown in Fig. 3.17(a). The corresponding {011} PF of the β variants and the {0001} PF of the α variants are shown in Fig. 3.17(b). It is evident that the α variants exhibit Burgers orientation relationship with the β variants. Also, the poles for the β variants and α variants can be divided into two groups, as indicated by the red color (named as Group A) and green color (named as group B) in the PFs. The IPF maps correspond to Group A and Group B are shown in Fig.

3.18. Fig. 3.18(a), (b) and (c) respectively shows the IPF map of the α+β phase, β phase and α phase in Group A. And Fig. 3.18(d), (e) and (f) respectively shows the IPF map of the α+β phase, β phase and α phase in Group B. Different with the HPT sample aged at 650 °C for 360 ks, the microzones of the β phase with similar crystallographic orientation are formed after aging at 750 °C for 14.4 ks.. This suggests a recrystallization process of the β grains. It seems like that there is a competition relationship between the recovery of β phase and the precipitation of α phase during aging.

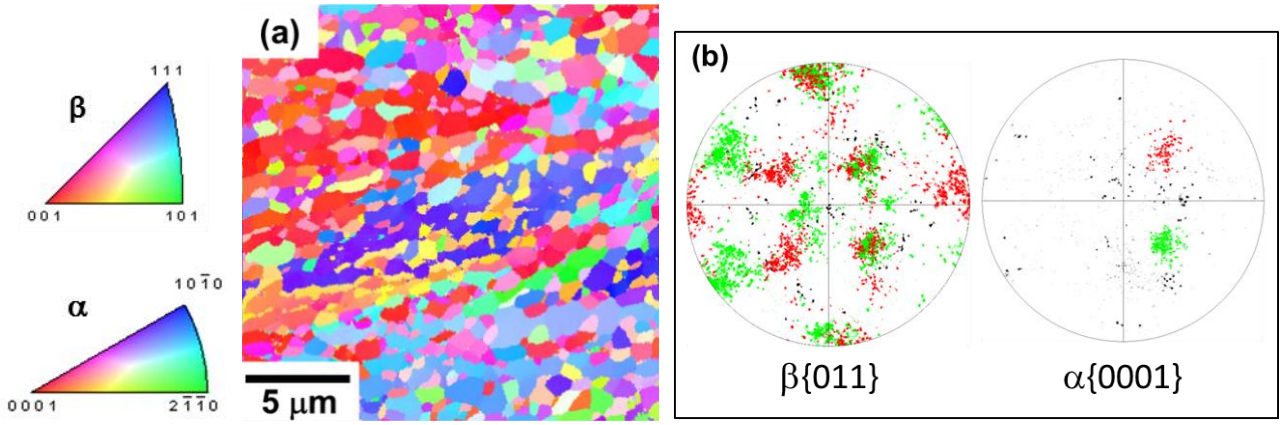

Fig. 3.17 (a) An overall IPF map of the α and β phases in the HPT sample aged at 750 °C for 14.4 ks, and (b) the {011} PF from the β phase and the {0001}PF from the α phase.

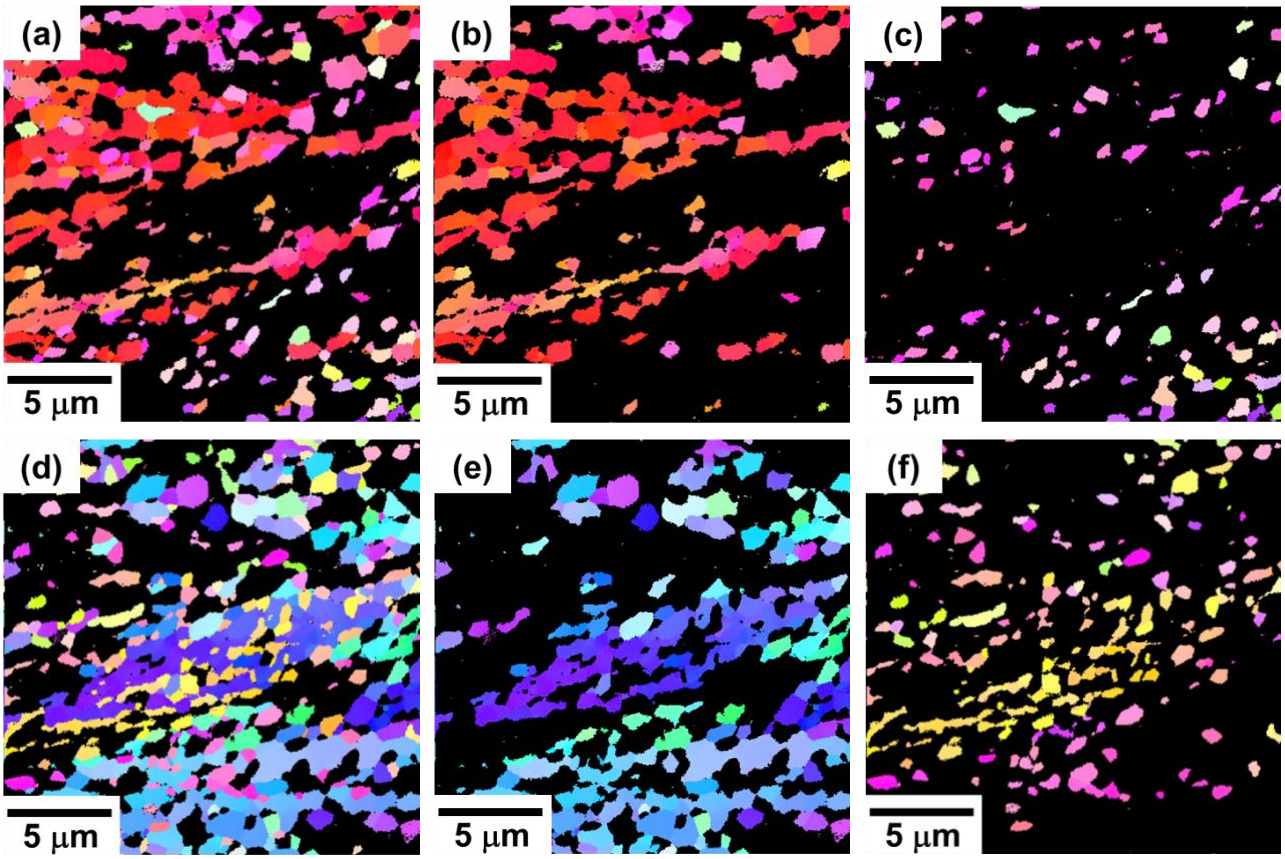

Fig. 3.18 IPF maps of Group A: (a) α+β phase, (b) β phase, and (c) α phase; IPF maps of Group B: (d) α+β phase, (e) β phase, and (f) α phase.

The volume fraction of α phase obtained from the SEM image analysis and the EBSD analysis are listed in Table 3.1. The two methods show very similar value for the volume fraction of α phase. This means that the method by the ImageJ software to calculate the volume fraction of a phase is preferably.

Table 3.1 Comparisons on the volume fraction of α phase obtained by the SEM image analysis and the EBSD analysis.

Ti-5553 alloy	Aging	Volume fraction of α phase, %	
		SEM image analysis	EBSD analysis
ST samples	750 °C – 14.4 ks	30.7	31.9
HPT samples	650 °C – 14.4 ks	47.28	51.35
	650 °C – 360 ks	46.20	47.43
	750 °C – 14.4 ks	30.15	29.1
	750 °C – 360 ks	30.06	29.6

3.3.4 Nanohardness of α and β phases

The nanohardness of the α phase and β phase were measured by nanoindentation. It is should be noted that the nanoindentation measurement was performed for some certain aging conditions because of the limitation of the particle size of α phase.

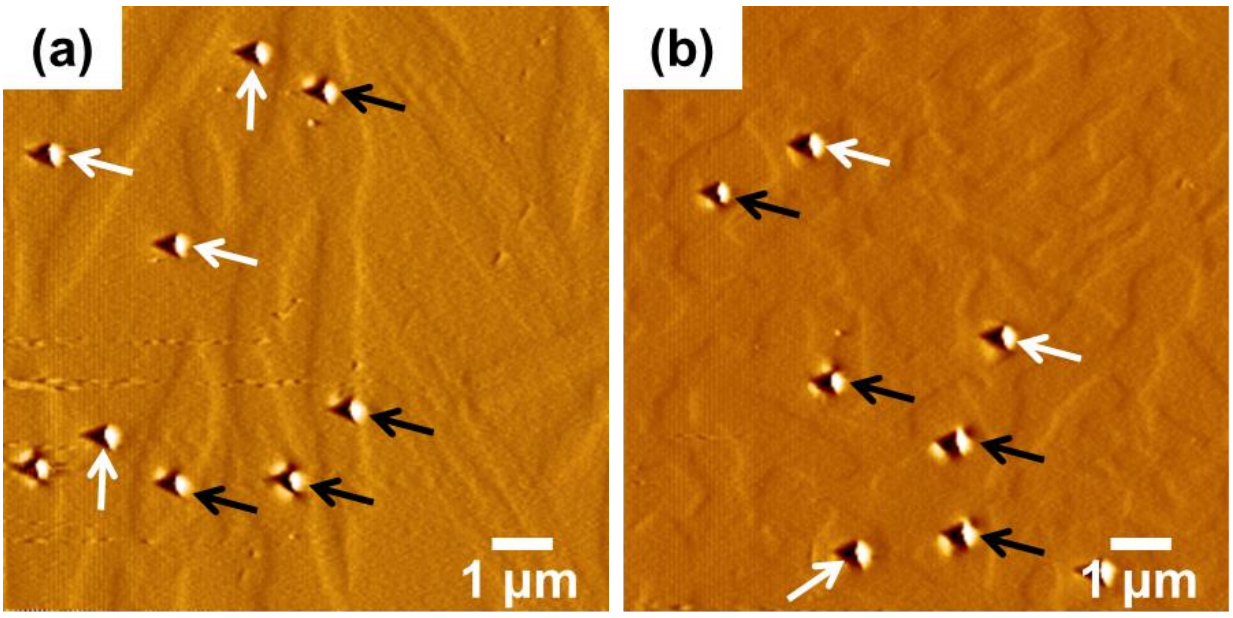

Fig. 3.19 Scanning probe microscopy images after nanoindentation measurements in the Ti-5553 alloy aged at 650 oC for 360 ks. (a) ST sample and (b) HPT sample.

Fig. 3.19 shows the corresponding in-situ scanning probe microscopy (SPM) images after the nanoindentation measurements in the ST sample and HPT sample aged at 650 ºC for 360 ks. The black and white arrows show indentations in α and β phases, respectively. The size of the indentations in α phase is comparable or smaller than the particle size of α phase.

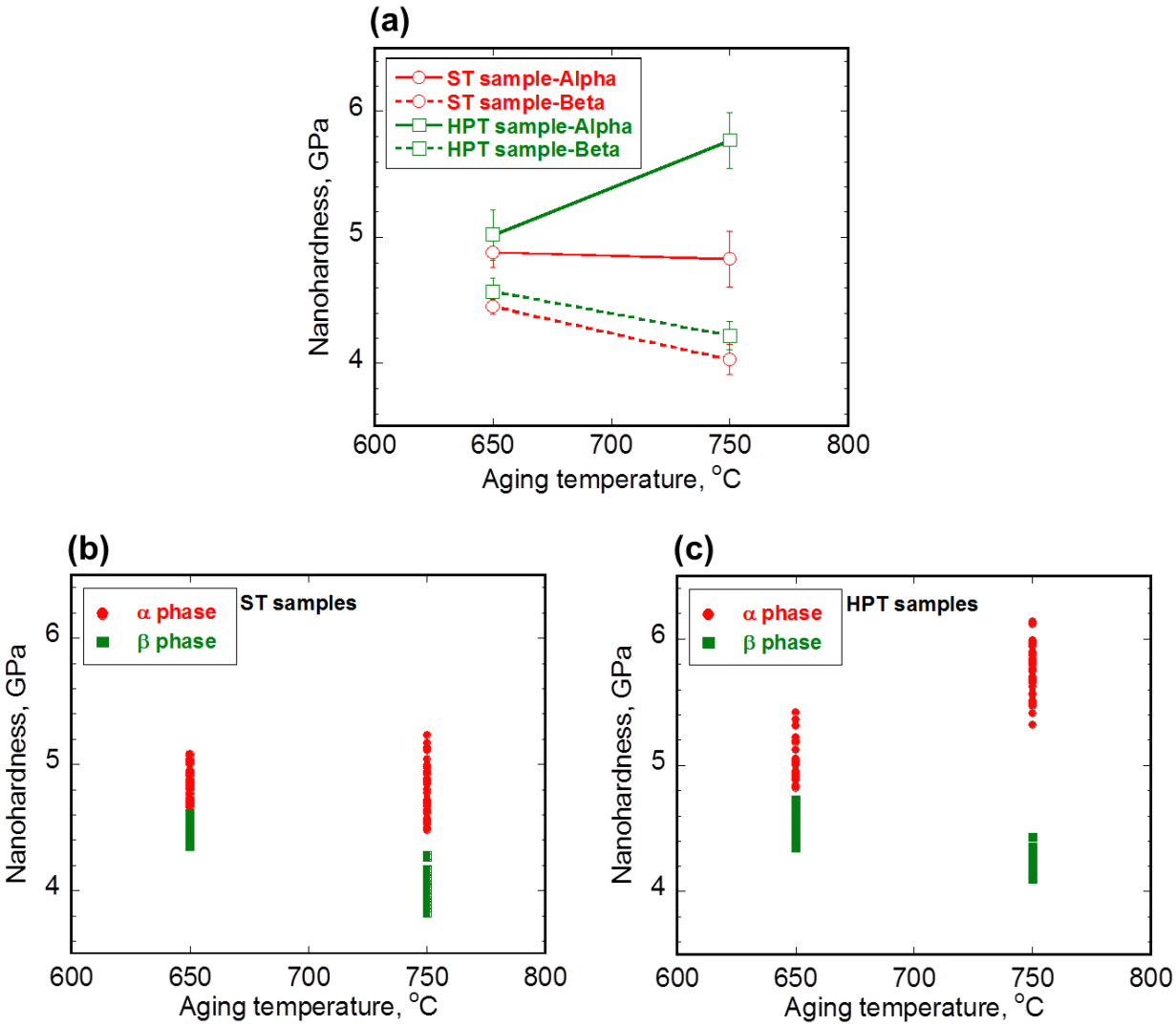

Fig. 3.20(a) Evolution of the average nanohardness of the α phase and β phase aged at 650 ºC and 750 ºC for 360 ks. All the measured nanohardness values of the α phase and β phase: (b) in the ST samples and (c) in the HPT samples.

Fig. 3.20(a) shows the average nanohardness of the α phase and β phase after aging at 650 ºC and 750 ºC for 360 ks. After aging at 650 ºC, the average nanohardness of the α phase and β phase in the ST sample are 4.88 ± 0.12 GPa and 4.45 ± 0.06 GPa, respectively. And the average nanohardness of the α phase and β phase in the HPT sample are 5.02 ± 0.20 GPa and 4.57 ± 0.11 GPa, respectively. The equiaxed α phase in the HPT sample is a little harder than the acicular α phase in the ST sample, and the β phase is also a little harder in the HPT sample than in the ST sample. After aging at 750 ºC, the average nanohardness of the α phase and β phase in the ST sample are 4.83 ± 0.22 GPa and 4.03 ± 0.12 GPa, respectively. And the average

nanohardness of the α phase and β phase in the HPT sample are 5.77 ± 0.22 GPa and 4.22 ± 0.11 GPa, respectively. The equiaxed α phase in the HPT sample is much harder than the acicular α phase in the ST sample, and the β phase in the HPT sample is also harder than that in the ST sample. The nanohardness of the acicular α phase shows no change by increasing the aging temperature from 650 °C to 750 °C, while the nanohardness of the equiaxed α phase shows a marked increase. The β phase in both the ST samples and the HPT samples shows a decrease by increasing the aging temperature from 650 °C to 750 °C. It also can be seen that the α phase is harder than the β phase. Fig. 3.20(b) shows all the measured nanohardness values of the α phase and β phase in the ST samples, while Fig. 3.20(c) shows those in the HPT sample. Even though in one sample, a wide range of nanohardness is obtained for the α or β phases.

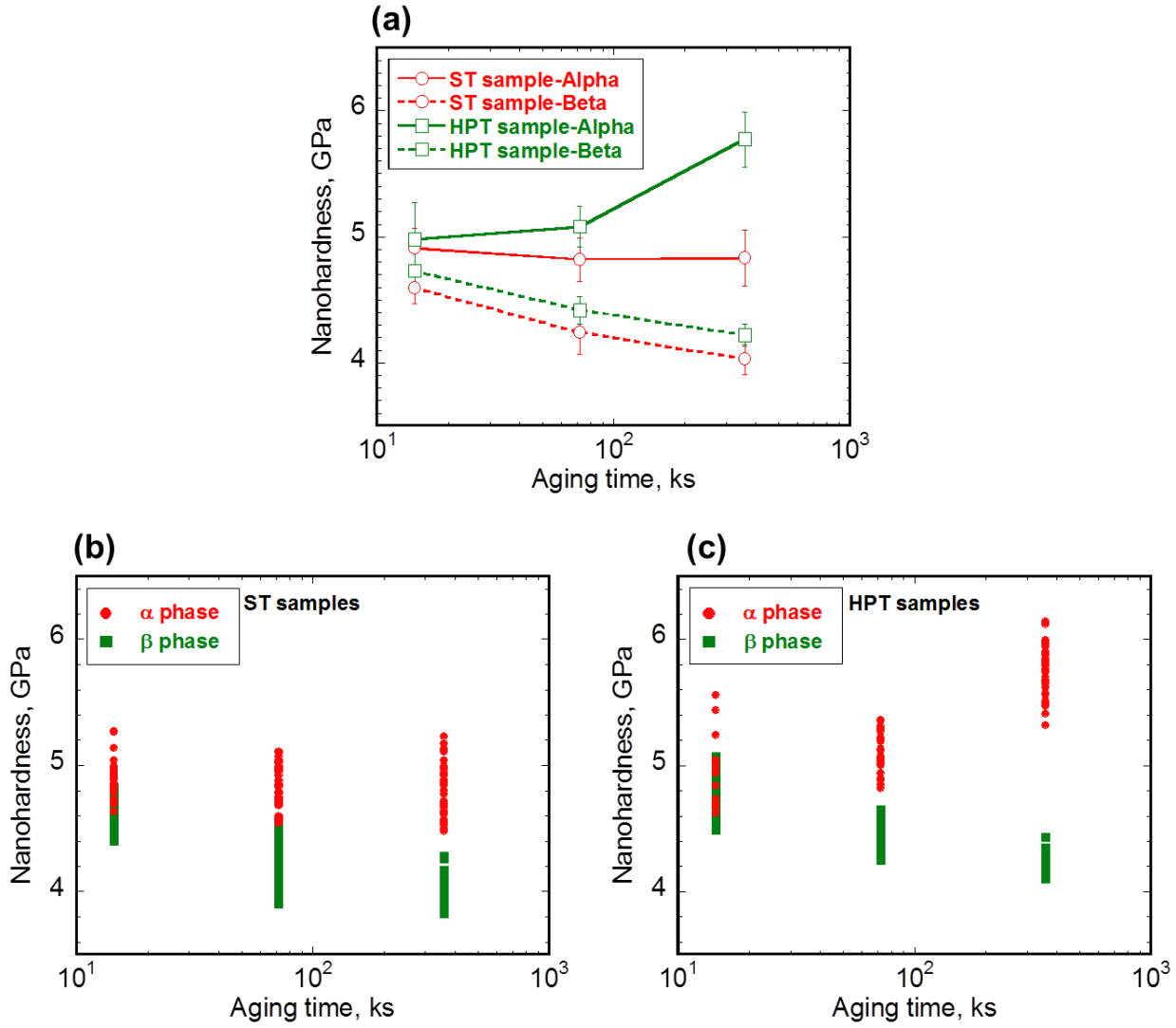

Fig. 3.21(a) Evolution of the average nanohardness of the α phase and β phase aged at 750 °C for different time. All the measured nanohardness values of the α phase and β phase: (b) in the ST samples and (c) in the HPT samples.

The evolution of the average nanohardness of the α phase and β phase aged at 750 °C for different time

is shown in Fig. 3.21(a). For the acicular α phase in the ST samples, the nanohardness keeps almost the same with increasing the aging time. But for the equiaxed α phase, the nanohardness increases with increasing the aging time. For the β phase in both the ST samples and HPT samples, the nanohardness decreases with increasing the aging time. Similar as mentioned above, the equiaxed α phase in the HPT sample is harder than the acicular α phase in the ST sample, and the β phase in the HPT sample is also harder than that in the ST sample. And the α phase is much harder than the β phase. All the measured nanohardness values of the α and β phases in the ST samples is shown in Fig. 3.21(b) and in the HPT samples are shown in Fig. 3.21 (c).

The results show that, for the Ti-5553 alloy, the α phase is harder than the β phase. The main reason for this is considered to be the enrichment of Al in the α phase. The enrichment of Al which has fairly large atomic size differences to Ti and also large solid solubility in the α phase causes substitutional solid solution hardening. It is reported that the enrichment of Al in the α phase can increase the c/a ratio by decreasing the a axis without causing much change in the c axis [7]. Min *et al*. reported the nanohardness of the α phase and β phase in three types of β-Ti alloys, including the Ti-15Mo alloy, Ti-15Mo-1Fe alloy and Ti-15Mo-3Al alloy (all the elements are in mass%). The results showed that the α phase is softer than the β phase in the Ti-15Mo alloy and Ti-15Mo-1Fe alloy, while the α phase is harder than the β phase in the Ti-15Mo-3Al alloy because of the enrichment of Al in the α phase [8].

The results in the present research also show that the nanohardness of the β phase decreases with increasing the aging temperature or aging time. This can be understood from the viewpoint of the depletion of Al from the β phase. However, there is a phenomenon cannot be answered just from the viewpoints of the compositions. As shown in Fig. 3.19 that the changes of the chemical composition in the equiaxed α phase and the acicular α phase are similar with increasing the aging temperature or time. But the nanohardness of the equiaxed α phase in the HPT samples increases with increasing the aging temperature or time, while the nanohardness of the acicular α phase keeps almost the same. Therefore, there are some other microstructural parameters can affect the nanohardness of the α phase, such as the crystal orientation, the morphology, the particle size or the content of β stabilizers. In the present research, how do these microstructural parameters affect the nanohardness of the α phase is not unclearly, but further studies are in progress.

3.3.5 Mechanical properties in ST and HPT samples

Fig. 3.22(a) shows the evolution of the microhardness in the ST samples with changing the aging temperature or aging time. In general, the tendency is that the microhardness increases firstly with increasing the aging time and then decreases with further aging. Take the samples aged at 650 °C for example, the peak hardness occurs after aging for 14.4 ks with a value of 352.1 ± 20 *H*v and the hardness decreases to 319.7 ± 8.4 *H*v after aging for 360 ks. But the hardness keeps the same after aging at 750 °C. The hardness is 294.7 ± 3.5 *H*v after aging for 0.3 ks and is 298.6 ± 7.5 *H*v after aging for 360 ks. In addition, the hardness is higher after aging at lower temperature. For example, the hardness is 410.2 ± 18.3 *H*v after aging at 550 °C for 14.4 ks and is 301.7 ± 10.4 *H*v after aging at 750 °C for 14.4 ks.

Fig. 3.22(b) shows the evolution of the microhardness in the HPT samples with changing the aging temperature or aging time. The peak hardness occurs much earlier in the HPT samples than in the ST samples. Aged at 650 ºC, the peak hardness with a value of 394.1 ± 7.6 *H*v occurs after aging for 1.2 ks. Further aging to 360 ks results in a decrease in the hardness to 313.5 ± 6.7 *H*v. Also, the increase in the aging temperature leads to a decrease in the hardness.

The results in Fig. 3.22 also show that the hardness is much higher in the HPT samples than in the ST samples when the aging time is ranging from 0.3 ks to 3.6 ks, and becomes to almost the same by ranging the aging time from 14.4 ks to 360 ks

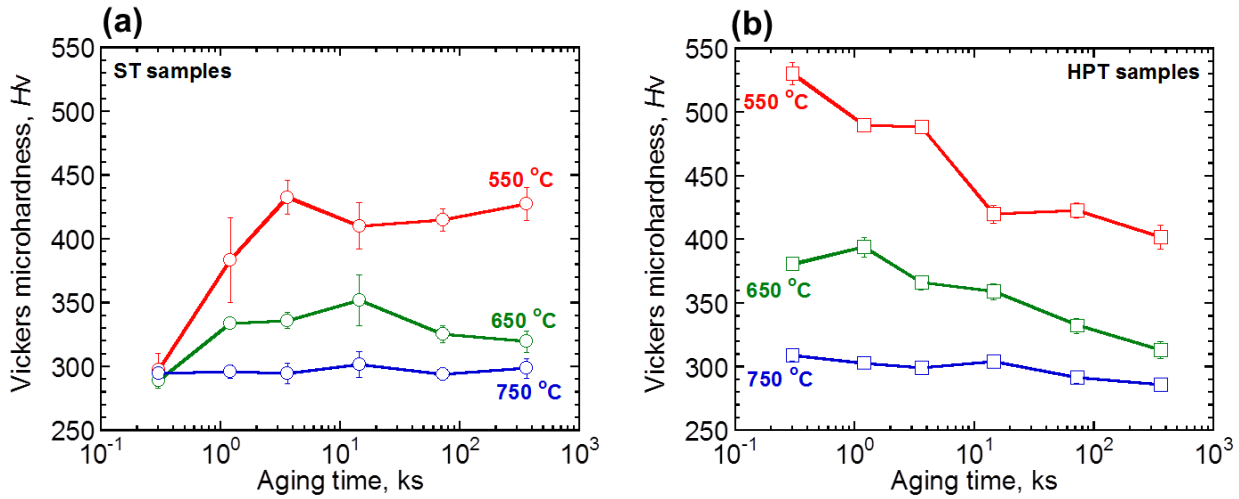

Fig. 3.22 Evolution of Vickers microhardness with changing the aging temperature or aging time. (a) ST samples, and (b) HPT samples.

The tensile properties of the ST samples and HPT samples aged at different temperatures for 14.4 ks were measured. Fig. 3.23(a) and (b) respectively shows the tensile stress-strain curves of the ST samples and HPT samples. The ultimate tensile strength (UTS) decreases with increasing the aging temperature, along with an increase in the elongation to failure (EL). A significant difference between the tensile stress-strain curves of the ST samples and HPT samples is that the HPT samples exhibit evident softening during the plastic deformation. Fig. 3.23(c) plots the average UTS and EL in the ST samples and HPT samples as a function of aging temperature. It shows the HPT samples have little higher UTS compared with the ST samples. And there is no difference in the EL between the ST samples and HPT samples.

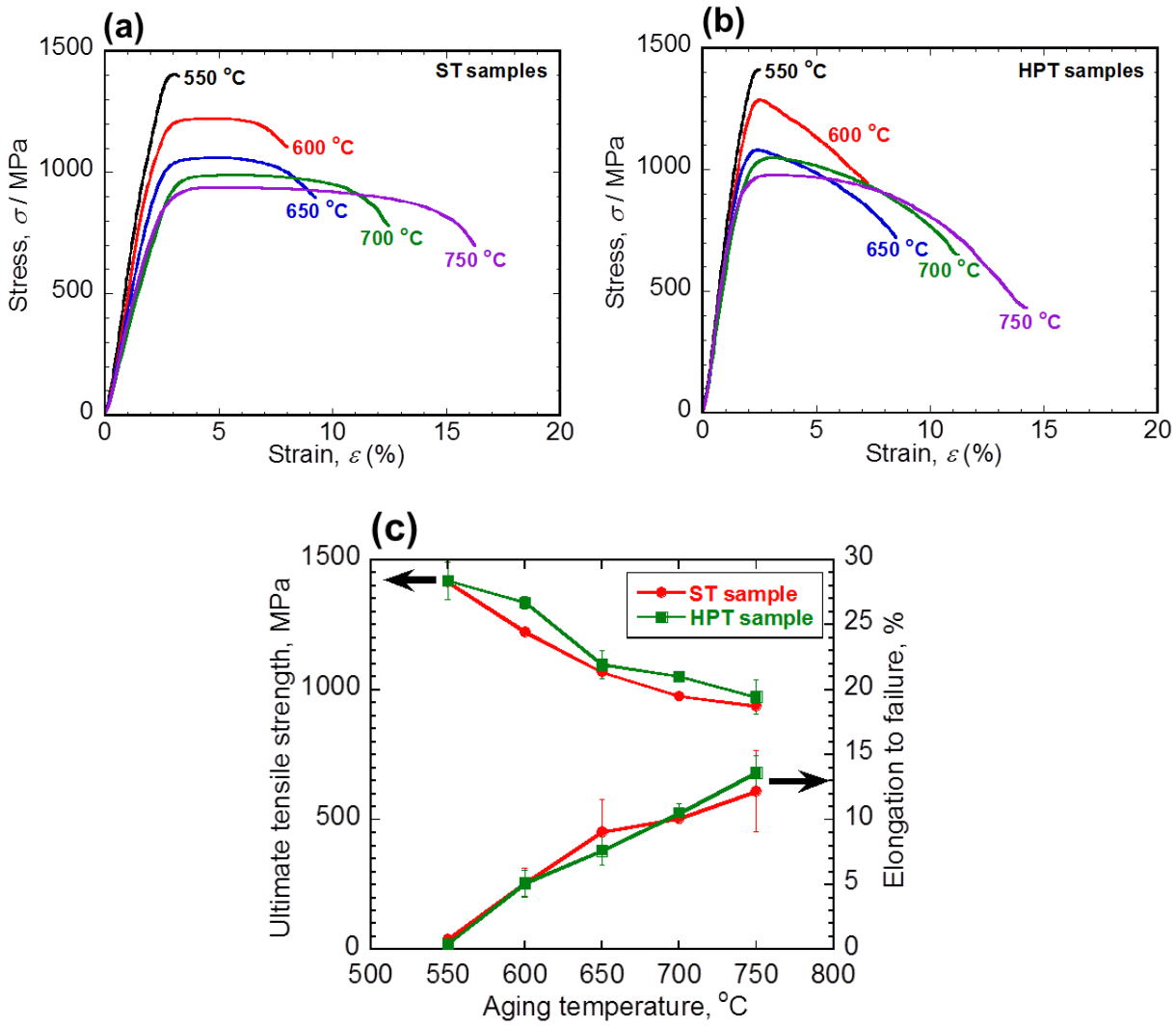

Fig. 3.23 Tensile stress-strain curves of the Ti-5553 alloy aged at different temperatures for 14.4 ks: (a) the ST samples and (b) the HPT samples, (c) the average ultimate tensile strength and elongation to failure of the ST samples and HPT samples.

3.4 Discussion

3.4.1 Formation of equiaxed α phase

This study confirmed that the HPT processing markedly changed the precipitation behavior of α phase in β-type Ti-5553 alloy during aging. The effects of the deformed ultrafine-grained microstructure on the formation of α phase are considered to originate mainly from the introduction of a high density of dislocations by HPT processing. As mentioned in Section 2.4, the HPT processing of 10 turns could produce a high density of dislocations which was 2.01 x 10^{15} m^{-2} inside the white etching layer.

Upon isothermal aging, two types of α phase, including the equiaxed α phase and acicular α phase, precipitate in the HPT samples. This is because of the different deformed microstructures. As shown in Section 2.3, deformation localized in the median section of the cross-section of the disk sample leading to the formation of white etching layer (WEL), which is the most dominant microstructure after HPT processing of

10 turns. Outside of the WEL, deformation localized in the form of shear bands (SB) where have a much higher defects density than the surroundings. The distribution of dislocations and other defects is homogeneous inside the WEL, but heterogeneous outside the WEL. Fig. 3.24(a) is a schematic diagram on the distribution of dislocations on the cross-section of the disk sample. The dislocation density is indicated by the grid density. In the central region of the cross-section where the WEL is formed, the dislocation density is the highest. In the surface region of the cross-section (outside the WEL), the dislocation density in the SBs is higher than the surrounding β matrix. Upon isothermal aging, the precipitation of α phase shows a selective nucleation and growth. The α phase first nucleates at the regions with a much higher density of dislocations, such as the SBs in the surface region and the WEL in the entire central region, as shown in Fig. 3.24(b). They grow into equiaxed α phase particles. In the regions with a lower density of dislocations, such as the β matrix surrounding the SBs in the surface region, the nucleation of α phase occurs late and grows into acicular α phase, as shown in Fig. 3.24(c).

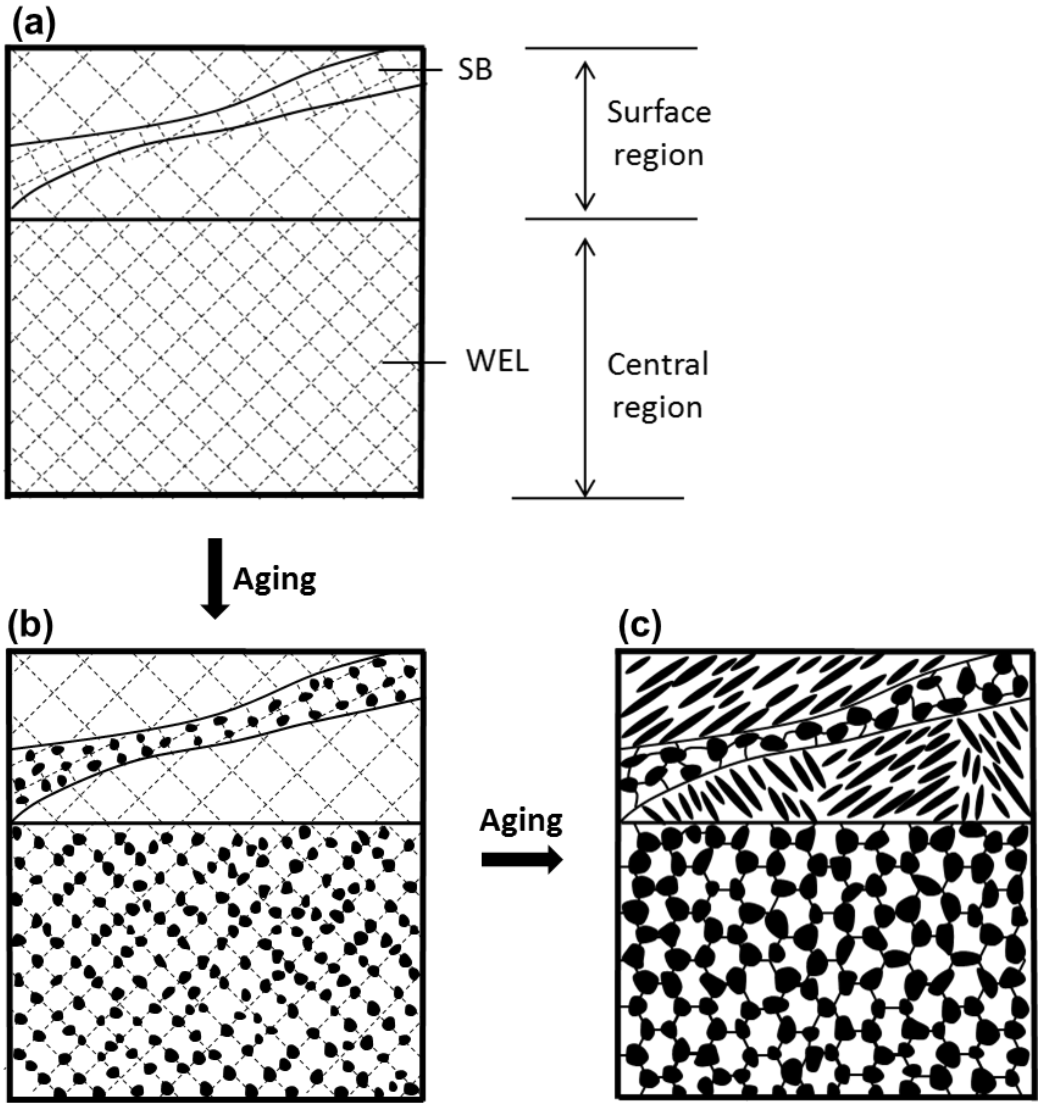

Fig, 3.24 (a) Schematic diagram of the microstructure on the cross-section of the disk sample after HPT processing. The grid density indicates the dislocation density. (b) and (c) Schematic diagram on the precipitation behavior of α phase upon aging.

The dislocation lines generally can act as preferential nucleation sites for α phase and fast paths for transporting atoms [9]. The HPT-induced high density of dislocations provides numerous nucleation sites and enhanced diffusivity of alloying elements, consequently the accelerating the nucleation of α phase. That's the reason why the formation of α phase is more rapid in the HPT samples than in the ST samples (or the formation of α phase is more rapid inside the WEL than outside the WEL).

Compared the particle size and composition between acicular α phase and equiaxed α phase, it shows that the growth of α phase in HPT samples is not accelerated very much. This is mainly due to the overlap of diffusion fields which is caused by the dense precipitation of equiaxed α phase. The influence of overlapping diffusion fields on the diffusion of Mo element is schematically exhibited in Fig. 3.25. As reported by Nag *et al*. [10] that the proximity of overlapping diffusion fields to adjacent α regions could lead to the pile-up of Mo at α/β interfaces. The content of Mo in β phase is higher than the equilibrium content at the α/β interfaces. The diffusion rate of alloying elements can be reduced, and consequently retarding the growth of α phase.

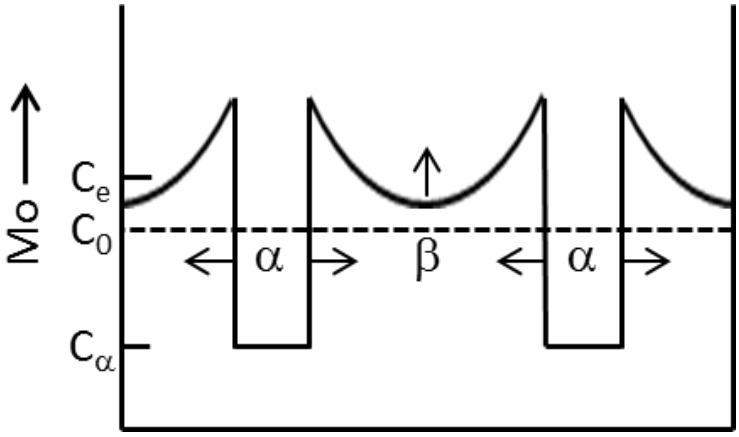

Fig.3.25 Schematic diagram on the influence of overlapping diffusion fields on the diffusion of Mo element between α and β phases.

For the shape of α phase, it is governed by the diffusion-controlled migration of α/β interfaces. In general, α nucleus is bounded by a combination of coherent or semicoherent facets and incoherent interfaces so as to minimize the total interfacial free energy [11]. The incoherent interfaces migrate much faster than the coherent or semicoherent interfaces, leading to the formation of an acicular shape, as the α phase formed in ST samples. But in HPT samples, the pile-up of Mo at α/β interfaces caused by overlapping diffusion fields limits the growth of α phase, especially the growth in long axis direction, promoting the formation of equiaxed morphology. In addition, EBSD analysis and TEM analysis in the present study show that the orientation relationship between equiaxed α phase and β phase is not random as inferred by Xu *et al*. [5], and Burgers orientation relationship is still maintained between equiaxed α phase and β phase .

3.4.2 Microstructure-mechanical properties relationship

This study showed that, for Ti-5553 alloy with a variety of microstructures, a wide range of microhardness, ultimate tensile strength and ductility could be achieved. Before the detailed discussion of the results, it appears to be useful to point out the complex nature of plastic deformation in such a two phase alloy. The aged Ti-5553 alloy consists of a β phase matrix and α phase precipitates. Both phases are ductile and can deform plastically. As mentioned in the introduction part, the mechanical properties strongly depend on the volume fraction, particle size, distribution and morphology of the of α phase precipitates. But it is very difficult to separate the individual contributions of each factor to the mechanical properties, because the α phase precipitates in all the aged samples contain numerous combinations of volume fraction, particle size and morphology. Therefore, the discussion will be limited to a more qualitative explanation on the microstructure-mechanical properties relationships.

The mechanical properties of Ti-5553 alloy have shown a very strong sensitivity to the changes in the volume fraction. Fig. 3.26(a) shows the relationship between the yield strength and the volume fraction of α phase. The yield strength was calculated by the empirical relationship $\sigma_y = Hv/3$. The tendency is that the yield strength increases with increasing the volume fraction of α phase. But it also shows that the yield strength keeps at a constant level when the volume fraction of α phase ranges from 0 to around 30 %. Fig. 3.26(b) shows the relationship between the elongation to failure and the volume fraction of α phase. There is a loss in the ductility by increasing the volume fraction of α phase.

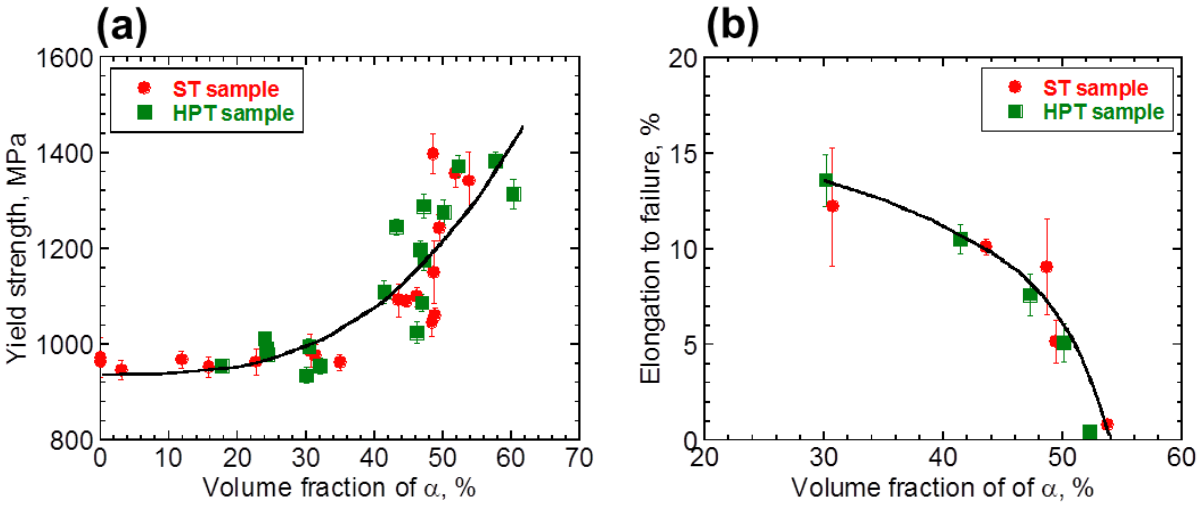

Fig. 3.26 Relationship between the mechanical properties and the volume fraction of α phase in the ST samples and HPT samples. (a) Yield strength, and (b) Elongation to failure.

The particle size of α phase is another important microstructural parameter that can affect the mechanical properties in metastable β-Ti alloys. Fig. 3.27(a) shows the relationship between the yield strength and the particle size of α phase. Fig. 3.27(b) shows the relationship between the elongation to failure and the particle size of α phase. For both the ST samples and HPT samples, the increase in the particle size of α phase leads to a decrease in the yield strength and an increase in the ductility.

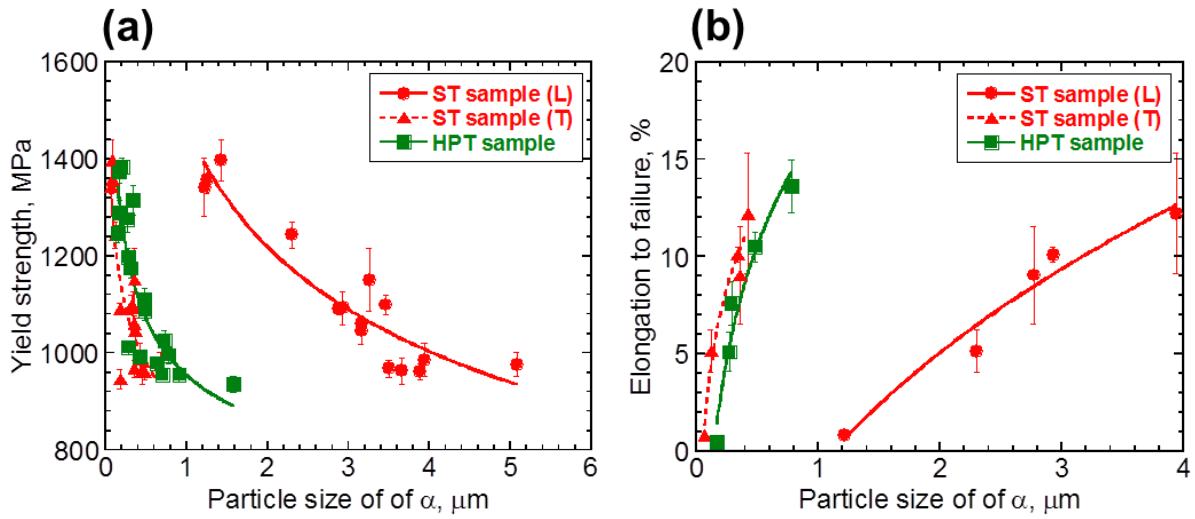

Fig. 3.27 Relationship between the mechanical properties and the particle size of α phase in the ST samples and HPT samples. (a) Yield strength, and (b) Elongation to failure.

A higher volume fraction and a finer particle size of α phase lead to a higher yield strength and a lower ductility in both the ST samples and HPT samples. This can be easily understood from the viewpoint of the precipitation/dispersion hardening mechanism. A higher volume fraction or a finer particle size of α phase at a certain volume fraction will lead to a smaller space between two α particles. The relationship between the yield strength and the interphase distance (d) is shown in Fig. 3.28. The liner relationship between the yield strength and $d^{-1/2}$ suggests that the strengthening by the precipitation of α phase follows Hall-Petch strengthening mechanism, which also implies the pile-up of dislocations at α/β interfaces during plastic deformation. Some previous studies by Jones *et al*. [12, 13] and Jackson *et al*. [14] have reported that the α phase can act as barriers, impeding the movement of dislocations strongly and leading to the pile-up of dislocations at α/β interfaces. However, it is should be noted that when the interphase distance is below 0.15 μm in the ST samples, the yield strength appears to keep almost no change with further decrease in the interphase distance. At very small interphase space, the array of dislocations may be limited and dislocation sources can hardly exist. This implies that dislocation pile-up cannot form and the Hall-petch relationship is no longer valid. The Hall-Petch coefficient for the ST samples, K_{ST}, was estimated to be 219 MPa(μm)$^{-1/2}$. And the Hall-Petch coefficient for the HPT samples, K_{HPT}, was estimated to be 246 MPa(μm)$^{-1/2}$. There is a slight difference in Hall-Petch coefficients between the ST samples and HPT samples.

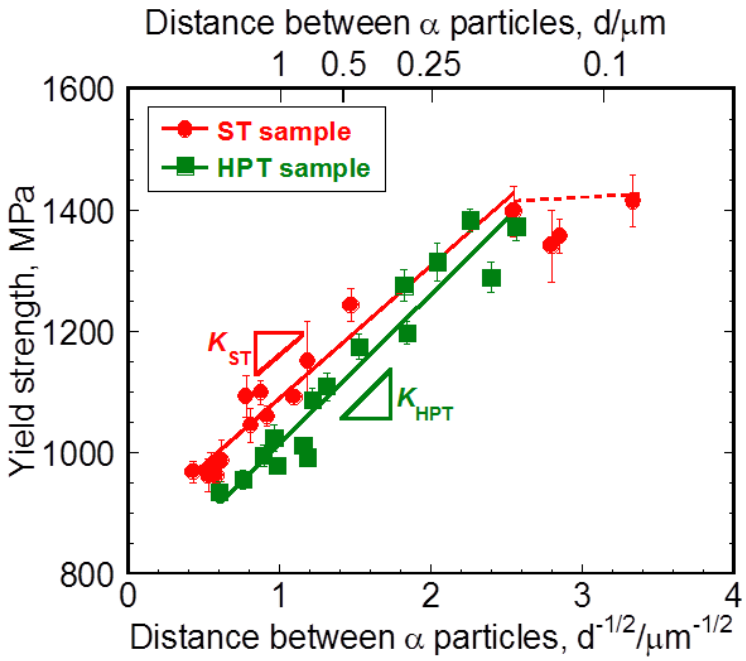

Fig. 3.28 Relationship between the yield strength and α interphase space in the ST samples and HPT samples.

3.5 Summary

The precipitation behavior of α phase in the high-pressured torsion (HPT) processed Ti-5Al-5Mo-5V-3Cr (mass%) alloy by isothermal aging was studied and compared with that in the solution treated (ST) samples. The effects of the α phase precipitates with different volume fraction, particle size and morphology on the mechanical properties were discussed. The results can be summarized as follows:

(1) Ultrafine equiaxed α phase precipitated in HPT samples, while coarse acicular α phase formed in the ST samples.

(2) The particle size of both the equiaxed α phase and acicular α phase increased by increasing the aging temperature or aging time. The particle size of the equiaxed α phase was much smaller than the length of the acicular α phase, but similar to or a little larger than the thickness of the acicular α phase.

(3) The volume fraction of both the equiaxed α phase and acicular α phase decreased with increasing the aging temperature or increased with increasing the aging time. The more rapid precipitation of the equiaxed α phase caused a much higher volume fraction in the HPT samples than in the ST samples at the early aging stage. But further aging for long time led to a similar volume fraction in the ST samples and HPT samples.

(4) The equiaxed α phase contained a lower content of α-stabilizer (Al) but a higher content of β-stabilizers (Mo, V and Cr) compared with the acicular a phase when aging for 1.2 ks to 14.4 ks. Aging for 360 ks led to a higher content of Al and a lower content of Mo, V and Cr in the equiaxed α phase than in the acicular α phase.

(5) The nucleation of α phase in HPT samples is more rapid than that in ST samples. This is due to the

HPT-induced high density of dislocations which can provide numerous nucleation sites and enhanced diffusivity. The dense precipitation of α phase in HPT samples causes overlapping diffusion fields which can retard the growth of α phase during long time aging, leading to ultrafine particle size with equiaxed morphology.

(6) TEM and EBSD analysis showed that Burgers orientation relationship was still maintained between the equiaxed α phase and surrounding β matrix. The β phase could be divided into two types based on their crystallographic orientations.

(7) For Ti-5553 alloy, the α phase was harder than the β phase because of the enrichment of Al in α phase. The nanohardness of β phase decreased with increasing the aging temperature or time. The nanohardness of equiaxed α phase increased with increasing the aging temperature or time, while the nanohardness of acicular α phase kept no change. The α and β phases in the HPT samples were respectively harder than these phases in the ST samples.

(8) For both the ST samples and HPT samples, the microhardness and ultimate tensile strength decreased with increasing the aging temperature, accompanied with an increase in the ductility. Aged at a certain temperature for different time, the peak hardness occurred much earlier in the HPT samples than in the ST sample. The microhardness was higher in the HPT samples than in the ST samples at the early aging stage, and then became almost the same after long time aging.

(9) The strengthening by the precipitation of α phase can be explained by Hall-Petch strengthening mechanism. A higher volume fraction or a finer particle size of α phase caused a smaller space between α particles, consequently leading to a higher strength and a lower ductility.

3.6 References

[1] J.C. Williams, B.S. Hickman, H.L. Marcus, The effect of omega phase on the mechanical properties of titanium alloys, Met. Trans. 2 (1971) 1913-1919.

[2] A.W. Bowen, Omega phase embrittlement in aged Ti-15Mo, Scripta mater. 5 (1971) 709-716.

[3] A.W. Bowen, On the strengthening of a metastable β-titanium alloy by ω- and α- precipitation, Titanium '80: Sceience and technology, (1980) 1317-1326.

[4] W. Xu, D.P. Edwards, X. Wu, M. Stoica, M. Calin, U. Kühn, J. Eckert and K. Xia, Promoing nano/ultrafine-duplex structure via accelerated α precipitation in a β-type titanium alloy severely deformed by high-pressure torsion, Scripta Mater. 68 (2013) 67-70.

[5] W. Xu, X. Wu, M. Stoica, M. Calin, U. Kuhn, J. Eckert, K. Xia, on the formation of an ultrafine-duplex structure facilitated by severe plastic deformation in a Ti-20Mo β-type titanium alloy, Acta Mater. 60 (2012) 5067-5078.

[6] W.C. Oliver, G.M. Pharr, An improved technique for determining hardness and elastic modulus using load and displacement sensing indentation experiments, Mater. Res. 7 (1992) 1564-1583.

[7] D.E. Gordon, J.W. Hagemeyer, Relationships of strength to composition and phase constitution for three aged beta titanium alloys, J. mater. Sci. 10 (1975) 1725-1731.

[8] X.H. Min, L. Zhang, K. Sekido, T. Ohmura, S. Emura, K. Tsuchiya, K. Tsuzaki, Strength evolution of α and β phases by nanoindentation in Ti-15Mo alloys with Fe and Al addition, Mater. Sci. Tech. 28 (2012) 342-347.

[9] M. Legros, G. Dehm, E. Arzt, T.J. Balk, Observation of giant diffusivity along dislocation cores, Science 319 (2008) 1646-1649.

[10] S. Nag, R. Banerjee, J.Y. Hwang, M. Harper, H.L. Fraser, Elemental [artitioning between α and β phases in the Ti-5Al-5Mo-5V-3Cr-0.5Fe (Ti-5553) alloy, Philos. Mag. 89 (2009) 535-552.

[11] D.A. porter, K.E. Easterling, Phase Transformations in Metals and Alloys, second ed., Chapman and Hall, London, 1992 pp. 279.

[12] N.G. Jones, M. Jackson, On mechanism of flow softening in Ti-5Al-5Mo-5V-3Cr alloy, Mater. Sci. Tech. 27 (2011) 1025-1032.

[13] N.G. Jones, R.J. Dashwood, D. Dye, M. Jackson, The flow behavior and microstructural evolution of Ti-5Al-5Mo-5V-3Cr during isothermal forging, Metall. Mater. Trans. A 40 (2009) 1944-1954.

[14] M. Jackson, N.G. Jones, D. Dye, R.J. Dashwood, Effect of initial microstructure on plastic flow behavior during isothermal forging of Ti-10V-2Fe-3Al, Mater. Sci. Eng. A 501 (2009) 248-254.

Chapter 4 Effect of 2-step aging on microstructure and mechanical properties

4.1 Introduction

For metastable β-Ti alloys, the microstructure consisted of primary α phase and secondary α phase is very important and is commercially the most interesting, since it can provide the best combinations of mechanical properties [1, 2]. In order to obtain this kind of microstructure, the processing of Ti-5553 alloy normally consists of hot forging in the α+β filed which is usually at 800 ºC (56 ºC below the β-transus temperature) and subsequent aging which is performed between 560 ºC and 677 ºC [3, 4].

The influences of the volume fraction, particle size and morphology on the mechanical properties of Ti-5553 alloy were partially studied in Chapter 3. Consider the sensitivity of the mechanical properties to the microstructure, the precipitation of secondary a phase should have a strong effect on the mechanical properties. Therefore, in order to develop a deep fundamental understanding of the microstructural evolution and the corresponding mechanical properties in Ti-5553 alloy, step aging was performed.

4.2 Experimental procedures

4.2.1 Materials preparation

The Ti-5553 alloy was prepared and processed as shown in Section 2.2.1. The Ti-5553 alloy was solution treated (ST) above the β transus temperature, which is 856 ºC, at 1000 ºC for 3.6 ks. HPT processing was carried out under a compressive pressure of 5 GPa, a rotation speed of 0.2 rpm and the rotation number of HPT processing (N) was N = 10. For the solution treated samples (ST samples) or the HPT processed samples (HPT samples), 2-step isothermal aging was performed. The first aging was done at 800 ºC for 3.6 ks and the second aging was done at the temperatures ranging from 550 ºC to 700 ºC for 14.4 ks or at 600 ºC for 1.2 to 360 ks. All the heat treatments were performed in an Ar atmosphere and followed by water quenching.

4.2.2 Materials characterization

Microstructural characterization was carried out using scanning electron microscopy (SEM, JEOL JSM-7001F, 20 kV). Backscattered electron (BSE) SEM observations and electron backscattered diffraction (EBSD) were carried out on the cross-sections of the samples mounted in resin and the samples were

prepared by conventional mechanical grinding and polishing. The step size of EBSD was set to 20 nm. The average particle size and volume fraction of α phase were measured by the image analysis with the SEM images. Disk samples (3 mm in diameter) for TEM analysis were cut from the median plane of the disk and thinned to perforation using a Gatan precision ion polishing system.

Vickers microhardness measurements were carried out with an applied load of 0.98 N for 15 seconds along the radius of the disks on the cross-section. And the hardness was measured on the position 1/4 and 1/2 of the thickness, which is about the surface region and the central region, respectively. The schematic illustration of the microhardness measurements on the cross-section is shown in Fig. 2.3 in Section 2.2.2. The miniature tensile specimens with a gauge section of 4 mm x 1 mm x 0.6 mm, as shown in Fig. 2.4 in Section 2.2.2, were cut by electron discharge machine (EDM) from the disks so that the center of the gauge section locates at the position 1.5 mm away from the disk center. The tensile specimens were electrochemical polished to make sure a smooth surface. The tensile tests were carried out at a strain rate of 2×10^{-3} s^{-1} and the strain was monitored by video-extensometer with 3 μm resolution.

The nanohardness of the α phase and β phase was measured by nanoindentation using a Hysitron Triboindenter TI950 in a load control mode. Both α and β phases were indented in at least 30 positions with a peak load of 500 μN at a loading/unloading rate of 50 μN/s. The indenter was held at peak force for 5 s before unloading. More details on nanoindentation were shown in Section 3.2.2.

4.3 Results

4.3.1 Microstructural evolution in ST and HPT samples

4.3.1.1 After first aging

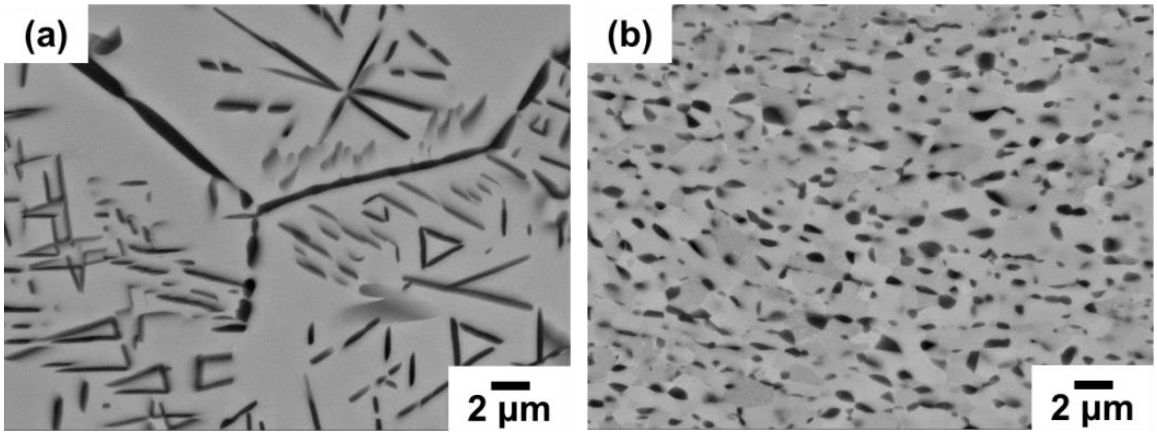

Fig. 4.1 BSE-SEM images on the morphology of α phase in the Ti-5553 alloy after first aging at 800 °C for 3.6 ks. (a) ST sample and (b) HPT sample.

Fig. 4.1(a) and (b) respectively show the BSE-SEM images of the ST sample and HPT sample aged at 800 °C for 3.6 ks. Grain boundary α phase films and the intragranular α phase (dark contrast) with an acicular morphology can be seen in the ST sample. In the HPT sample, there is no grain boundary α phase formed and the α phase shows equiaxed morphology. The volume fraction and particle size of α phase were

measured by image analysis with the SEM images. The measured volume fraction of α phase in the ST sample and HPT sample is 15.8% and 17.7%, respectively. The average particle size of acicular α phase in the ST sample is 2.18 ± 0.92 μm in length and 0.27 ± 0.08 μm in thickness. The average particle size of equiaxed α phase in the HPT sample is 0.70 ± 0.24 μm.

After first aging at 800 °C for 3.6 ks, the average microhardness is 291.4 ± 6.5 *Hv* in the ST sample and 292.1 ± 3.3 *Hv* in the HPT sample. The tensile-testing results show that the ST sample has an ultimate tensile strength of 956.1 ± 16.4 MPa and an elongation to failure of 8.2 ± 0.7%, while the HPT sample has an ultimate tensile strength of 1038.1 ± 14.8 MPa and an elongation to failure of 9.1 ± 0.7%. The tensile stress-strain curves for the ST sample and HPT sample are shown in Fig. 4.2. All the results suggest that the ST sample and HPT sample have similar mechanical properties after first aging at 800 °C for 3.6 ks.

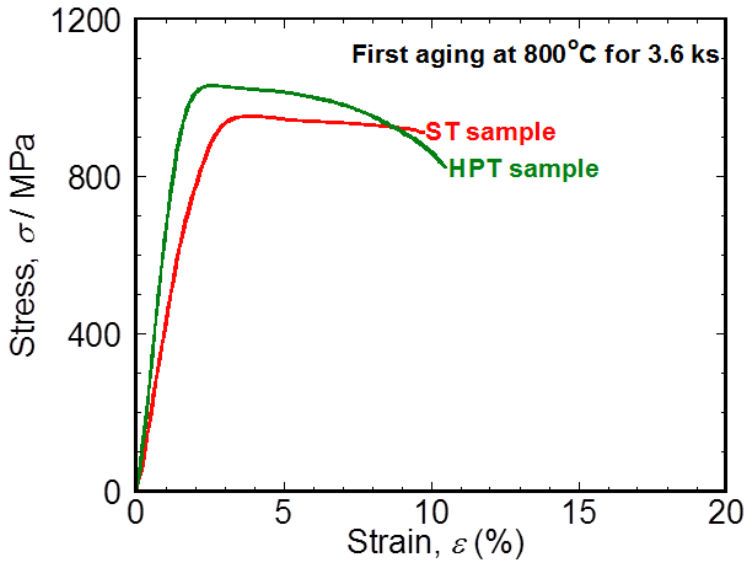

Fig. 4.2 Tensile stress-strain curves for the ST sample and HPT sample after first aging at 800 °C for 3.6 ks.

4.3.1.2 After second aging

The BSE-SEM images of the ST samples after second aging at different temperatures for 14.4 ks are shown in Fig. 4.3. The microstructures consist of coarse primary α phase and fine secondary α phase precipitated inside the β matrix and grain boundary α phase (GB α). The primary, secondary and GB α phases are respectively indicated by the arrows in Fig. 4.3(a). Both the primary and secondary α phases have acicular shape. The distribution of the primary α phase is heterogeneous. The GB α phase films are thick and continuous, as shown in Fig. 4.3(a)-(c).

Fig. 4.4 shows the BSE-SEM images of the HPT samples after second aging at different temperatures for 14.4 ks. The primary, secondary and GB α phases are respectively indicated by the arrows in Fig. 4.4(a). The precipitation of the equiaxed primary α phase is homogeneous. The β grains in the HPT samples are very fine, with an average grain size less than 2 μm. The fine β grains limit the growth of secondary α phase and reduce the thickness and continuity of grain boundary α phase films. Aged at higher temperature, there is almost no secondary α phase formed.

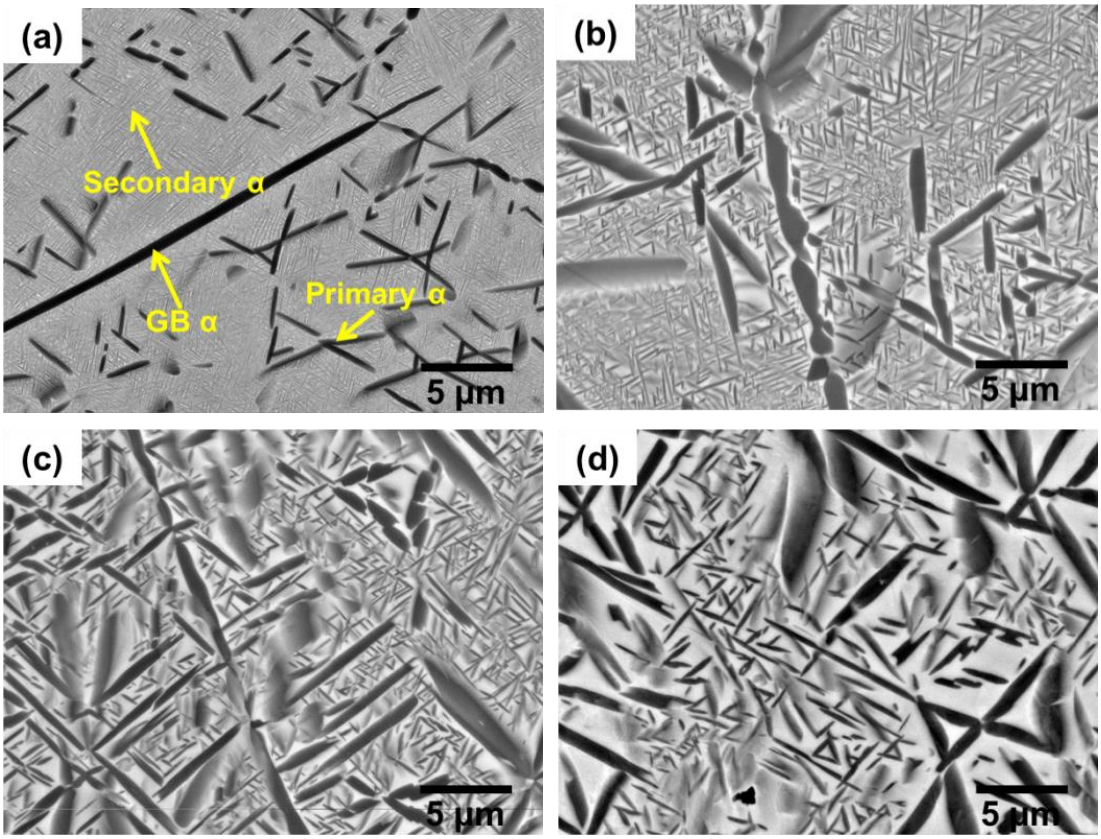

Fig. 4.3 BSE-SEM images on the morphology of α phase in the ST samples after second aging at different temperatures for 14.4 ks. (a) 550 ºC, (b) 600 ºC, (c) 650 ºC, and (d) 700 ºC.

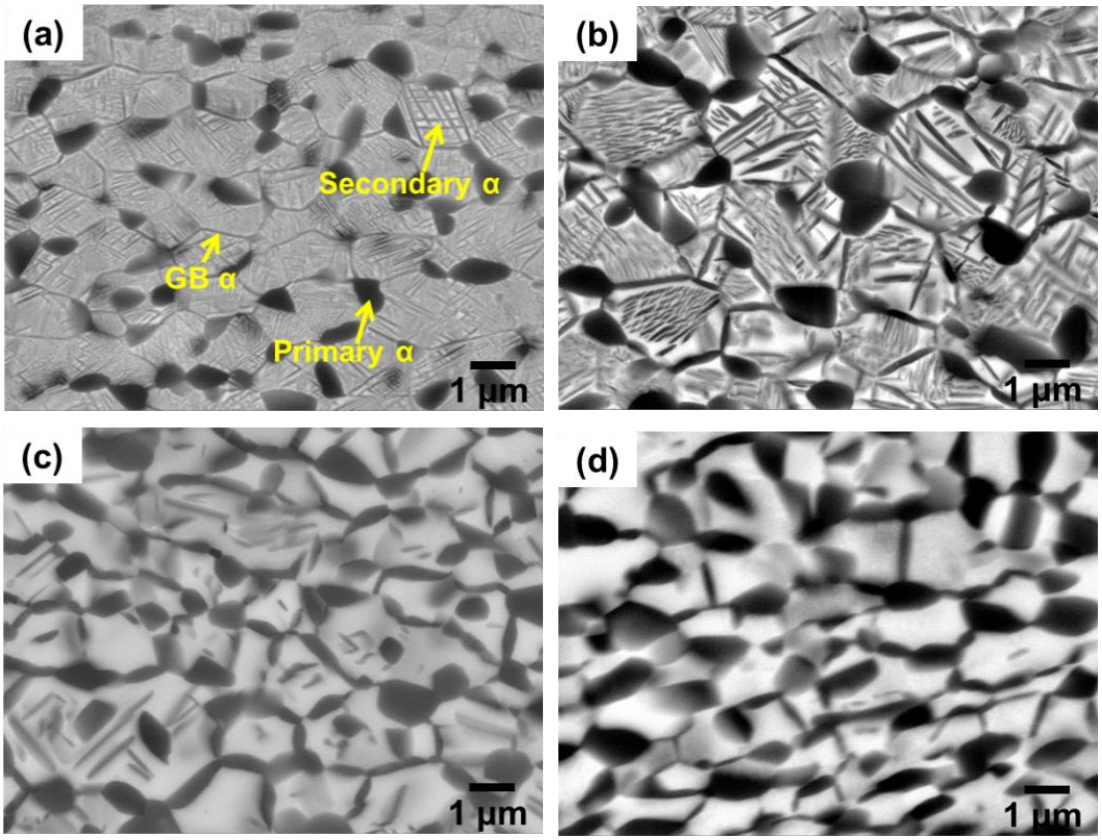

Fig. 4.4 BSE-SEM images on the morphology of α phase in the HPT samples after second aging at different temperatures for 14.4 ks. (a) 550 ºC, (b) 600 ºC, (c) 650 ºC, and (d) 700 ºC.

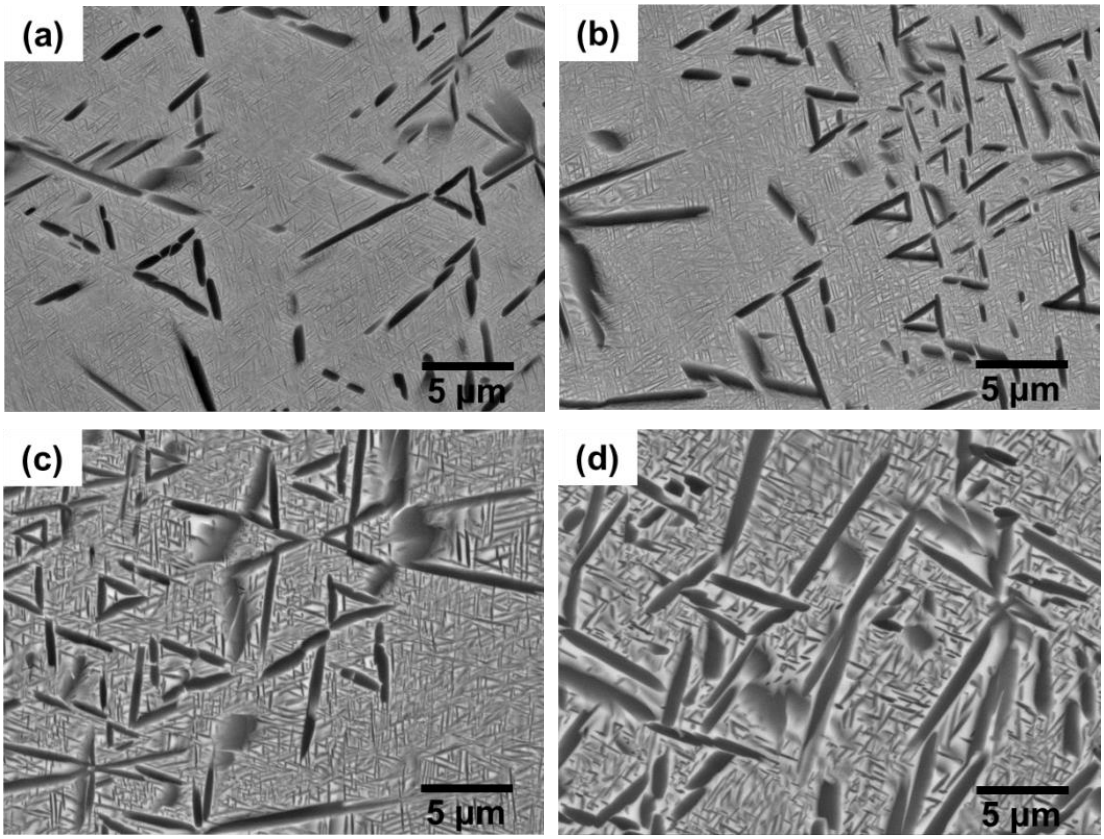

Fig. 4.5 BSE-SEM images on the morphology of α phase in the ST samples after second aging at 600 ºC for different time. (a) 1.2 ks, (b) 3.6 ks, (c) 72 ks, and (d) 360 ks.

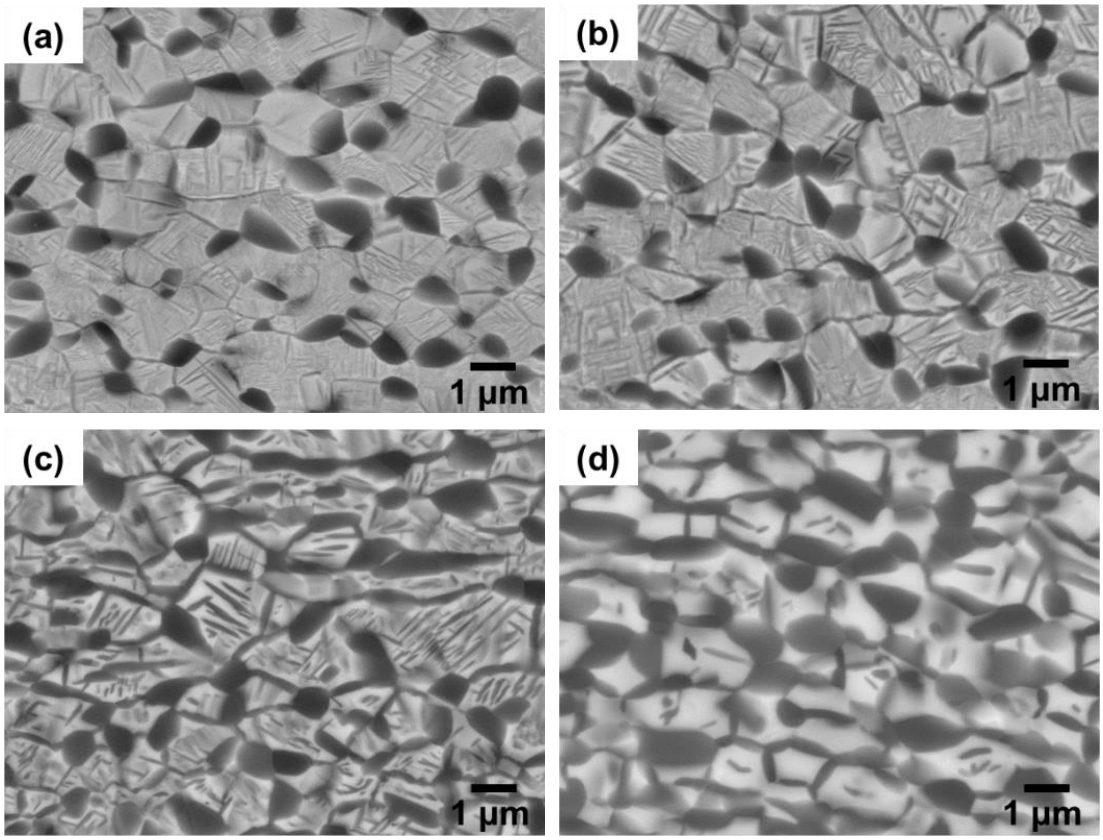

Fig. 4.6 BSE-SEM images on the morphology of α phase in the HPT samples after second aging at 600 ºC for different time. (a) 1.2 ks, (b) 3.6 ks, (c) 72 ks, and (d) 360 ks.

Fig. 4.5 shows the BSE-SEM images in the ST samples aged at 600 °C for different time. Aged at 600 °C, there is a large amount of secondary α phase precipitated. The primary and secondary α phases show a significant growth with increasing the aging time.

Fig. 4.6 shows the BSE-SEM images in the HPT samples aged at 600 °C for different time. With increasing the aging time, the growth of the primary α phase is not significant. After aging from 1.2 ks to 72 ks, there is a significant growth in the secondary α phase, especially in the thickness direction. However, there is a marked decrease in the volume fraction of secondary α phase after further aging. As shown in Fig. 4.6(d), there is almost no secondary α phase formed after aging for 360 ks.

Depending on the SEM images, the particle size of the primary α phase and secondary α phase was measured. For the quantitative analysis on the particle size, more than 200 α particles were selected. However, it must be remembered that there could also be some uncertainty in the particle size measured form SEM images. Fig. 4.7(a) and (b) respectively shows the particle size of the primary α phase and secondary α phase in the ST samples. For both the primary and secondary α phases, the tendency is that the particle size increases by increasing the aging time or aging temperature. After aging at 600 °C, the length of the primary α phase increases from 3.72 ± 1.73 μm to 4.23 ± 1.97 μm while the thickness increases from 0.46 ± 0.12 μm to 0.73 ± 0.23 μm by increasing the aging time from 1.2 ks to 360 ks. By increasing the aging temperature from 550 °C to 700 °C, the length of the primary α phase increases from 2.88 ± 0.93 μm to 5.08 ± 1.64 μm while the thickness increases from 0.37 ± 0.07 μm to 0.71 ± 0.19 μm after aging for 14.4 ks. For the secondary α phase, the length increases from 0.68 ± 0.29 μm to 0.91 ± 0.48 μm while the thickness increases from 0.06 ± 0.01 μm to 0.14 ± 0.04 μm by increasing the aging time from 1.2 ks to 360 ks after aging at 600 °C. By increasing the aging temperature from 550 °C to 700 °C, the length increases from 0.75 ± 0.29 μm to 1.68 ± 0.56 μm while the thickness increases from 0.06 ± 0.01 μm to 0.17 ± 0.04 μm after aging for 14.4 ks. Fig. 4.7(c) and (d) respectively shows the particle size of the primary α phase and secondary α phase in the HPT samples. There is a slight increase in the particle size of the primary and secondary α phases with increasing aging time or aging temperature. Aged at 600 °C, the average particle size of the primary α phase increases from 0.68 ± 0.21 μm to 0.83 ± 0.29 μm when increase the aging time from 1.2 ks to 360 ks. Aged for 14.4 ks, the particle size increases from 0.81 ± 0.27 μm to 0.91 ± 0.22 μm when increase the aging temperature from 550 °C to 700 °C. For the secondary α phase, the length increases from 0.42 ± 0.16 μm to 0.56 ± 0.20 μm while the thickness increases from 0.04 ± 0.01 μm to 0.12 ± 0.04 μm by increasing the aging time from 1.2 ks to 360 ks after aging at 600 °C. When increase the aging temperature from 550 °C to 650 °C, the length increases from 0.42 ± 0.19 μm to 0.54 ± 0.20 μm while the thickness increases from 0.04 ± 0.01 μm to 0.07 ± 0.02 μm after aging for 14.4 ks. In addition, the results also show that the primary and secondary α phases in the HPT samples are finer than those in the ST samples.

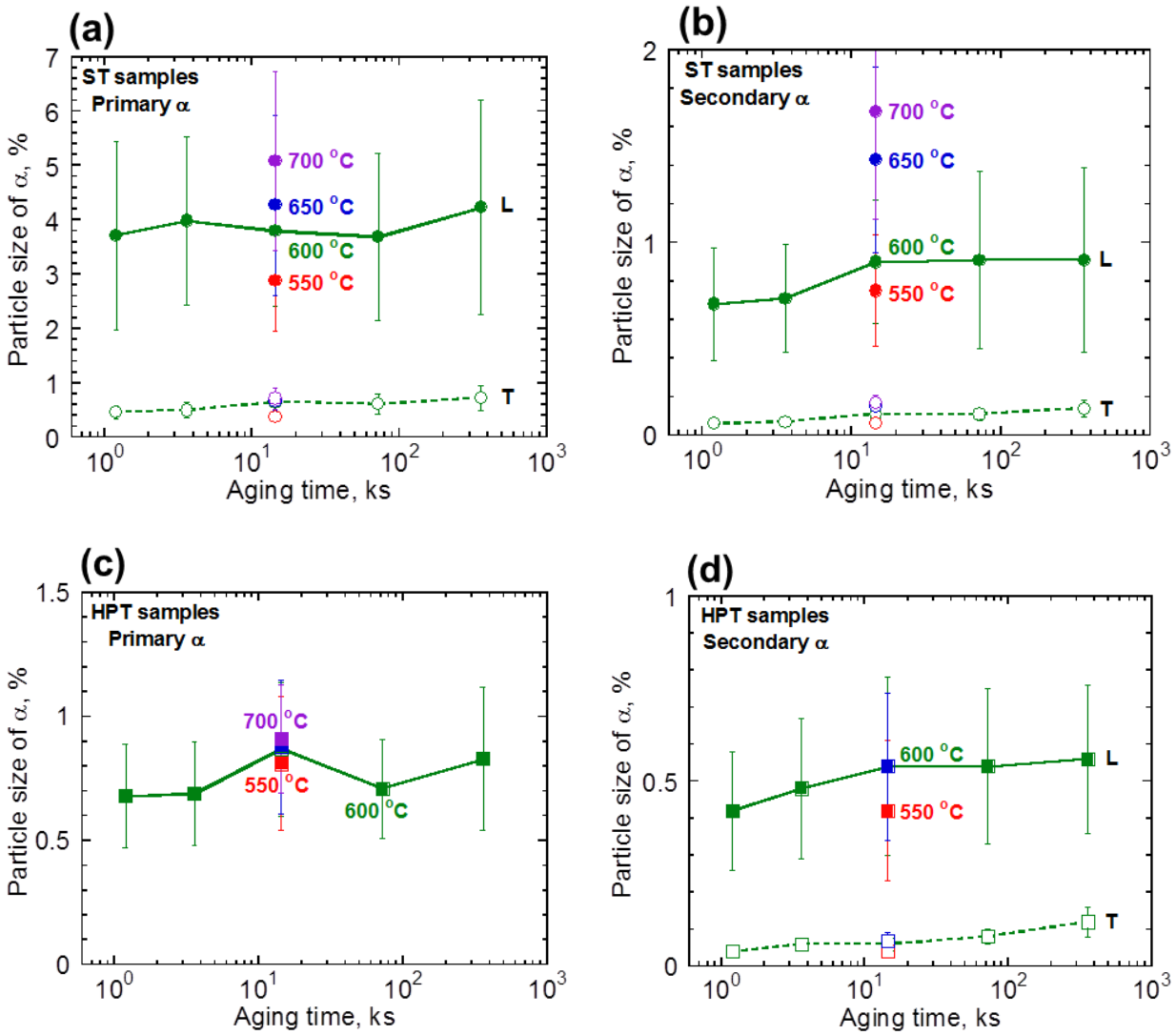

Fig. 4.7 Average particle size in the ST samples: (a) primary α phase and (b) secondary α phase; and average particle size in the HPT samples: (c) primary α phase and (d) secondary α phase.

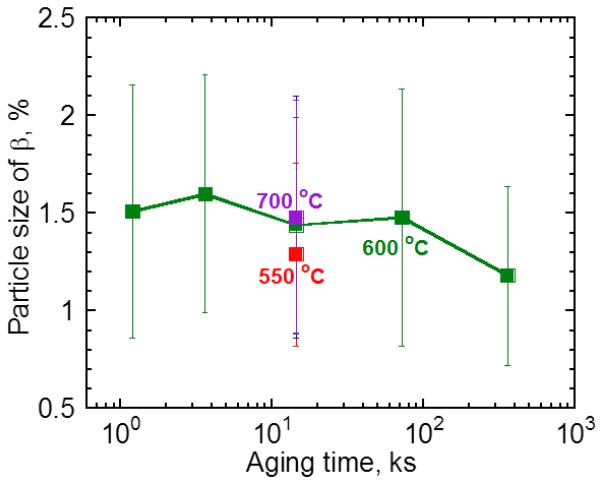

Fig. 4.8 Average β grain size in the HPT samples after second aging.

Fig. 4.8 shows the β grain size in the HPT samples. The change in the β grain size is not much by changing the aging time or aging temperature. The β grain size decreases from 1.51 ±0.65 μm to 1.18 ±0.46 μm after aging at 600 ºC from 1.2 ks to 360 ks, and it increases slightly from 1.29 ±0.47 μm to 1.48 ±0.60 μm after aging from 550 ºC to 700 ºC for 14.4 ks.

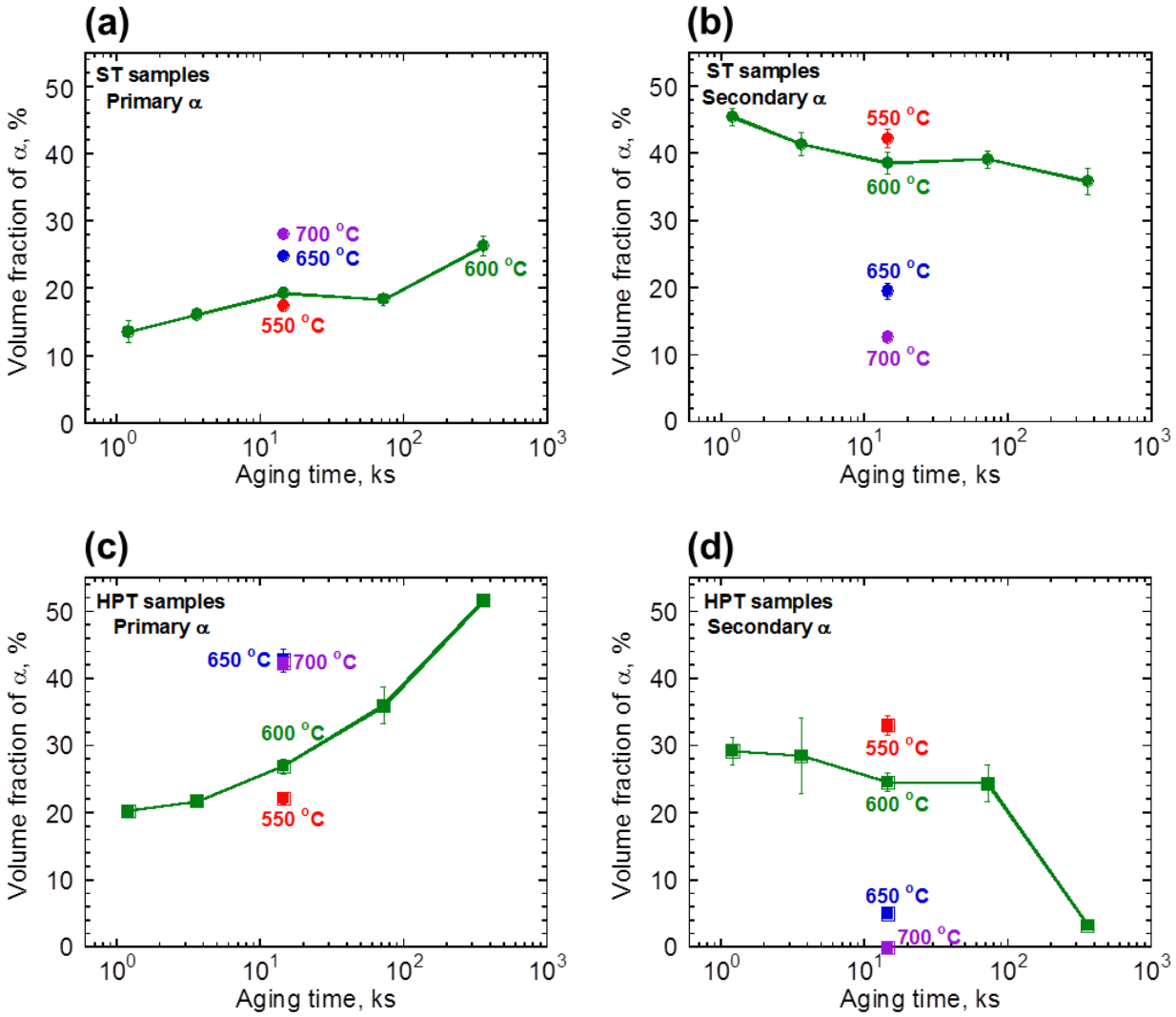

Fig. 4.9 Volume fraction of α phase in the ST samples: (a) primary α phase and (b) secondary α phase; and volume fraction of α phase in the HPT samples: (c) primary α phase and (d) secondary α phase.

The volume fraction of the primary and secondary α phases were also measured depending on the SEM images. The volume fraction of the primary α phase in the ST samples is shown in Fig. 4.9(a). Aged at 600 ºC, there is an increase in the volume fraction of the primary α phase from 13.6 ±1.6% to 26.1 ±1.5% when increase the aging time from 1.2 ks to 360 ks. There is also an increase from 17.5 ±0.9% to 28.0 ±0.8% by increasing the aging temperature from 550 ºC to 700 ºC after aging for 14.4 ks. Fig. 4.9(b) shows the volume fraction of the secondary α phase in the ST samples. Different with the primary α phase, the volume fraction of the secondary α phase decreases with increasing the aging time or temperature. Aged at 600 ºC, it decreases from 45.5 ±1.3% to 35.8 ±2.0% after aging from 1.2 ks to 360 ks. And there is a marked decrease

from 42.3 ± 1.3% to 12.7 ± 0.4% after aging from 550 °C to 700 °C for 14.4 ks. For the volume fraction of the primary α phase in the HPT samples, it shows an increase by increasing the aging time or temperature, as shown in Fig. 4.9(c). Aged at 600 °C, it increases from 20.3 ± 0.8% to 51.7 ± 0.6% after aging from 1.2 ks to 360 ks. Also, it increases from 22.2 ± 0.9% to 42.2 ± 0.6% after aging from 550 °C to 700 °C for 14.4 ks. Fig. 4.9(d) shows the volume fraction of the secondary α phase in the HPT samples, which decreases with increasing the aging time or temperature. Aged at 600 °C, it decreases from 29.2 ± 2.1% to 3.3% after aging from 1.2 ks to 360 ks. And it decreases from 33.0 ± 1.5% to 0% after aging from 550 °C to 700 °C for 14.4 ks. In addition, the results shown by Fig. 4.9 show that the volume fraction of the primary α phase is higher in the HPT samples than in the ST samples, while the volume fraction of the secondary α phase is lower in the HPT samples than in the ST samples.

4.3.2 Mechanical properties in ST and HPT samples

After 2-step aging, the microhardness and tensile properties of the ST samples and HPT samples were measured. The evolution of Vickers microhardness with the aging time or aging temperature was shown in Fig. 4.10. Fig. 4.10(a) shows the microhardness of the ST samples. The hardness is 409.2 ± 12.1 *H*v after aging at 600 °C for 1.2 ks and decreases to 364.9 ± 8.2 *H*v after aging for 360 ks. In addition, the hardness is 415.3 ± 7.8 *H*v after aging at 550 °C for 14.4 ks and decreases to 326.2 ± 9.5 *H*v after aging at 700 °C for 14.4 ks. Fig. 4.10(b) shows the microhardness of the HPT samples. The hardness decreases from 398.2 ± 10.2 *H*v to 360.8 ± 7.3 *H*v after aging at 600 °C from 1.2 ks to 360 ks. And the hardness decreases from 411.1 ± 5.8 Hv to 331.1 ± 6.6 *H*v after aging from 550 °C to 700 °C for 14.4 ks. The results in Fig. 4.10 also show that The ST samples and HPT samples have the same hardness.

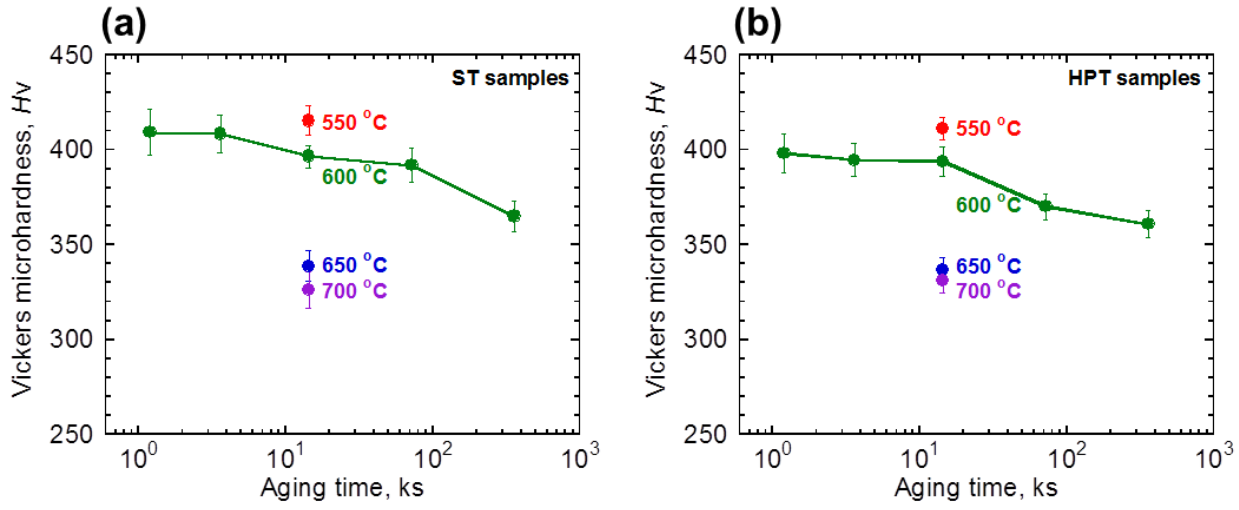

Fig. 4.10 Evolution of microhardness with the aging time or aging temperature: (a) ST samples and (b) HPT samples.

Fig. 4.11(a) and (b) respectively shows the tensile stress-strain curves of the ST samples and HPT samples aged at different temperature for 14.4 ks. A higher aging temperature results in a lower ultimate

tensile strength (UTS) along with a higher elongation to failure (EL) in both the ST samples and HPT samples. The average UTS and EL in the ST samples and HPT samples are listed in Fig. 4.11(c). When increase the second aging temperature from 550 ºC to 700 ºC, the UTS decreases from 1382 ± 4 MPa to 1060 ± 57 MPa while the EL increases from 0.8 ± 0.1% to 8.6 ± 0.1% in the ST samples, and the UTS decreases from 1354 ± 22 MPa to 1102 ± 16 MPa while the EL increases from 4.4 ± 1.6% to 14.8 ± 1.1% in the HPT samples. A similar UTS is obtained in the ST samples and HPT samples, but a much higher EL is obtained in the HPT samples.

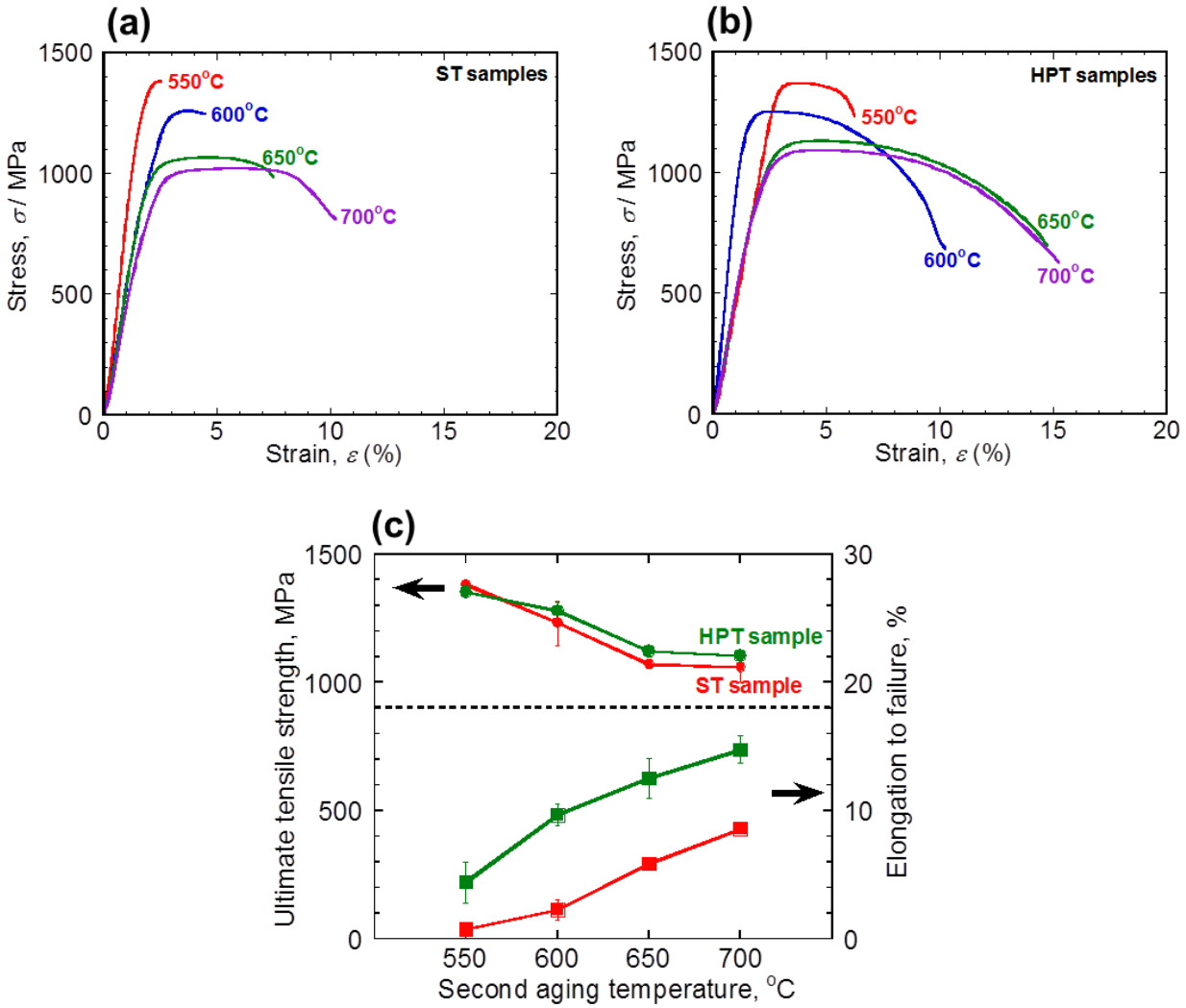

Fig. 4.11 Tensile stress-strain curves in (a) ST samples and (b) HPT samples after aging at different temperature for 14.4 ks. (c) Average ultimate tensile strength and elongation to failure in the ST samples and HPT samples.

The tensile stress-strain curves of the ST samples and HPT samples aged at 600 ºC for different time are respectively shown in Fig. 4.12(a) and (b). And the average UTS and EL are listed in Fig. 4.12(c). It shows a tendency that there is a decrease in the UTS along with an increase in the EL by increasing the aging time from 1.2 ks to 360 ks. The UTS decreases from 1187 ± 54 MPa to 1009 ± 27 MPa while the EL increases from 0.9% to 2.2 ± 0.4% in the ST samples, and the UTS decreases from 1264 ± 19 MPa to 953 ± 7 MPa

while the EL increases from 4.7 ± 1.1% to 10.3 ± 0.8% in the HPT samples. Also, the results show that the ST samples and HPT samples have a similar UTS, but the HPT samples have much higher elongation to failure.

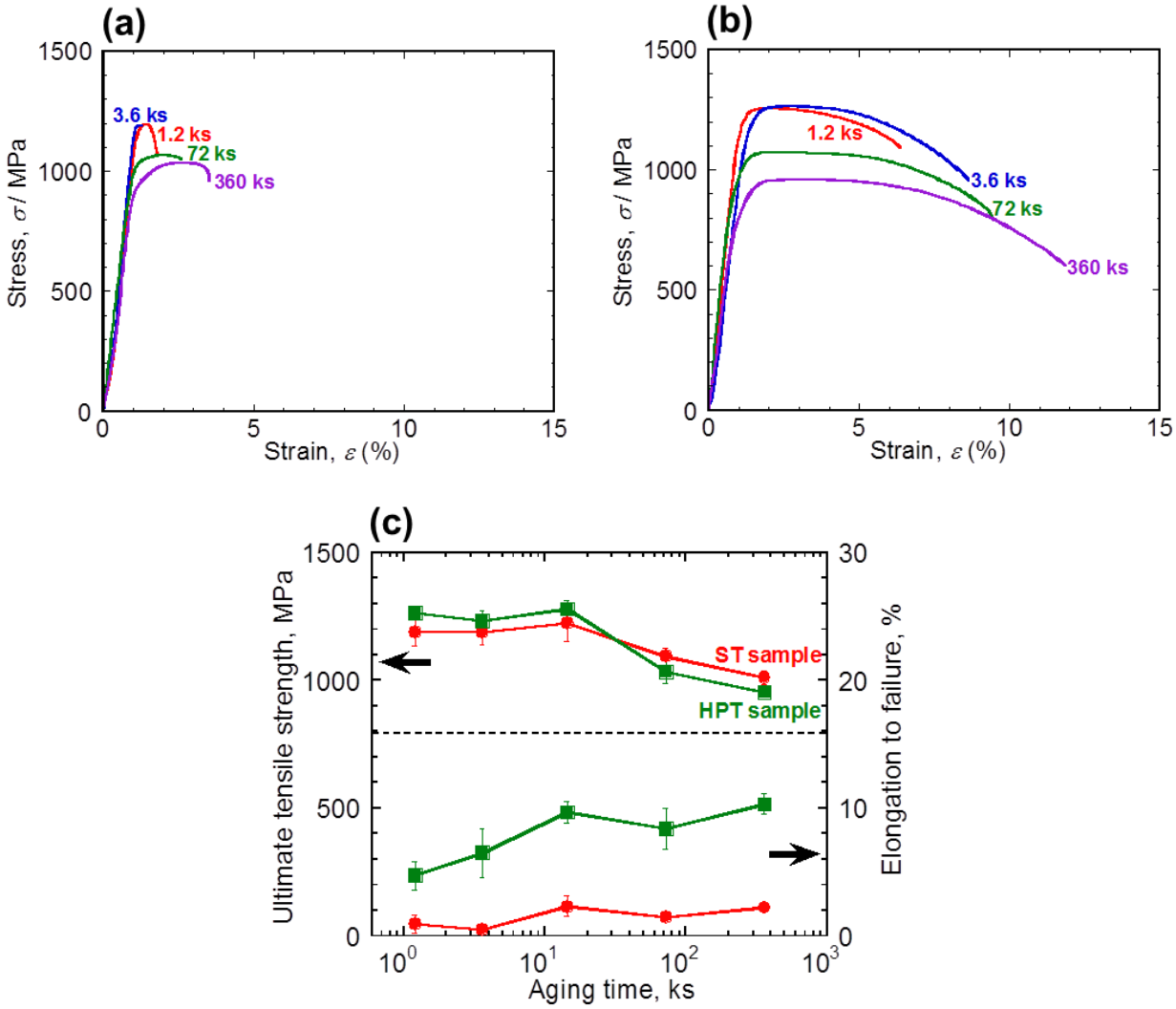

Fig. 4.12 Tensile stress-strain curves in (a) ST samples and (b) HPT samples aged at 600 ºC for different time. (c) Average ultimate tensile strength and elongation to failure in the ST samples and HPT samples.

Fig. 4.13(a) shows the fracture surface of the ST sample that second aged at 600 ºC for 14.4 ks. The SEM fractograph shows a mixed-mode, with brittle and ductile fracture. The smooth facets correspond to the low plasticity intergranular fracture and the dimple zones correspond to the transgranular fracture. Crack path appears to follow the grain boundaries as well as through the grains. In addition, secondary cracking can also be seen. The dimple zone is shown by the SEM fractograph at high magnification in Fig. 4.13(b). Fig. 4.13(c) shows the fracture surface of the ST sample that second aged at 650 ºC for 14.4 ks. The transgranular fracture becomes to be dominant at this aging temperature. The fine dimples are shown by the high magnification SEM fractograph in Fig. 4.13(d).

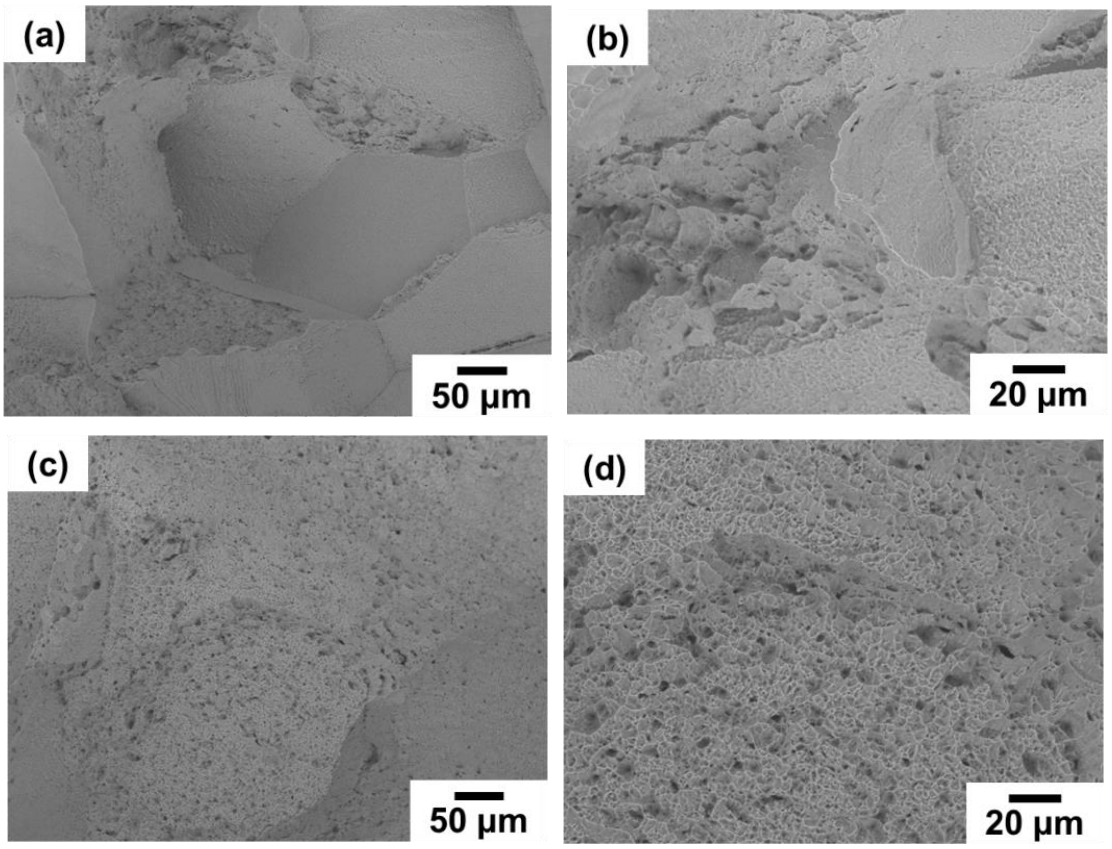

Fig. 4.13 Fracture surface in the ST sample. Aged at 600 ºC for 14.4 ks: (a) low magnification and (b) high magnification; Aged at 650 ºC for 14.4 ks: (c) low magnification and (d) high magnification.

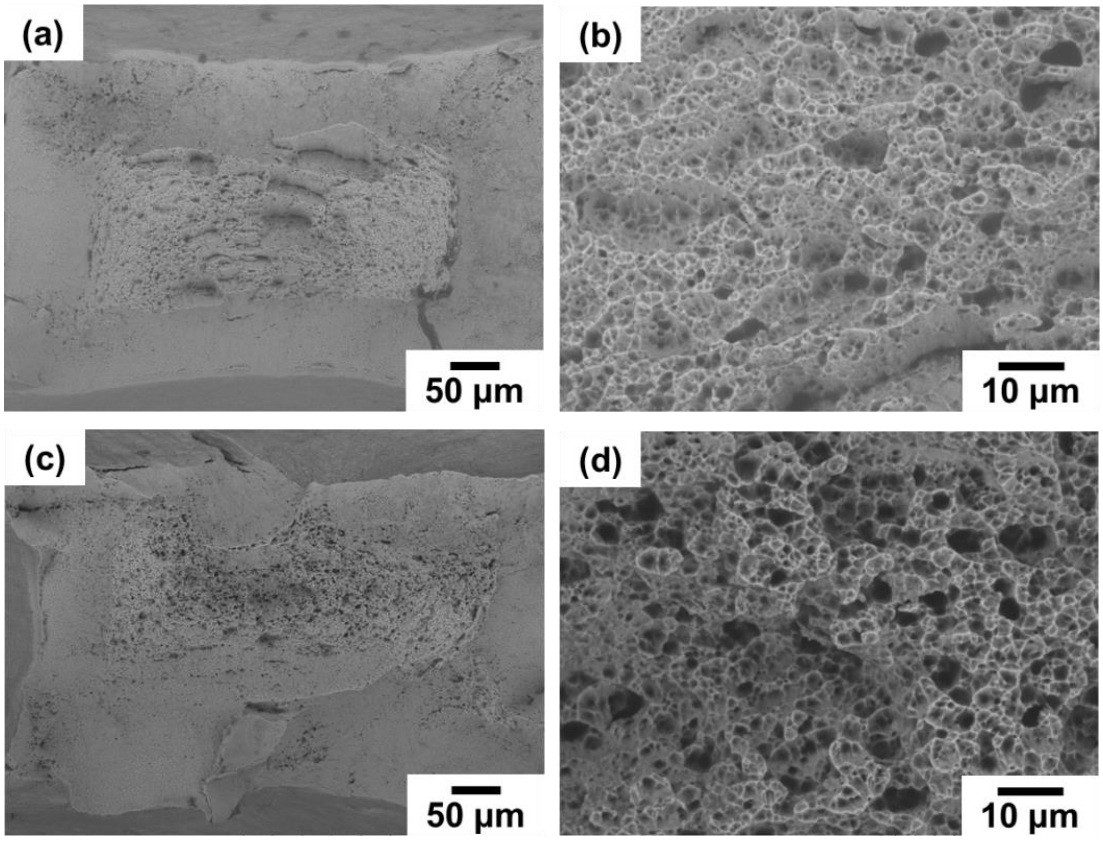

Fig. 4.14 Fracture surface in the HPT sample. Aged at 600 ºC for 14.4 ks: (a) low magnification and (b) high magnification; Aged at 650 ºC for 14.4 ks: (c) low magnification and (d) high magnification.

The fracture surface of the HPT sample after the second aging at 600 ºC for 14.4 ks is shown in Fig. 4.14(a). The SEM fractograph exhibits a ductile fracture accompanied with secondary cracking. The dimple region and the shear tip can be found on the fractograph. In the dimple region, as shown in Fig. 4.14(b), the dimple size is uniform and the micro-voids can be observed. The fracture features of the HPT sample after the second aging at 650 ºC for 14.4 is similar, as shown in Fig. 4.14(c) and (d). And more micro-voids can be seen in the dimple region.

4.4 Discussion

This study showed that, for Ti-5553 alloy with a variety of microstructures, a wide range of ultimate tensile strength and ductility could be achieved and that the ductility was strongly influenced by the microstructure. The present study also confirmed that the 2-step aged HPT samples had the same ultimate tensile strength but much better ductility compared with the step aged ST samples.

Based on the SEM microstructures that mentioned in the results part, it is clearly that the introduction of prior deformation by HPT has great effects on the microstructure. Firstly, HPT changed the morphology of the primary α phase, promoting the formation of equiaxed shape instead of acicular shape. The formation of the equiaxed morphology had been discussed in Section 3.4. Moreover, the equiaxed primary α phase in the HPT samples had a more homogeneous distribution compared with the acicular primary α phase in ST the samples. Secondly, grain refinement by HPT led to ultrafine β grains even after aging. The average β grain size in the aged HPT samples is less than 2 μm and it is much smaller than the average β grain size in the ST samples which is around 220 μm. The ultrafine β grains in the HPT samples impeded the formation of large grain boundary α phase films. Finally, the α phase was finer in the HPT samples than in the ST samples. The HPT samples had a higher volume fraction of primary α phase but a lower volume fraction of secondary α phase than the ST samples.

As discussed in Section 3.4, the precipitation of α phase has a strong influence on the mechanical properties. In the present study, the influence of the complex microstructure consisted of primary α phase and secondary α phase on the mechanical properties will also be discussed in details.

The relationships between the particle size of α phase and mechanical properties are shown in Fig. 4.15. The yield strength is indicated in the y-axis, which was calculated by the empirical relationship $\sigma_y = Hv/3$. For both the ST samples and HPT samples, the larger particle size of primary α phase leads to a lower yield strength (as shown in Fig. 4.15(a)) and a higher elongation to failure (as shown in Fig. 4.15(b)). Similarly, the larger particle size of secondary α phase leads to a lower yield strength (as shown in Fig. 4.15(c)) and a higher elongation to failure (as shown in Fig. 4.15(d)).

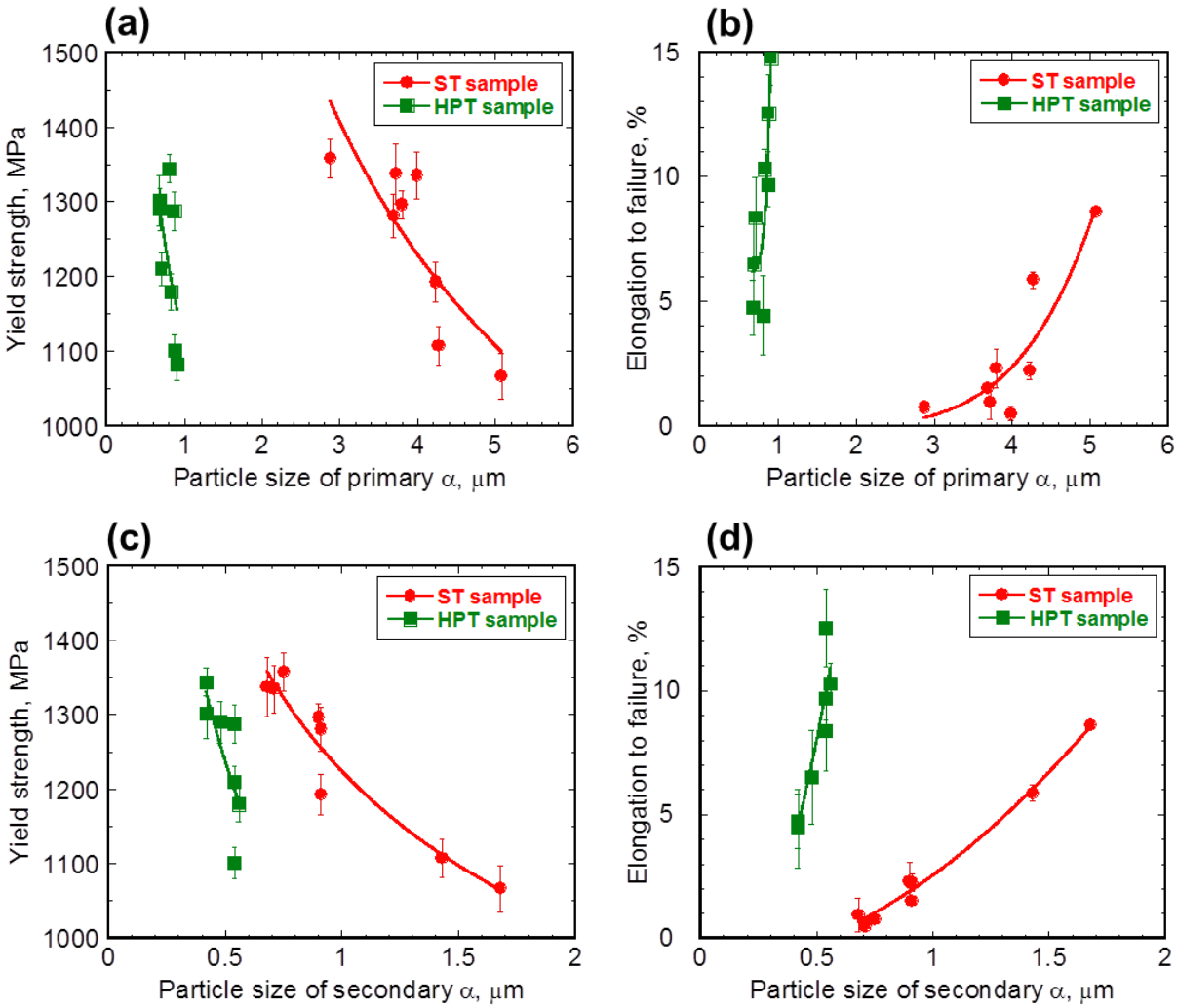

Fig.4.15 Relationship between mechanical properties and particle size of α phase: (a) yield strength *vs* primary α, (b) Elongation to failure *vs* primary α, (c) yield strength *vs* secondary α, and (d) Elongation to failure *vs* secondary α.

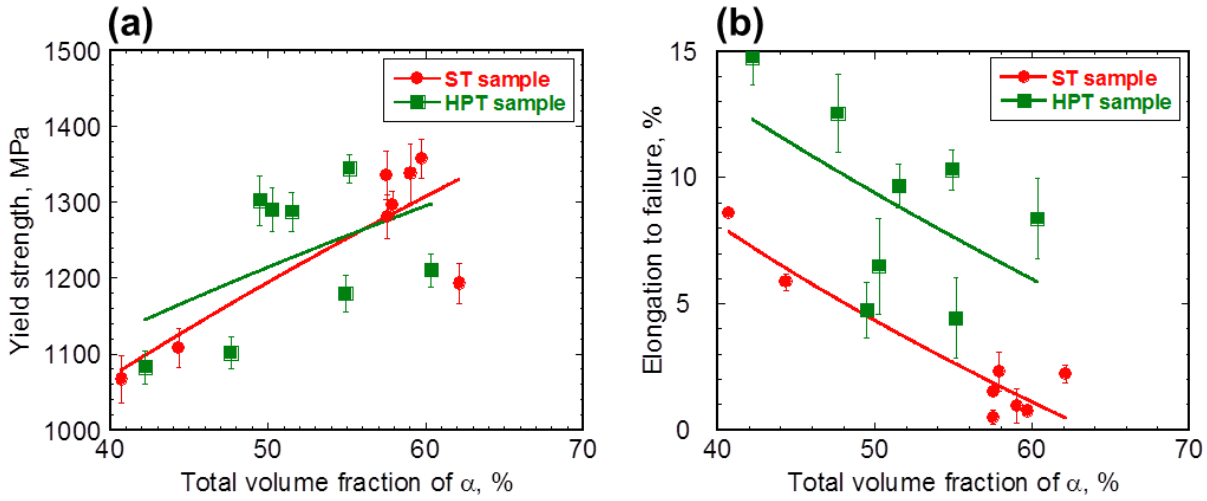

Fig.4.16 Relationship between mechanical properties and total volume fraction of α phase: (a) yield strength *vs* total volume fraction of α, (b) Elongation to failure *vs* total volume fraction of α.

The relationships between the total volume fraction of α phase (including the primary and secondary α phases) and the mechanical properties are shown in Fig. 4.16. As shown in Fig. 4.16(a), the increase in the total volume fraction of α phase leads to an increase in the yield strength. Meanwhile, the increase in the total volume fraction of α phase leads to a decrease in the elongation to failure, as shown in Fig. 4.16(b).

The relationships between the volume fraction of α phase and mechanical properties are shown in Fig. 4.17. Fig. 4.17(a) and (b) respectively shows that the increase in the volume fraction of primary α phase leads to a decrease in the yield strength and an increase in the elongation to failure. Conversely, the increase in the volume fraction of secondary α phase leads to an increase in the yield strength and a decrease in the elongation to failure, which is respectively shown in Fig. 4.17(c) and (d). From these results, it seems like that the primary α phase contributes to the ductility, while the secondary α phase contributes to the strength.

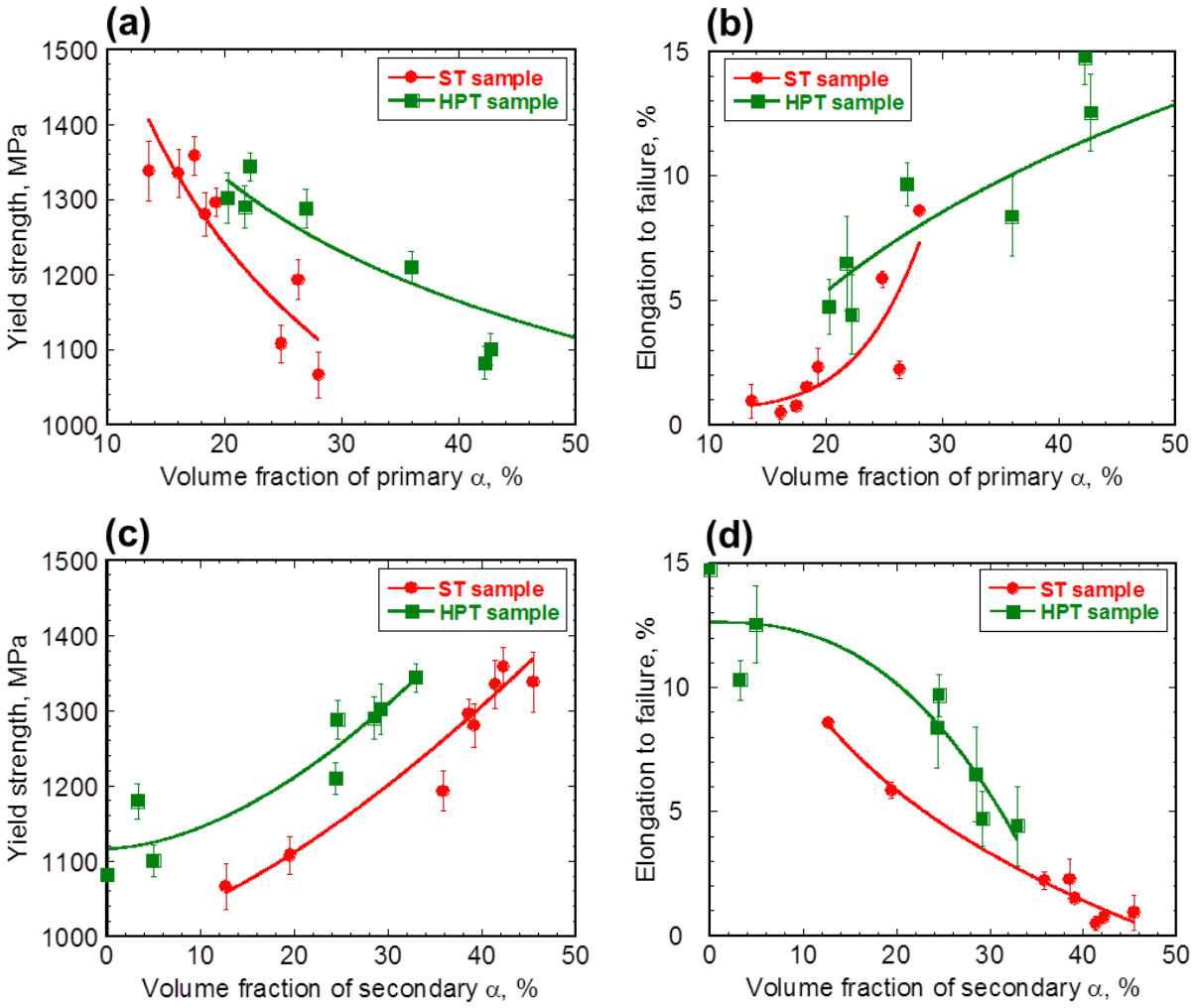

Fig.4.17 Relationship between mechanical properties and volume fraction of α phase: (a) yield strength *vs* primary α, (b) Elongation to failure *vs* primary α, (c) yield strength *vs* secondary α, and (d) Elongation to failure *vs* secondary α.

The strengthening by the precipitation of α phase follows Hall-Petch strengthening mechanism, which has been discussed in Section 3.4. For the Ti-5553 alloy with the microstructure consisted of primary α phase and secondary α phase, Hall-Petch plotting is shown in Fig. 4.16. Here it is should be noted that the average interphase space, d, was calculated from the space between secondary α phase or the space between secondary α phase and primary α phase. The increase in the volume fraction and particle size of primary α phase is at the expense of secondary α phase which can cause an increase in the value of d, consequently leading to a decrease in the yield strength and an increase in the ductility. The similar hardness (or ultimate tensile strength) in the ST samples and HPT samples is considered to be mainly due to the similar interphase space. In addition, the Hall-Petch coefficient for the ST samples, K_{ST}, was estimated to be 120 MPa(μm)$^{-1/2}$, and the Hall-Petch coefficient for the HPT samples, K_{HPT}, was estimated to be 102 MPa(μm)$^{-1/2}$. The difference between the Hall-Petch coefficient for the ST samples and HPT samples is not so large.

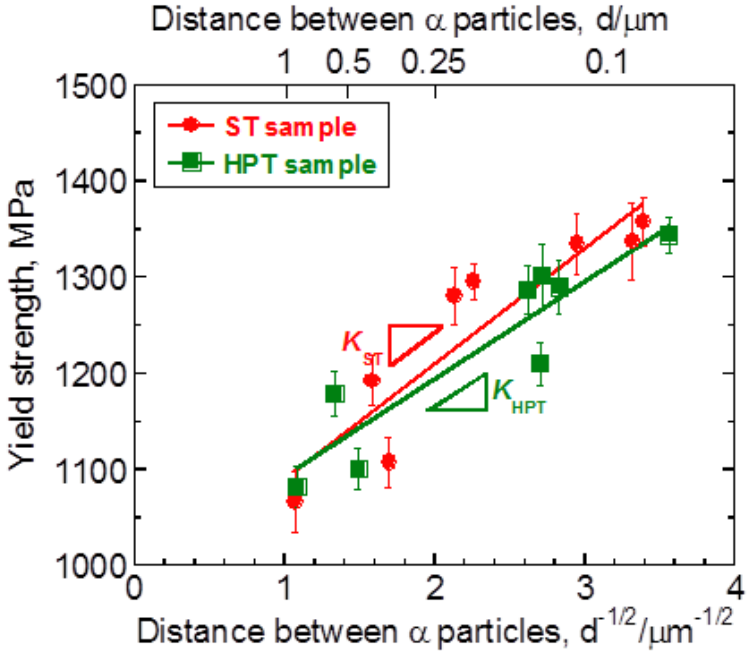

Fig. 4.18 Hall-Petch plotting for the ST samples and HPT samples after step aging.

As shown by the tensile testing results that the HPT samples have much better ductility than the ST samples. In order to understand the deformation mechanism of the HPT samples, the deformation process in the HPT samples was studied by EBSD analysis. Before tensile testing (0% strain), the inverse pole figure (IPF) maps of the HPT sample after second aging at 650 °C for 14.4 ks are shown in Fig. 4.19. In the present EBSD analysis, the crystallographic orientation is presented based on a cylindrical coordinate (Thickness, Radial, and Hoop direction) instead of the ordinary Cartesian coordinate (i.e., ND, TD, RD). The observed plane is parallel to the Hoop direction. Fig. 4.19(a) shows an overall IPF map of α and β phases. Fig. 4.19(b) and (c) respectively show the IPF map of the β phase and α phase. It is clearly that the primary α phase is surrounded by the β phase, forming network-like structure.

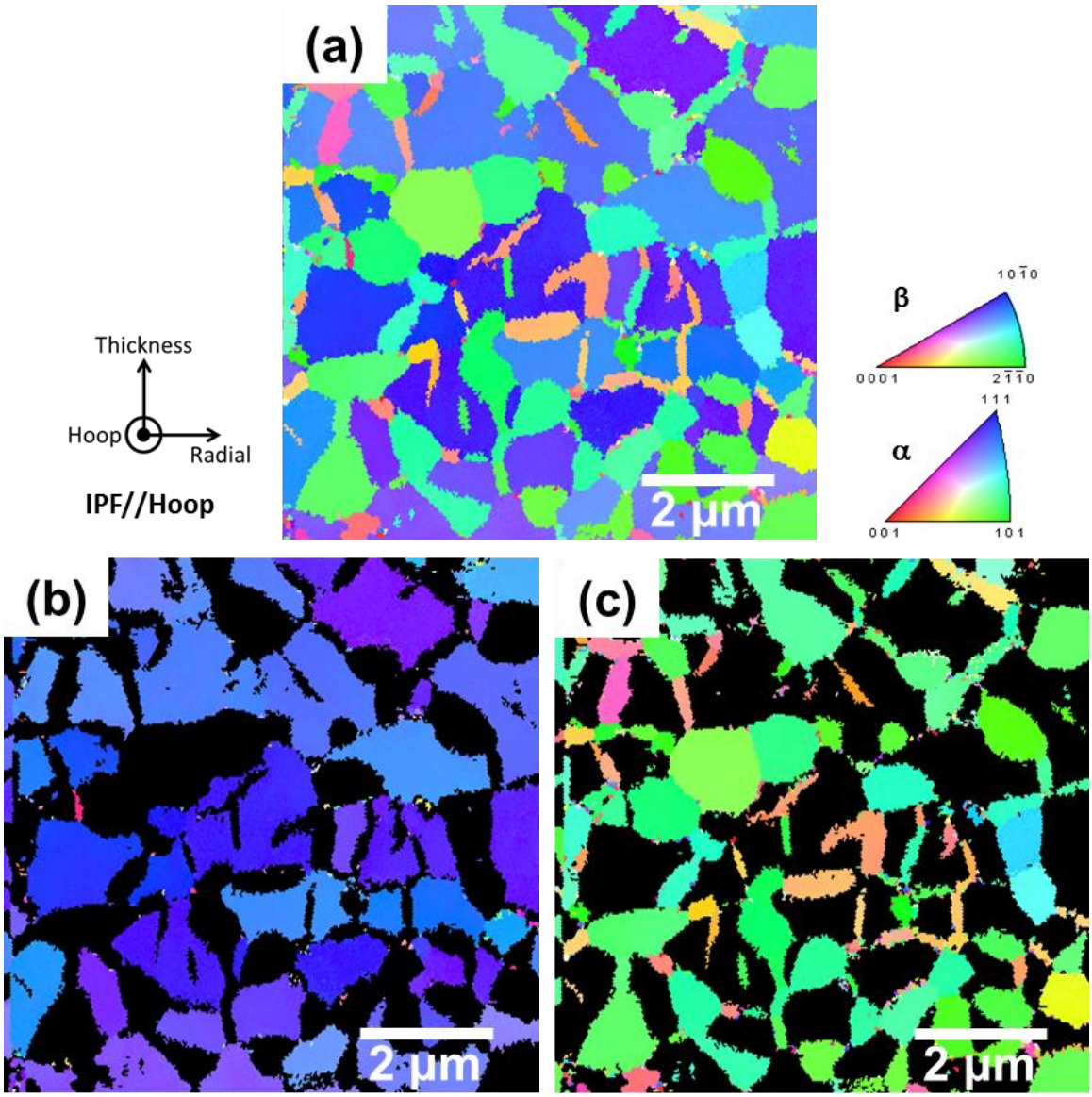

Fig. 4.19 Inverse pole figure maps before tensile testing in the HPT sample after second aging at 650 ºC for 14.4 ks.

After tensile testing with a plastic strain of 3%, the IPF maps of the HPT sample second aged at 650 ºC for 14.4 ks are shown in Fig. 4.20. The arrows indicate the tensile testing direction. Fig. 4.20(a) shows an overall IPF map of α and β phases. It is clearly from this IPF map that some areas are deformed. Compared the IPF map of β phase which is shown in Fig. 4.20(b) with the IPF map of α phase which is shown in Fig. 4.20(c), it shows that the β phase is deformed more severely than the α phase. This implies preferential plastic deformation occurs in the β phase. The reason for the preferential deformation of β phase is that the β phase is softer than the α phase which has been reported in Section 3.3. For the HPT sample after second aging at 650 ºC for 14.4 ks, the average nanohardness of the β phase measured by nanoindentation is 5.33 ± 0.23 GPa and it is much lower than the average nanohardness of the primary α phase which is 6.92 ± 0.25 GPa. In addition, accompanied with the shape change of the β phase by plastic deformation, the arrangement

of the surrounding primary α phase also undergoes a shape change which can be seen clearly in Fig. 4.20(c).

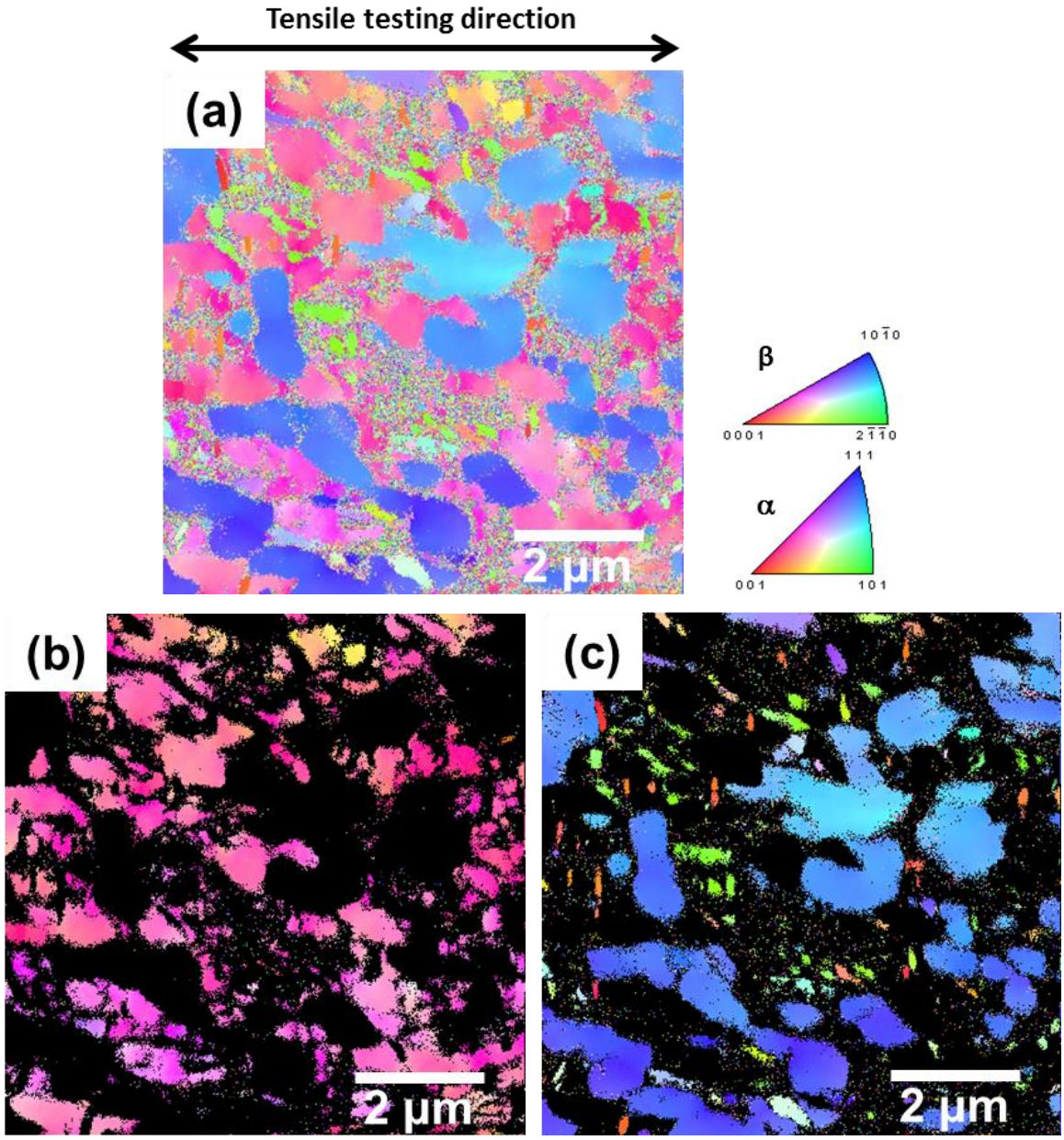

Fig. 4.20 Inverse pole figure maps after tensile testing with a plastic strain of 3% in the HPT sample second aged at 650 ºC for 14.4 ks.

Fig. 4.21 shows the IPF maps of the HPT sample second aged at 650 ºC for 14.4 ks after tensile testing with a plastic strain of 5.6%. Fig. 4.21(a) shows an overall IPF map of α and β phases, and Fig. 4.21(b) and (c) respectively shows the IPF map of α phase and β phase. The β phase is more severely deformed. The α phase is also slightly deformed and elongated along the tensile testing direction.

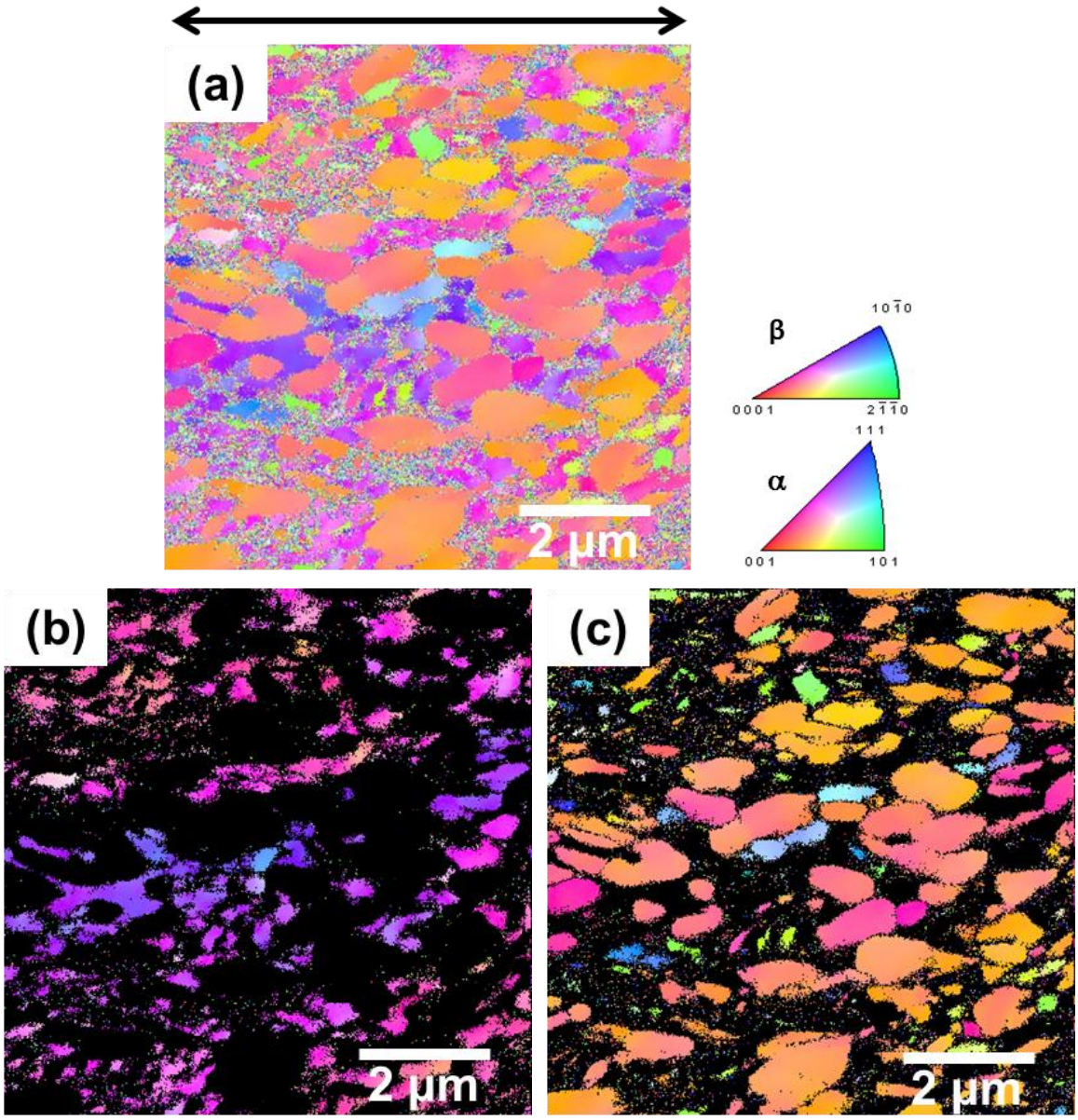

Fig. 4.21 Inverse pole figure maps after tensile testing with a plastic strain of 5.6% in the HPT sample second aged at 650 ºC for 14.4 ks.

After fracture with a plastic strain of 13.3%, the BSE-SEM image of the HPT sample second aged at 650 ºC for 14.4 ks is shown in Fig. 4.22. Both the β and primary α phases are severely deformed and elongated along the tensile testing direction. The plastic deformation is homogeneous across the structure and covers a large region.

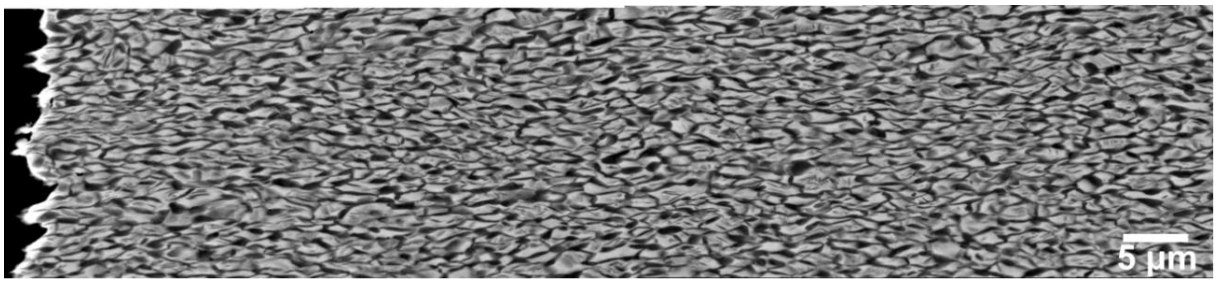

Fig. 4.22 BSE-SEM image in the HPT sample second aged at 650 ºC for 14.4 ks after fracture.

Based on the EBSD analysis and SEM images, the deformation mechanism in the HPT samples can be depicted by Fig. 4.23. Network-like structure forms in the HPT samples after step aging. The softer "core" (β phase) is surrounded by the harder "cell" (primary α phase). The softer "core" undergoes preferential plastic deformation during tensile testing. As soon as the "core" is deformed, the harder "cell" undergoes shape change to accommodate the shape change of the softer "core". The plastic deformation inside the "core" leads to the strain hardening and increased strength. The subsequent straining results in a further accumulation of strain inside the "core", reaching a strength comparable to the "cell". Thereafter, the whole structure, including the "core" and the "cell", deforms homogeneously until fracture. Hence, the much better ductility of the HPT samples is due to the accommodation of plastic deformation by the softer "core", which promotes the uniform distribution of strain during plastic deformation. The similar deformation mechanism was also reported in the so-called "harmonic structure" which is effective in achieving a combination of reasonable ductility and high strength [5-8]. It is also reported that higher "core" size could lead to higher ductility [6, 7].

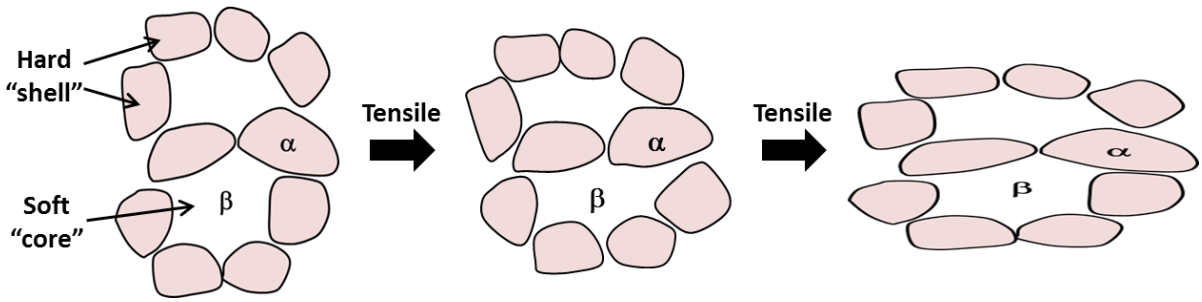

Fig. 4.23 A schematic diagram depicts the deformation mechanism of the HPT samples after step aging.

Different with the HPT samples, the plastic deformation is uneven in the ST samples which have heterogeneous acicular primary α phase. Fig. 4.24 shows the BSE-SEM morphology near the transgranular fracture surface in the cross-sectional direction of the ST sample second aged at 650 ºC for 14.4 ks. Some microvoids can be seen in the regions where there is only primary α phase in the β matrix. During the transgranular fracture, the soft precipitate-free β matrix close to the primary α phase is preferentially deformed. The local strain at the interface between the acicular primary α phase and β matrix results in the formation of the microvoids. The uneven deformation of the micro-zone occurs in the early stage of the tensile deformation, accelerating the formation and propagation of the microvoids. Therefore the ST samples

show a premature failure with a poor ductility.

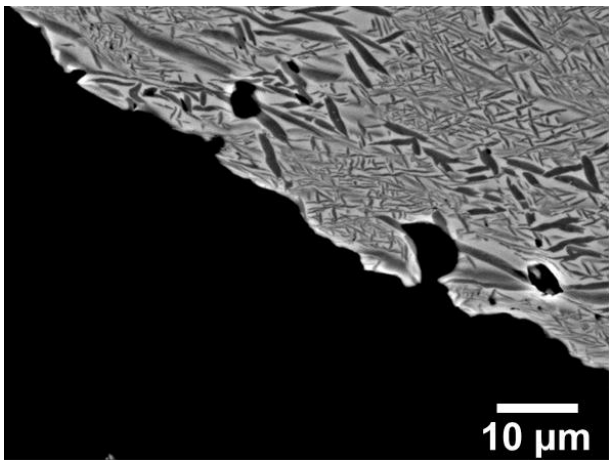

Fig. 4.24 BSE-SEM morphology near the transgranular fracture surface in the cross-sectional direction of the ST sample second aged at 650 °C for 14.4 ks.

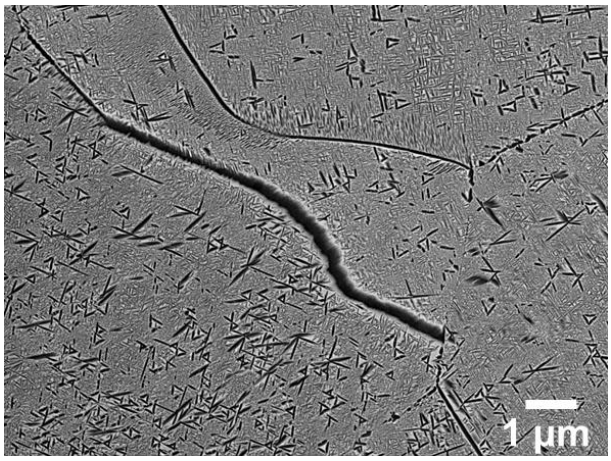

Fig. 4.25 BSE-SEM morphology showing the intergranular crack close to the fracture surface in the cross-sectional direction of the ST sample second aged at 650 °C for 14.4 ks.

Compared the ST samples and HPT samples, another microstructural parameter affecting the tensile properties is the β grain size. The governing influence of the grain size of β matrix on the ductility is related to the formation of grain boundary α phase films [9]. It has been reported that the grain boundary α phase films have pronounced effect on the mechanical properties of high strength β-Ti alloys [10-12]. In the present research, thick and continuous grain boundary α phase films form in the ST samples because of the large β grain size. And they are considered as one of the microstructural parameters that result in the low ductility in the ST samples, especially at lower second aging temperatures. Due to the strong precipitation/dispersion hardening of the matrix (interior of the β grains), preferential plastic deformation occurs along the grain boundary α phase films during the tensile testing. The crack along the grain boundary α phase film can be observed in Fig. 4.25, which shows the SEM morphology close to the fracture surface in the cross sectional direction of the ST sample second aged at 650 °C for 14.4 ks. This phenomenon can be treated in a very

simplified way as a dislocation pile-up against the grain boundaries. Because of the long slip length (≤ β grain size), high stress concentrations and high local strain develop at grain boundary α phase films, enabling easy crack nucleation [13-15]. This can lead to a fracture at low macroscopic strains, although the local strains in the grain boundary α phase films are high. Meanwhile, the much smaller β grain in the HPT samples reduces the thickness and continuity of grain boundary α phase and the grain boundary α phase is not responsible for the main crack nucleation process.

At last, the tensile properties of Ti-5553 alloy obtained in the present study will be compared with referenced results, as shown in Fig. 4.26. The green squares indicate the present results from HPT processed samples after 2-step aging. It is clearly that the present results show a better combination of ultimate tensile strength and ductility. This implies that severe plastic deformation by HPT followed by 2-step aging is an effective method to obtain good combination of tensile strength and ductility.

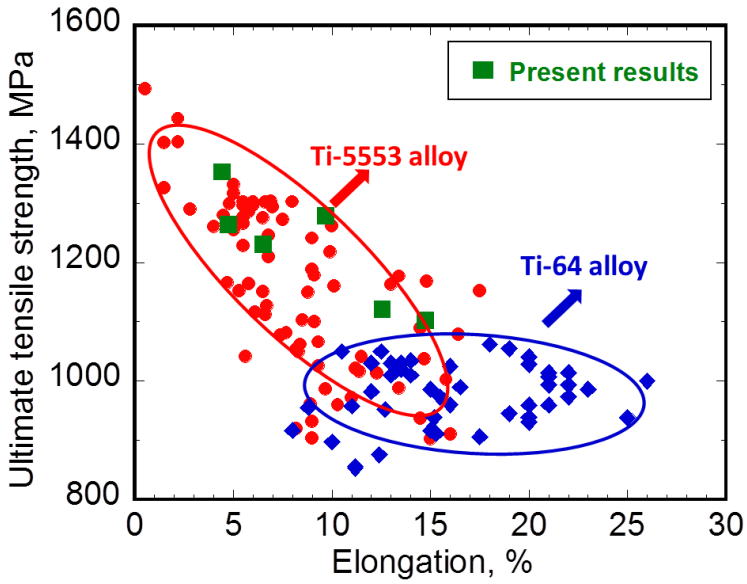

Fig. 4.26 Comparison of the tensile properties of Ti-5553 alloy obtained in the present study with referenced results [3, 16-19].

4.5 Summary

In the Ti-5553 alloy a variety of microstructures has been studied. They were established by a combination of solution treatment, high-pressure torsion (HPT) process and subsequent 2-step aging. The microstructures were characterized by different types of α phase (primary α phase, secondary α phase and grain boundary α phase), with different volume fractions, particle sizes, distributions and morphologies. The effects of α phase precipitates on the tensile properties were investigated. The results can be summarized as follows:

(1) Upon 2-step aging, the microstructure consisted of primary α phase and secondary α phase was obtained. The primary α phase in the ST samples was heterogeneous and had acicular morphology, while the primary α phase in the HPT samples was homogeneous and had equiaxed morphology.

(2) Coarse and continuous grain boundary α phase films were formed in the ST samples. The fine β grains

in the HPT samples which were less than 2 μm reduced the thickness and continuity of the grain boundary α phase.

(3) The particle size of α phase and the volume fraction of primary α phase increased by increasing the aging temperature or aging time, accompanied with a decrease in the volume fraction of secondary α phase. The HPT samples had a higher volume fraction of primary α phase, a lower volume fraction of secondary α phase and smaller α particle size than the ST samples.

(4) Similar microhardness and ultimate tensile strength were obtained in the ST samples and HPT samples, but the HPT samples had much better ductility than the ST samples. There was a decrease in the microhardness and ultimate tensile strength by increasing the aging temperature or aging time, accompanied with an increase in the ductility.

(5) The precipitation hardening by α phase could be explained by Hall-Petch strengthening mechanism. The increase in the volume fraction and particle size of primary α phase which was at the expense of secondary α phase led to an increase in the interphase space, decreasing the strength and increasing the ductility.

(6) In HPT samples, hard equiaxed primary α phase surrounded the ductile β phase, forming network-like structure. Preferential deformation occurred inside the soft β phase during tensile deformation, but subsequent straining led to the deformation of the whole structure. The homogeneous network-like structure promoted the uniform distribution of strain during plastic deformation, contributing to the ductility.

4.6 References

[1] J.C. Williams, F.H. Froes, J.C. Chesnutt, C.G. Rhodes, R.G. Berryman, Toughness and fracture behavior of titanium, ASTM STP , 651 (1978) 64-114.

[2] R.R. Boyer, Design properties of a high-strength titanium alloy, Ti-10V-2Fe-3Al, JOM, 32 (1980) 61-65.

[3] J.C Fanning, Properties of TIMETAL 555 (Ti-5Al-Mo-5V-3Cr-0.6Fe), JMEPEG, 14 (2005) 788-791.

[4] S.L. Nyakana, J.C. Fanning, R.R. Boyer, Quick reference guide for β titanium alloys in the 00s, JMEPEG, 14 (2005) 799-811.

[5] S.K. Vajpai, K. Amayama, M. Ota, T. Watanabe, R. Maeda, T. Sekiguchi, G. Dirras, A. Tingaud, High performance Ti-6Al-4V alloy by creation of harmonic structure design, IOP. Conf. Series: Mater. Sci. Eng. 63 (2014) 012030.

[6] H. Fujiwara, Ryota Akada, A. Noro, Y. Yoshita, K. Ameyama, Enhanced Mechanical properties of nano/meso Hybrid structure materials produced by hot roll sintering process, Mater. Trans. 49 (2008) 90-96.

[7] T. Sekiguchi, K. Ono, H. Fujiwara, K. Ameyama, New microstructure design for commercially pure titanium with outstanding mechanical properties by mechanical milling and hot roll sintering, Mater. Trans. 51 (2010) 39-45.

[8] D. Orlov, H. Fujiwara, K. Ameyama, Obtaining copper with harmonic structure for the optimal balance of structure-performance relationship, Mater. Trans. 54 (2013) 1549-1553.

[9] O.M. Ivasishin, R.V. Teliovich, A comparative study of the mechanical properties of high-strength β-titanium alloys, Mater. Sci. Eng. A 263 (1999) 142-154.

[10] A. Ghosh, S. Sivaprasad, A. Bhattacharjee, S.K. Kar, Microstructure–fracture toughness correlation in an aircraft structural component alloy Ti–5Al–5V–5Mo–3Cr, Mater. Sci. Eng. A 568 (2013) 61-67.

[11] G. Lutjering, J.Albrecht, C. Sauer, T. Krull, The influence of soft, precipitate-free zones at grain boundaries in Ti and Al alloys on their fatigue and fracture behavior, Mater. Sci. Eng. A 468 (2007) 201-209.

[12] J.W. Foltz, B. Welk, P.C. Collins, H.L. Fraser, J.C. Williams, Formation of grain boundary α in β Ti alloys: Its role in deformation and fracture behavior of these alloys, Metall. Mater. Trans. A 42A (2011) 645-650.

[13] G.T. Terlinde, T.W. Duerig, J.C. Williams, Microstructure, tensile deformation and fracture in aged Ti-10V-2Fe-3Al, Metall. Trans. A 14A (1983) 2101-2105.

[14] G. Terlinde, G. Luetjering, Influence of grain size and age-hardening on dislocation pile-ups and tensile fracture for a Ti-Al alloy, Metall. Trans. A 13A (1982) 1283-1292.

[15] G. Terlinde, H.J. Rathjen, K.H. Schwalbe, Microstructure and fracture toughness of the aged β-Ti alloy Ti-10V-2Fe-3Al, Metall. Trans. A 19A (1988) 1037-1049.

[16] N. Clement, A. Lenain, P.J. Jacques, Mechanical property optimization via microstructural control of new metastable beta titanium alloys, JOM 59 (2007) 50-53.

[17] B.A. Welk, Microstructural and property relationships in β-titanium alloy Ti-5553, Master's thesis, The Ohio State University, 201 West 19th Avenue, Columbus, OH 43210, 2010.

[18] R.P. Giosa, Microstructure evolution and mechanical properties in Ti-5Al-5Mo-5V-3Cr after solution treatment and aging in the alpha-beta range, Mc Master University.

[19] R. Boyer, G. Welsch, E.W. Collings, Materials Properties Handbook: Titanium Alloy. Materials Park, OH: ASM International (1994) 525-527.

Chapter 5 Conclusions

In the present work, severe plastic deformation by high-pressure torsion (HPT) was performed on metastable β-type Ti-5Al-5Mo-5V-3Cr (mass%, Ti-5553) alloy. The influences of HPT processing on the microstructure and mechanical properties of Ti-5553 alloy were studied. The precipitation behavior of α phase in the HPT processed samples were investigated and compared with that in the solution treated samples (ST samples without HPT processing). The influence of the α phase on the mechanical properties was also discussed.

1. HPT introduces a high density of shear bands in the samples which increases with the rotation numbers. As the results, a significant grain refinement and a high density of dislocations were introduced in Ti-5553 alloy by HPT processing. The dislocation seems to distribute uniformly in the b grains without forming subgrains. The low-angle annular dark field observations suggested the formation of dislocation cells. The dislocation strengthening seems to a cause of high hardness and ultimate tensile strength, accompanied by a brittle failure.

2. Upon aging, ultrafine equiaxed α phase precipitated in HPT samples, while coarse acicular α phase formed in the ST samples. The particle size of the equiaxed α phase was much smaller than the length of the acicular α phase, but similar to or a little larger than the thickness of the acicular α phase.

3. HPT-induced high density of dislocations could provide numerous nucleation sites and enhanced diffusivity, accelerating the nucleation of a large number of α phases. The dense precipitation of α phase resulted in overlapping diffusion fields which could retard the growth of α phase during long time aging, leading to ultrafine particle size with equiaxed morphology.

4. The same with the acicular α phase precipitates, the equiaxed α phase also maintained Burgers orientation relationship, $\{0001\}_\alpha$ // $\{011\}_\beta$; $<11\bar{2}0>_\alpha$ // $<1\bar{1}1>_\beta$, with the β phase.

5. The precipitation of α phase strongly influenced the mechanical properties. The strengthening by the precipitation of α phase could be explained by Hall-Petch strengthening mechanism. The higher volume fraction or the finer particle size of α phase caused a smaller space between α particles, consequently

leading to the higher strength and lower ductility.

6. A good combination of strength and ductility was obtained in the HPT samples after 2-step aging. In the HPT samples, hard equiaxed primary α phase surrounded the ductile β phase, forming network-like structure. Preferential deformation occurred in the soft β phase during the initial stage of tensile deformation, and subsequent straining led to the deformation of the whole structure, including primary α phase. The network-like structure composed of soft β phase and surrounding hard α phase improves the strength-ductility balance.

Unsolved issues and future work

Unsolved issues

Present thesis investigated and discussed the influences of severe plastic deformation on the precipitation behavior of α phase in Ti-5Al-5Mo-5V-3Cr (Ti-5553, mass%) alloy and the influences of α phase on the mechanical properties. While several aspects of the phenomenon has been clarified and explained well in the thesis, there are still a few unsolved issues which deserve to be mentioned.

- Upon aging, the recovery and recrystallization of β phase and the precipitation of α phase seem to occur in parallel in HPT processed Ti-5553 alloy. The recovered/recrystallized β phases form microzone where many β grains have very similar crystallographic orientation. The details of this process needs to be clarified.
- By increasing the aging temperature or aging time, there is an increase in the nanohardness of equiaxed α phase while no change in the nanohardness of acicular α phase and the equiaxed α phase becomes much harder than the acicular α phase. Unfortunately, we cannot give detailed explains on this phenomenon.
- The tensile deformation process of HPT processed Ti-5553 alloy after 2-step aging are investigated by EBSD analysis. However, the deformation modes for the β phase and the primary equiaxed α phase are not mentioned, and the detailed deformation mechanism at the α/β interfaces is not given.

Future work

In the future, we will try to find the answers for the unsolved issues. In addition, some other work will be focused on.

- The homogeneous network-like structure formed in the HPT processed samples after 2-step aging contributes to the tensile properties. How about the influence of this kind of structure to some other mechanical properties, such as high-cycle fatigue property? And can we obtain this kind of microstructure by some other cold deformation method, such as caliber rolling?
- In the present thesis, HPT processing is performed on β-type Ti-5553 alloy. How about the influence of HPT processing on α+β type Ti-5553 alloy and corresponding precipitation behavior of α phase upon aging?

Acknowledgements

This was the last part that I completed when I was writing my thesis, because too many times too many people's names crowded into my mind that I wished to give my sincere thanks to. During my PHD course under the joint program between National Institute for Materials Science (NIMS) and University of Tsukuba, I have been so lucky to study and work with so many people who helped and supported me towards my work.

First and foremost, I would like express my deepest sense of gratitude to my supervisor, Dr. Koichi TSUCHIYA, for his unwavering support and encouragement throughout my work. His suggestions towards research helped me grow as an experimentalist. At a personal level he has always treated me with great kindness and I respect him for everything I have learnt from him.

Secondly, I would like to thank Dr. Satoshi EMURA for providing many supports and suggestions throughout my study and being my committee. I also would like to thank Dr. Hee Young KIM from Graduate School of Pure and Applied Sciences in University of Tsukuba and Dr. Yoshio SAKKA from Materials Processing Unit in NIMS for being my committee.

I would like to thank Mr. Mitsuaki NISHIO from Materials Analysis Station in NIMS for his help in the EPMA observations and Ms. Hong GAO from International Center for Young Scientist in NIMS for her guidance on EBSD analysis.

I would like to express my thanks to all the current and previous members in Microstructure Design Group: Dr. Xiaohua MIN, Dr. Seiichiro II, Dr. Ryoji SAHARA, Dr. Gutierrez Urrutia IVAN, Dr. Alok SINGH and Dr. Julian ROSALIE for their support during my experiments and encouragement whenever I was in need. My gratitude is also given to my friends: Dr. Fanqiang MENG, Dr. Dayangku Noorfazidah AWANG, Haotian NI, Xuejiao CHEN, Xin JI and Takashi MIYAWAKI for making my life in Tsukuba easier.

I also would like to thank Ms. Tomomi UTAGAWA who helped me so much on my life in Tsukuba and Ms. Yoshimi TOYONO who helped me so much in my experimental operations.

Last but not least, I would like to thank my parents and sisters in china for their love and tremendous supports in my life. My beautiful and kind wife Ms. Ruiqi PAN always encourages and helps me when I faced difficulties. My cute son is the strongest force for me to study and work. I would like to give this thesis as a present to my son for his first birthday